INVESTIGATION OF A DOUBLY SALIENT SPECIAL MACHINE WITH PERMANENT MAGNETS IN STATOR FOR ELECTRICAL VEHICLE TRACTION APPLICATIONS

by

Chandra Sekhar Goli

A dissertation submitted to the faculty of
The University of North Carolina at Charlotte
in partial fulfillment of the requirements
for the degree of Doctor of Philosophy in
Electrical Engineering

Charlotte

2024

Approved by:

_____
Dr. Madhav Manjrekar

_____
Dr. Sukumar Kamalasadan

_____
Dr. Valentina Cecchi

_____
Dr. Maciej Noras

_____
Dr. Tiefu Zhao

_____
Dr. Somasundaram Essakiappan

ABSTRACT

CHANDRA SEKHAR GOLI. Investigation of a Doubly Salient Special Machine with Permanent Magnets in Stator for Electrical Vehicle Traction Applications

(Under the direction of DR. MADHAV MANJREKAR)

An in-depth analysis of a distinctive machine topology characterized by a doubly salient structure and integrated permanent magnets within the stator is presented in this dissertation. The machine exhibits exceptional power density performance of upto 50kW/L, capable of operating at a rated torque of 95Nm at a rated speed of 12,500rpm, and maximum speed of 37,500rpm with a specific focus on its relevance to electric vehicle traction applications. The machine comprises 12 stator segments and coils configure for three-phases, interspersed with 12 PMs in the stator, along with a reluctance-type rotor featuring 10 protrusions equivalent to 20 electric poles.

An analytical model for this novel machine configuration is developed using lumped parameter magnetic equivalent circuits (LPMEC), encompassing stator segments, permanent magnets (PM), toroidal windings, air gap, and a reluctance-type rotor. In contrast to prior analytical methods, the proposed methodology thoroughly investigates spatial harmonics, elucidating the non-saliency behavior of the machine. The LPMEC model is employed to compute critical parameters such as flux linkages, open circuit back EMF, and inductances with respect to the rotor position. These outcomes are validated through finite element analysis. Intriguingly, despite its inherently doubly salient structure, the proposed machine exhibits characteristics similar to a non-salient machine such as surface permanent magnet machine. This behavior is substantiated by the scrutiny of spatial harmonics.

For comprehensive evaluation, a high-fidelity model-based motor drive system is developed. A field-oriented control approach is adopted to regulate torque and speed across a broad spectrum encompassing constant torque and field weakening regimes. Further, a complex vector current (CVC) regulation strategy is introduced to account for the substantial variations in inductances with rotor position. Unlike classical current regulation strategies in synchronous reference frames, the CVC strategy is more robust despite uncertainties related to the estimation of d-q inductances of plant model, thus enhancing the stability of the control system.

In-depth comparative analysis between the classical synchronous reference frame proportional integral current control and CVC regulation strategies is conducted. A detailed stability analysis reveals the robustness of the CVC regulation strategy without the need for decoupling feed-forward voltages compared to the classical proportional integral current regulation strategy with decoupling voltages. The efficacy of these regulation strategies is validated through extensive simulations in the continuous domain and substantiated through controller hardware in the loop (CHIL) experiments.

Experimental tests have been conducted to validate the analytical outcomes and proposed control methodologies employing an open frame laboratory prototype (OFLP) of the proposed machine and SiC based traction inverter.

ACKNOWLEDGMENTS

I gratefully acknowledge the invaluable guidance I received from my advisor, Dr. Madhav Manjrekar, throughout this academic journey. I extend my heartfelt thanks to Dr. Sukumar Kamalasadan, Dr. Valentina Cecchi, Dr. Maciej Noras, Dr. Tiefu Zhao, Dr. Somasundaram Essakiappan, and Mr. James Gafford for their insightful reviews and enriching discussions. Special appreciation goes to Prof. Dan M Ionel and late Mr. Charles Joe Flynn for their invaluable guidance, which greatly enhanced my understanding of electric machines.

My gratitude extends to my fiancé, parents, and siblings for their unwavering support in achieving this significant milestone.

I am also appreciative of the assistance from my friends at the University of North Carolina at Charlotte. I extend special thanks to Andrew LeClair, Nakul Shah, Dr. Prasanth Kumar Sahu, Mariyam Saleh, Dr. Abilash Thakallapelli, Dr. Rubin Bisht, and Dr. Aniket Joshi for their invaluable feedback.

Furthermore, I would like to acknowledge the generous support provided by the U.S. Department of Energy (DoE), QM Power, and Energy Production and Infrastructure Center (EPIC). Your contributions have been instrumental in the success of this endeavor.

DEDICATION

I dedicate this dissertation to my loving fiancé and my family. Your unwavering support, encouragement, and love have been my pillars throughout this academic journey. This accomplishment is as much yours as it is mine. Thank you for being my source of strength.

TABLE OF CONTENTS

LIST OF FIGURES

LIST OF TABLES

CHAPTER 1: INTRODUCTION

1.1. Introduction

This chapter presents a brief introduction and organization of the dissertation. The motivation behind this dissertation is presented in section 1.2. The organization of the dissertation has been discussed in section 1.3.

1.2. Dissertation Motivation

With increasing penetration of electric vehicles, electric motor technologies have also seen rapid evolution. A handout [1] from the U.S. Department of Energy (DoE) has listed key targets for traction motor and Power Electronics Inverter Module (PIM) of the electric drive system for the years 2020 and 2025 have been shown in TABLE 1.1.

TABLE 1.1: DOE TARGETS FOR TRACTION MOTOR AND PIM

DoE Targets	Cost ($/kW)		Power Density (kW/L)	
	2020	2025	2020	2025
Traction Motor	4.7	3.3	5.7	50
PIM	3.3	2.70	13.4	100

Over the decades, there haven't been significant improvements in energy storage technologies in electric vehicle traction applications. Introducing a high power dense traction motors in order to increase the mileage which reflects as a better utilization of energy delivered from the battery may have significant impact on adaptability of electric vehicles for transportation applications.

In this regard, a special doubly salient machine with permanent magnets in stator, capable of very high power density up to 50kW/L has been investigated in this dissertation. The proposed doubly salient permanent magnet machine (DSPM) is based on the concept

of parallel path magnetic technology introduced by Charles Joe Flynn [64]. A three-phase DSPM machine with 12 slots, 12 PM, and reluctance type rotor with 10 pole protrusions equivalent to 20 electric poles has been analyzed in this dissertation.

Despite the doubly salient structure, the proposed DSPM has a non-salient behavior similar to surface permanent magnet machine (SPM). A detailed analysis reported in this dissertation addresses the non-salient behavior of machines with doubly salient structures such as proposed DSPM and flux switching permanent magnet machine (FSPM). A model-based motor drive system with maximum torque per Ampere (MTPA) and field weakening control algorithms is presented in this dissertation considering non-linear characteristics of flux linkages. A complex vector current regulation strategy with improved transient response and less peak overshoot has been developed to account for substantial variation in the estimated inductances of the proposed DSPM.

Thus, analytical modeling, model-based motor drive system development, and complex vector current regulation strategy have been thoroughly investigated for the proposed machine. Controller hardware in loop (C-HIL) has been employed to verify the control algorithms. An open frame laboratory prototype (OFLP) of the machine has been built to perform experimental tests to validate the analytical results and control algorithms.

1.3.Organization of Dissertation

A brief overview of the organization of the thesis has been discussed in this section.

Chapter 1: Introduction

This chapter has been focused on detailing the importance of high-power dense traction motors and the motivation behind this dissertation is discussed in Section 1.2. The organization of the dissertation has been presented in Section 1.3.

Chapter 2: Literature Review

A literature review and landscaping of traction motors and traction inverters has been presented in this chapter. Targets for key design matrices of traction motor and power inverter module are introduced in Section 2.1. Landscaping and review of popular topologies of traction motors in commercially available electrical vehicles are discussed in Section 2.2. Design trend in rotor and stator of the traction motors is presented in Section 2.3 and Section 2.4. Landscaping and review of traction inverters have been reported in Section 2.5. Topology and control methodology are discussed in Section 2.6. Selection of components to improve power density of traction inverters is discussed in Section 2.7.

Chapter 3: Doubly Salient Machines

Several topologies of doubly salient machines are introduced in section 3.1. Magnet free doubly salient machines such as flux switching machine and switched reluctance machines are discussed in Section 3.2 and Section 3.3. Doubly salient machine with permanent magnets such as Lipo's classical DSPM with PMs in back iron is presented in Section 3.4. Another classical DSPM employing PPMT invented by Charles J Flynn is discussed in Section 3.5. Focus of this dissertation, analysis of a three-phase doubly salient permanent magnet machine employing PPMT and explanation of rotating magnetic field employing winding function theory are detailed in Section 3.6.

Chapter 4: Analysis of a Mechanically Doubly Salient Electric Machine Using FE and Lumped Parameter Magnetic Equivalent Circuit Models

Analysis of the proposed special DSPM employing lumped parameter magnetic equivalent circuits (LPMEC) and finite element method is detailed in this chapter. The

process of employing LPMECs to the DSPM is introduced in Section 4.1. Analysis of magnetic equivalent circuits is presented in Section 4.2. Non-saliency behavior of the proposed DSPM is investigated in Section 4.3.

Chapter 5: Model-Based Motor Drive Development

Model-based motor drive development is presented in this chapter. A workflow detailing several steps in implementing model-based motor drive development is introduced in Section 5.1. Modeling of the proposed high power dense DSPM machine is presented in Section 5.2. Control methodology employing high-fidelity plant model, maximum torque per Ampere (MTPA) and flux weakening control strategies are discussed in Section 5.3. Stability analysis of the implemented control strategies by means Bode plot is reported in Section 5.4.

Chapter 6: Complex Vector Current Regulation Strategy

Complex vector current (CVC) regulation strategy for the special DSPM motor drive system is discussed in this chapter. Significance of CVC regulation strategy, effect of bandwidth, and empirical tuning of proportional and integral controllers are introduced in Section 6.1. Analysis of conventional synchronous reference frame proportional integral control strategy (SRF-PI) and CVC regulation strategy are discussed in Section 6.2 and Section 6.3. Stability analysis of SRF-PI and CVC regulation strategies is reported in Section 6.4.

Chapter 7: Simulation & C-HIL Results

Continuous domain simulation results and discrete domain controller hardware in loop (C-HIL) are presented in Section 7.1. Simulation results of model-based motor drive

system are reported in Section 7.2. Comparative analysis of SRF-PI and CVC regulation strategies and their respective simulation results are discussed in Section 7.3. C-HIL results of comparative analysis of SRF-PI and CVC regulation strategies are reported in Section 7.4.

Chapter 8: Experimental Validation of Control Algorithms

This chapter focuses on presenting the details of the experimental setup and validation of torque control algorithms to assess the performance of the open frame laboratory prototype (OFLP) of the proposed high-power density motor. It covers the specifics of the motor dynamometer experimental setup, the design of experiments aimed at identifying the plant model of the OFLP, and the implementation of torque control algorithms.

Chapter 9: Conclusions

This chapter consists of a conclusive discussion on the outcomes of analysis of the proposed special motor drive system for electric vehicle traction applications. State of the art of traction motors and inverters, investigation of non-saliency behavior of the proposed special DSPM, verification of model-based control algorithms, and validation of the respective control algorithms employing continuous domain simulations, C-HIL, and experimental tests on OFLP of the motor are detailed in this section.

All the references used in this dissertation have been listed in bibliography.

Chapter 10: Future Works

Future works relevant to the presented dissertation topic are listed in this chapter followed by bibliography and publications.

CHAPTER 2: LITERATURE REVIEW OF TRACTION MOTORS AND INVERTERS

2.1. Introduction

With increasing penetration of electric vehicles, electric motor and inverter technologies have also seen rapid evolution. Review and landscape of several topologies of traction motors and traction inverters employed in electrical vehicle traction applications are reported in this chapter. An emphasis has been made to showcase trends in volumetric power density and gravimetric power density of traction motors and traction inverters since they directly affect end product weight, packaging, and efficiency. A handout [1] from the U.S. Department of Energy (DoE) has listed key targets for traction motor and Power Electronics Inverter Module (PIM) of the electric drive system for the years 2020 and 2025 have been shown in TABLE 2.1.

TABLE 2.1: DOE TARGETS FOR TRACTION MOTOR AND PIM

DoE Targets	Cost ($/kW)		Power Density (kW/L)	
	2020	2025	2020	2025
Traction Motor	4.7	3.3	5.7	50
PIM	3.3	2.70	13.4	100

2.2. Landscaping and Review of Traction Motors

A study and classification of motor topologies based on permanent magnet use, the location of the permanent magnets inside the motor, magnetic and reluctance components of torque, and design trends in rotor and stator have been discussed. Several key Original Equipment Manufacturers (OEM) products have been used in this analysis and thus, this

chapter provides a useful reference for understanding the product evolution and forecasting future trends.

Design matrices of traction motors employed in electric vehicles have been reviewed in several papers. Comparison of design matrices of traction motors employed in several types of electric vehicles has been discussed in previous literature [2]. The differences between AC motors, DC motors and their suitability towards electric vehicle traction applications and their adoption in battery-operated electric vehicles and hybrid electric vehicles have been evaluated in the existing literature. Comprehensive data of drive cycle capabilities of different traction motors have been reviewed in [3], [4], and [23] consists of the comparison of synchronous motors, internal permanent magnet synchronous motors, and induction motors. The efficiency and cost factors of DC motors, induction motors, switched reluctance motors, permanent magnet-based motors, and flux switching motors for traction applications have been reported in [5]. However, the existing literature review of different topologies of traction motors is not extensive and design matrices have not been profiled. A study of torque capabilities of several types of permanent magnet synchronous motors employed in traction applications has been reviewed in this chapter. Volumetric power density and gravimetric power density of traction motors have been profiled. An extensive list of specifications of traction motors used in Battery Operated Electric Vehicles (BEV), Hybrid Electric Vehicles (HEV), Plugin Hybrid Electric Vehicles (PHEV), and Fuel Cell Electric Vehicles (FCEV) have been listed in TABLE 2.2. Permanent Magnet Assisted Synchronous Reluctance Motor (PM-SyRM), Induction Motor (IM), and Internal Permanent Magnet Synchronous Motor (IPMSM) are popular among electric vehicle traction applications.

TABLE 2.2: SPECIFICATIONS OF COMMERCIALLY AVAILABLE TRACTION MOTORS

	EV Type	Motor Type	Power (kW)	Torque (N.m)	Speed (peak RPM)	VPD (kW/L)	GPD (kW/kg)
Jaguar I-Pace 2019 [6]	BEV	PM-SyRM	294	696	13000	6.37	7.73
Nissan Leaf 2019 [6][17]	BEV	PM-SyRM	110	320	10400	2.619	-
Tesla M3 2018 [6]	BEV	PM-SyRM IM	Rear:285 Front: 145	750 (total)	18100	Rear: 10.27 Front: 8.977	Rear:9.21 Front:6.22
Chevy Bolt 2017 [7]	BEV	PM-SyRM	150	360	8810	3.49	4.44
Toyota Prius 2017 [8]	PHEV	PM-SyRM	53	-	17000	5.7	5.69*
Audi e-Tron SUV 2016 [8]	PHEV	IM, IM	Front: 135 Rear: 165	Front: 309 Rear: 355	6000	-	-
BMW i3 2016 [8]	BEV	PM-SyRM	125	250	11400	9.1	3.58
Chevy Volt 2016 [8]	PHEV	PM-SyRM	112	400	-	-	3.07
Cadillac CT6 2016 [9]	PHEV	IPMSM	2x75	-	-	-	-
Honda Accord 2014 [4]	HEV	IPMSM	125	110	8000	8.5	2.9
Chevy Spark 2014 [7]	BEV	PM-SyRM	-	540 (peak)	4500	-	-
Nissan Leaf 2012 [9]	BEV	PM-SyRM	80	280	10390	-	1.42
Sonata HSG 2012 [8]	HEV	IPMSM	30	45	15000	7.42	1.9
Toyota Prius 2010 [8]	HEV	IPMSM	60 (peak)	207 (peak)	13500	4.8	1.6
Lexus 2008 [8]	HEV	IPMSM	110 (peak)	300 (peak)	10230	6.6	2.5
Toyota Camry 2007 [8]	HEV	IPMSM	70 (peak)	270 (peak)	14000	5.9	1.7
Honda Accord 2006 [8]	HEV	IPMSM	12.4	136	6000	--	-
Toyota Prius 2004 [8]	HEV	IPMSM	50	400	6000	3.3	1.11
Nissan Hypermini 2003 [8]	FCEV	IPMSM	24	130	6700	-	0.4
GM EV1 1999 [22]	BEV	IM	102	149	7000	-	-

*hybrid system net power density, IM: Induction Motor

Wound field induction motors are known for poor power factor and low power density because of the presence of copper winding on the rotor in addition to the stator of the motor. Classical wound field machines have been designed to operate from pure AC may often need power electronic converters to control speed and torque. The field winding is eliminated by inclusion of permanent magnets in the electric motors come with the advantages of high volumetric power density (VPD) and gravimetric power density (GPD). Improvement in power factor, high torque per Ampere capability and extended constant speed region operation of permanent magnet motors fit them well for electric vehicle traction applications.

Permanent magnet motors cannot be operated from direct AC and the presence of power electronic converters is unavoidable to initiate the operation of the motor. However, speed and torque control of induction motor is much simpler compared to permanent magnet-based motors may still find it as one of the suitable candidates for electric vehicle traction applications. A trend in VPD in kW/L and GPD in kW/kg of the traction motors to timeline has been shown in Figure 2.1 and Figure 2.2. Area of the bubble in the graphs is proportional to the power rating of the traction motor. High VPD and GPD have been observed in battery-operated electric vehicles (BEV). A trend in the adoption of PM-SyRM over IPMSM has been observed among BEV and PHEV automakers in recent years. Various topologies of traction motor have been detailed in further sections that will declassify the advantages of PM-SyRM.

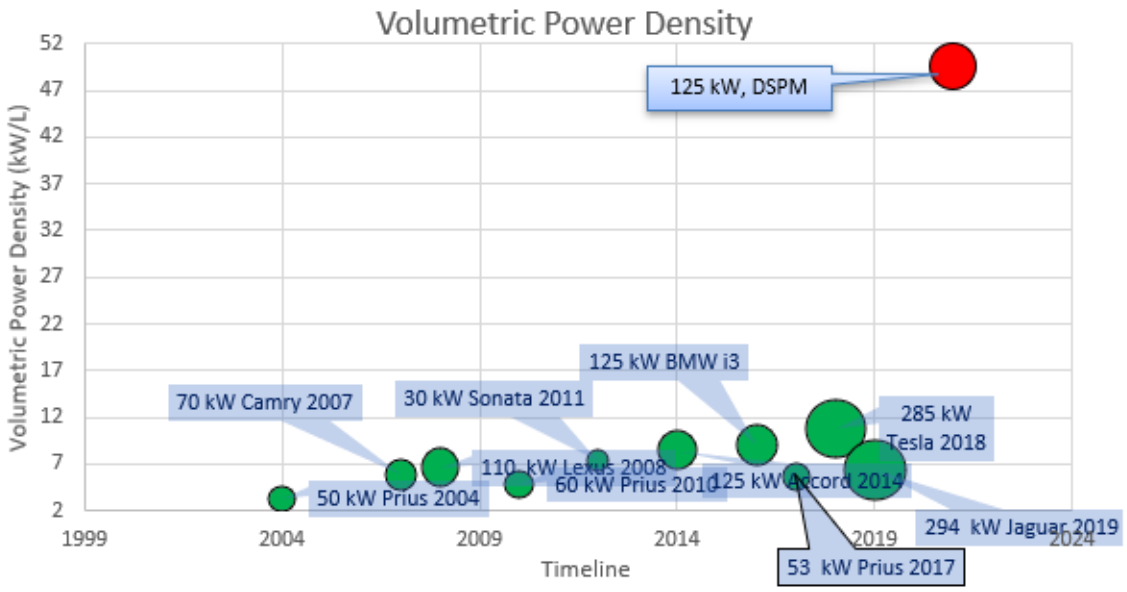

Figure 2.1. Trend in volumetric power density of commercially available traction motors from the year 2004 to 2020.

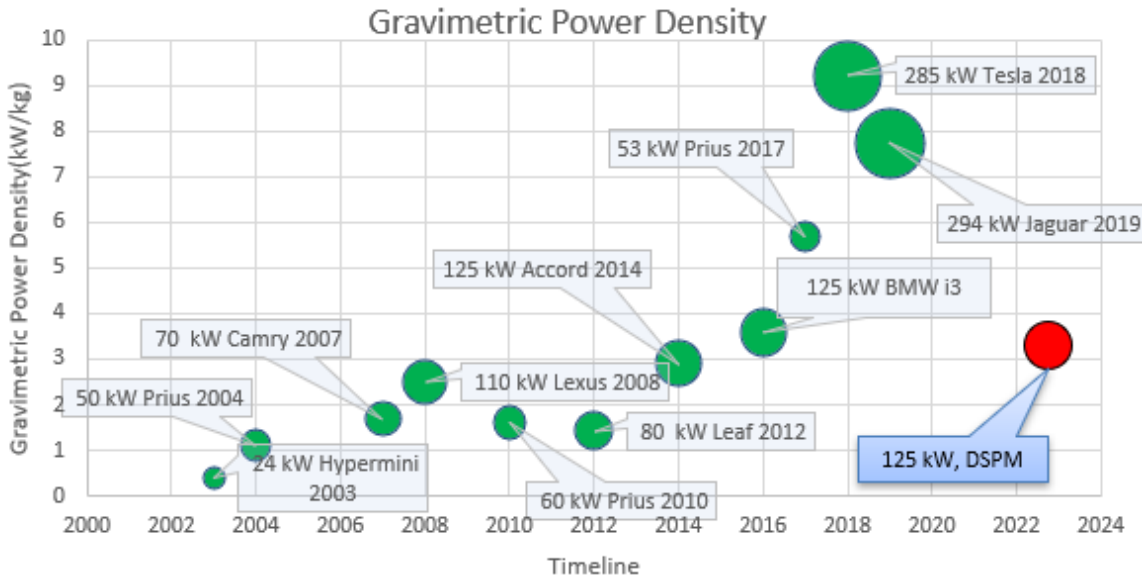

Figure 2.2. Trend in gravimetric power density of commercially available traction motors from the year 2003 to 2020.

2.2.1. Topologies of Motors

Classic topology of synchronous motor and induction motor has armature winding on stator and field winding on the rotor, operates on the principle of rotating magnetic field. Rotating magnetic field set up by alternating current in stator locks the poles set up by field winding on the rotor at synchronous speed in case of synchronous motor. Poles set up by the field winding on the rotor of the induction motor always try to align with rotating magnetic poles set up by stator and rotates at a speed less than synchronous speed. There hasn't been a significant change in the winding topology of induction motors over the years. The operating principle of PM-SyRM and IPMSM is same as classic synchronous motor except filed winding is replaced by permanent magnets. Permanent magnet-based motors which operate on the principle of operation same as synchronous motor are often called as Permanent Magnet Synchronous Motors (PMSM). PMSM is available in different topologies may be classified under synchronous motors. The steady-state torque equation of PM-SyRM and IPMSM can be well understood by going through the geometry of different topologies of synchronous motors as shown in Figure 2.4. Surface Permanent Magnet Motor (SPM), IPM, and PM-SyRM may be sub-classified as PMSMs. Non-salient pole synchronous motor, salient pole synchronous motor, and synchronous motor are classic topologies of synchronous motor.

Classic topologies of synchronous motor have distributed winding on the stator and concentrated winding on the rotor except for synchronous reluctance motor. The stator winding of SPM and IPM may be sinusoidally distributed or concentrated winding based on the application. PM-SyRM has sinusoidally distributed winding on the stator [11]. The

field winding is replaced by permanent magnets in the case of SPM, IPM, and PM-SyRM. The nomenclature used in this chapter has been listed in TABLE 2.3.

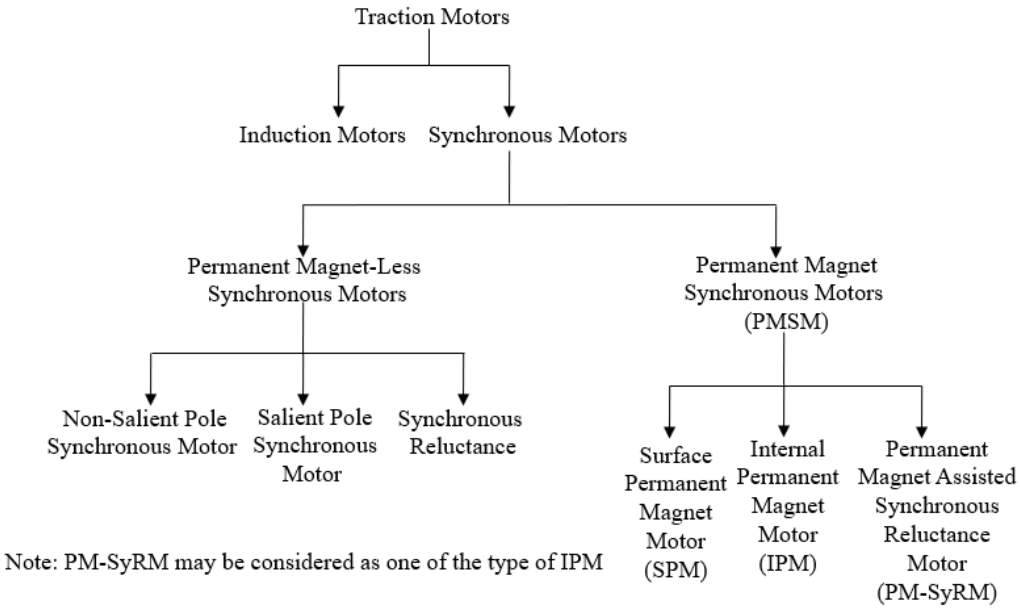

Figure 2.3. Classification of different topologies of traction motors.

TABLE 2.3: NOMENCLATURE

Parameter	*Explanation*
T	*Output torque in N.m*
P	*Number of poles*
V_s	*Source Voltage to the motor*
E	*Induced EMF in Volts*
X_{ds}	*Reactance along direct axis in ohms*
X_{qs}	*Reactance along quadrature axis in ohms*
ω	*Mechanical speed in rad per sec*
δ	*Rotor angle or torque angle*

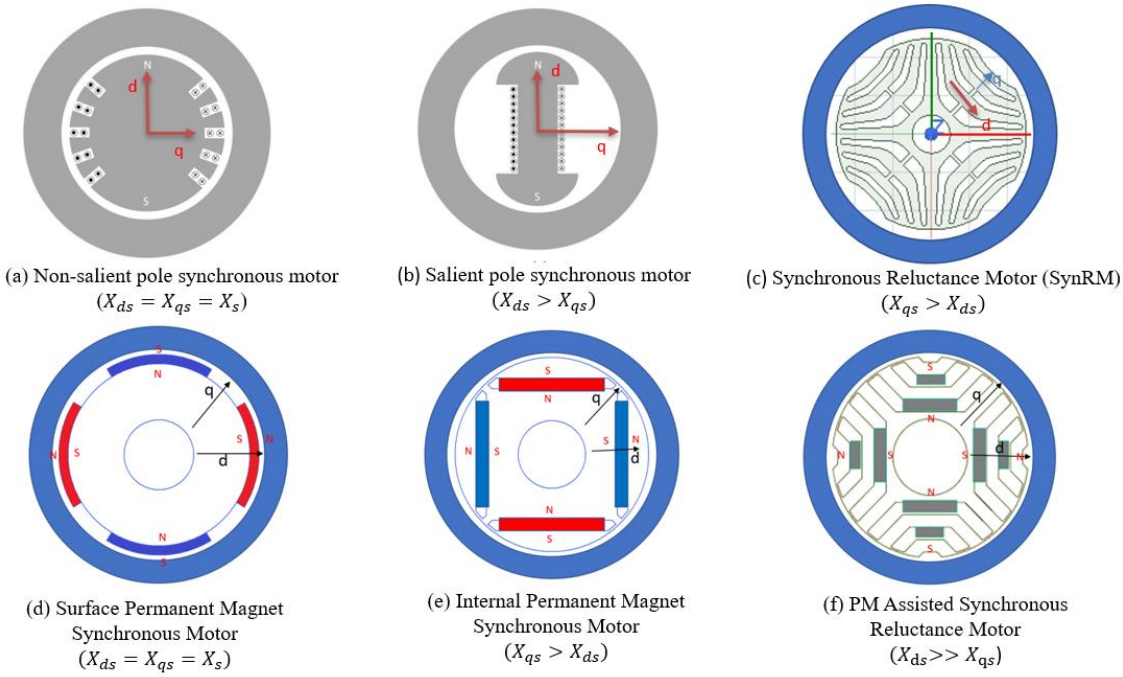

Figure 2.4. Schematics of geometry of different topologies of synchronous motors.

SPM is analogous to a non-salient pole synchronous motor since the cylindrical rotor provides a uniform air gap. Permanent magnets are placed on the surface of the cylindrical rotor for SPM. It must be noted that width of the permanent magnet is considered an air gap. The direct axis is defined along the north pole and the quadrature axis is defined along with the south pole setup by field on the rotor. Reluctance is proportional to the width of airgap, inductance and inductive reactances are inversely proportional to the width of airgap and hence reactance along direct and quadrature axis is equal in the case of non-salient pole synchronous motor and SPM i.e. $X_{ds} = X_{qs}$.

IPM is analogous to a salient pole synchronous motor. Flux set up by the field winding along direct axis has minimum reluctance path since the air gap is minimum and flux along quadrature axis has maximum reluctance path since the air gap is maximum in case of salient pole synchronous motor. Thus, inductance and inductive reactance along the direct axis is more than the quadrature axis i.e. $X_{ds} > X_{qs}$. Similarly, the flux path along

the direct axis of IPM experiences more reluctance since the width of the permanent magnet and length of airgap offer higher reluctance. Flux path along quadrature axis of IPM experiences low reluctance since it has core only along the length of the air gap. Thus, $X_{qs} > X_{ds}$ in the case of IPM.

PM-SyRM is analogous to synchronous reluctance motor with multiple air barriers offering a high reluctance path [28] [29] [30]. The synchronous reluctance motor has no back EMF due to the absence of the field winding of the rotor. Flux path along the direct axis of synchronous reluctance motor experiences low reluctance path compared to flux along quadrature axis i.e. $X_{qs} > X_{ds}$. Similarly, flux along the direct axis has multiple permanent magnets embedded in air barriers in addition to the length of airgap experiences high reluctance path compared to flux along quadrature axis. Thus, $X_{\mathrm{ds}} >> X_{\mathrm{qs}}$ since the width of multiple permanent magnets offers more reluctance compared to IPM or classic synchronous reluctance motor [36]. The difference between reactances along the direct and quadrature axis has a greater influence on the torque produced by PMSM.

The generic equation of torque (1) produced by the synchronous motor has magnetic and reluctance components that may apply to different topologies of the synchronous motor. The difference in magnetic and reluctance components of the torque is based on the shape of the rotor, place of permanent magnets, and air barriers [12] [13].

$$T \cong -\left(\frac{3P}{2\omega}\right)\left[\left(\frac{V_s E}{X_d}\right) sin\delta \; + \left(\frac{1}{2}\right)\frac{V_s^2\left(X_d - X_q\right)}{X_d X_q} sin2\delta\right] \tag{2.1}$$

First-term of generic torque equation (1) is called magnetic torque and the second term is called as reluctance torque. Thus, reluctance torque is negligible in the case of non-salient pole synchronous motor and SPM. Salient pole synchronous motor, IPMSM, and

PM-SyRM have both magnetic and reluctance torque due to the difference between reactances along the d-axis and q-axis. Synchronous reluctance motor has no magnetic torque since no back EMF is induced due to the absence of field winding.

Thus, the torque produced by PM-SyRM outperforms other topologies of PMSM [10]. Torque capability curves of different topologies of synchronous motors have been shown in Figure 2.5. The synchronous motor with internal permanent magnets and air barriers i.e PM-SyRM is capable of delivering more torque by harnessing the reluctance component of the torque with an increase in saliency.

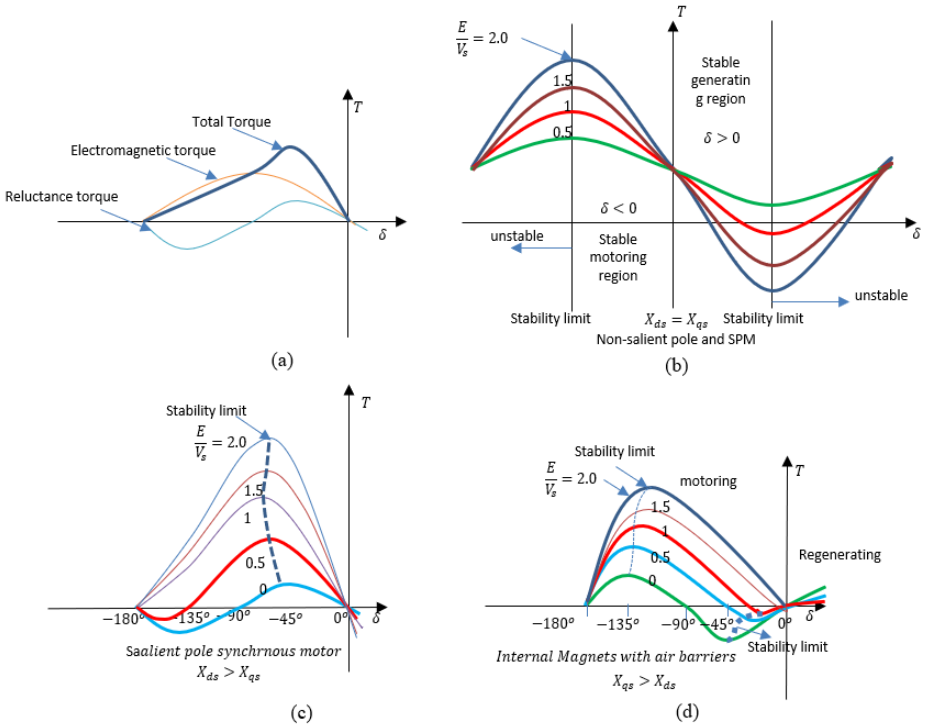

Figure 2.5. (a). Generic characteristic curve of torque versus rotor angle (b). Torque capability curve of non-salient pole synchronous motor or SPM with similar reactances $X_{ds} = X_{qs}$ (c) Torque capability curve of salient pole synchronous motor (d) Torque capability curve of synchronous motor with internal permanent magnets and air barriers.

TABLE 2.4: COMPARISON OF DIFFERENT VARIANTS OF MOTORS

Motor Type	$X_{ds}\ vs\ X_{qs}$	T_{em}	T_{re}	Winding Type
No-salient pole	$X_{ds} = X_{qs}$	High	0	Distributed
Salient pole	$X_{ds} > X_{qs}$	High	Low	Distributed
SPM [31]	$X_{ds} = X_{qs}$	High	Low	Distributed/ Concentrated
IPM	$X_{qs} > X_{ds}$	High	Moderately High	Distributed/ Concentrated
PM-SyRM	$X_{qs} >> X_{ds}$	High	Very High	Distributed
BLDC	-	High	Zero	Concentrated

2.2.2. Design Trend in Rotor

The size and number of permanent magnets embedded inside the rotor of PMSM have a significant influence on torque and the overall cost of the motor [10]. To deliver the same torque, the size and number of permanent magnets used in IPMSM are more compared to the PM-SyRM. An alternative method to decrease the cost of the motor while increasing the torque is by providing air barriers on the rotor. Thus, air barriers on the rotor of PM-SyRM [26] [27] increase the reluctance torque which helps in achieving the cost targets [15]. Teardown reports [16], [17] of Toyota Prius by ORNL have been shown in Figure 2.6, and TABLE 2.5 as an example to show a trend in adapting air barrier design of the rotor to improve the volumetric power density and gravimetric power density while cutting the costs per kilowatt. Further, a reduction in the size and number of PMs on the rotor increased the speed specification of the motor. A similar type of design has been adopted by other manufacturers was reported by Munro Associates [10] has been shown in the Figure 2.7. Chevy Volt has adapted semi-circular type of barriers [25], slots are filled

with ferrite magnets while the remaining have V or U-type air barriers, and slots are partially filled with high flux dense Neodymium (NdFeB) magnets.

Figure 2.6. Design trend in rotor of Toyota Prius over the years from 2002 to 2017 [].

Figure 2.7. Design trend in air barrier type rotors of PM-SyRM [].

TABLE 2.5: DESIGN SPECIFICATIONS OF ROTOR OF TOYOTA PRIUS

	Stack Length (Inches)	Power (kW)	Speed (RPM)
Toyota Prius 2002	3.5	33	6000
Toyota Prius 2004	3.3	50	6000
Toyota Prius 2010 [13]	2	60	13000
Toyota Prius [4] 2017	2.4	53	17000

2.2.3. Design Trend in Stator

No significant change in the winding topology on the stator side of the motor over the years except for the adaption of advanced technology to wound the stator to increase the slot fill factor [37-39]. Distributed winding is more popular among traction motors, but the power density has to be compromised when compared to concentrated winding because of end winding. Concentrated winding results in non-sinusoidal induced voltage would limit the application of SPM motors. However, fractional slot type of concentrated windings would introduce a non-linearity by increasing inductance along direct axis would result in induced voltages near to sinusoidal [18]. An example of design trend in stator windings has been shown in Figure 2.8.

Design of concentrated winding by modular approach [17], distributed winding of Bar-Wound type [18][24], and 3D printed coils [19][20] have been reported as the proven methods to increase the power density, and mass production of the stators can be expedited as well. An efficient cooling methodology that aids the capabilities of current density and electric loading of the motor [32]-[35], [40] would further improve the power density of

the motor. Typical values of current densities of PMSM under continuous operation have been shown in TABLE 2.6.

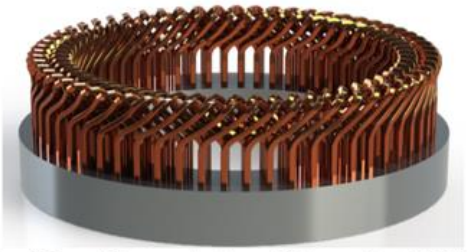

Bar-Wound Stator winding of Chevy Spark 2013

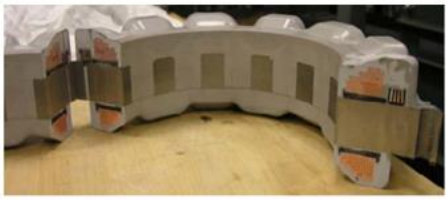

Cross-sections of stator of 2010 Prius IPM generator

3D Printed Coils by Additive Drives

Figure 2.8. Design trend in stator windings of PMSMs for electric vehicle traction applications.

More insights into doubly salient machines such as flux switching machine (FSM), switched reluctance machine (SRM), and doubly salient permanent magnet machine (DSPM) are detailed in Chapter 3.

2.3. Landscaping and Review of Traction Inverters

The current state of the art of traction inverters has been reviewed in this section. A handout [1] from the U.S. Department of Energy (DoE) has listed key targets for traction motor and Power Electronics Inverter Module (PIM) of the electric drive system for the years 2020 and 2025 are shown in TABLE 2.1. DoE targets for key electrical and thermal specifications have been listed in TABLE 2.6 and TABLE 2.7.

TABLE 2.6: DOE TARGETS FOR KEY ELECTRIC SPECIFICATIONS [1]

Peak Power (kW)	200
Continuous Power (kW)	110
Battery Operating Voltage (V_{dc})	850-1100
Voltage Rating (V)	1200
Maximum Device Current (A)	200
Maximum Current (A)	800
Switching Frequency (kHz)	30-50
Maximum Efficiency	>98
Power Factor	>0.6

TABLE 2.7: DOE TARGETS FOR KEY THERMAL SPECIFICATIONS [1]

Maximum Junction Temperature (℃)	250
Ambient Operating Temperature (℃)	-40 to +125
Storage Temperature (℃)	-40 to +125
Maximum Cooling System Flow Rate (lpm)	10
Maximum Coolant Inlet Temperature (°C)	85
Maximum Inlet Pressure (Psi)	25
Maximum Inlet Pressure Drop (Psi)	>98
Volume (liters)	2
Mass (kg)	4

This reference may provide an opportunity for the research community of Original Equipment Manufacturers (OEM) and academia to enhance the infrastructure of electric

mobility. These targets have been set to envision an extended range in mileage of the electric vehicles by improving the performance of the various components involved in electric vehicle traction applications at the device level.

Several reviews of state of the art of traction inverter have highlighted the necessity of wide bandgap (WBG) devices to meet the higher switching frequency requirements have been focused on either all-electric or plug-in hybrid or hybrid vehicles [41], [42]. Different topologies of traction inverters and power electronic components employed in battery-operated electric vehicles and hybrid electric vehicles at General Motors have been reviewed in numerous papers [43-45]. However, a trend in key design matrices of traction inverters hasn't been reviewed extensively in the existing literature. An extensive list of specifications of traction inverters employed in Battery Operated Electric Vehicles (BEV), Hybrid Electric Vehicles (HEV), Plugin Hybrid Electric Vehicles (PHEV), and Fuel Cell Electric Vehicles (FCEV) have been reviewed in this chapter. Key specifications of electric vehicles listed in TABLE 2.8 have been profiled based on Volumetric Power Density (VPD) and Gravimetric Power Density (GPD) as shown in Figure 2.9 and Figure 2.10. Area of the bubble in the plot is proportional to the power rating of the traction inverter. A power factor of 0.6 has been considered to estimate the kW rating of the traction inverter.

TABLE 2.8: SPECIFICATIONS OF COMMERCIALLY AVAILABLE TRACTION INVERTERS

	EV Type	Motor Type	Power (kW or kVA)	DC Link Voltage (V)	VPD (kW/L)	GPD (kW/kg or kVA/kg**)	Device	Cooling Methodology
Jaguar I-Pace 2019 [6]	BEV	PMSynRM	300* kW	500	32.68	36.45	Si IGBT	Water-Glycol
Nissan Leaf 2019 [6]	BEV	PMSynRM	140* kW	450	4.21*	12.55	Si IGBT	Water-Glycol
Tesla M3 2018 [6]	BEV	PMSynRM IM	344* kW	430	27.4*	71.51**	SiC MOSFET	Water-Glycol
Chevy Bolt 2017 [7]	BEV	PMSynRM	153 kVA	350	19.61*	15.93*	Si IGBT	Water-Glycol
Toyota Prius 2016 [8]	PHEV	PMSynRM	162.2* kW	600	11.5	16.7	Si IGBT	-
Audi e-Tron 2016 [6]	PHEV	IM, IM	75* kW	600	9.375	7.5	Si IGBT	Double Sided WEG
BMW i3 2016 [8]	BEV	PMSynRM	125	355	9.375	14.1	Si IGBT	-
Chevy Volt 2016 [9]	PHEV	PMSynRM	180*	360	17.3*	21.7**	Si IGBT	Double Sided WEG
Cadillac CT6 2016 [10]	PHEV	IPMSM	215*	360	23*	16.5**	Si IGBT	Double Sided WEG
Tesla S 2015 [10]	BEV	-	320* kW	430	47-50*	52-55*	Si IGBT	-
Honda Accord 2014 [8]	HEV	IPMSM	-	700	-	-	Si IGBT	-
Chevy Spark 2014 [7]	BEV	PMSM	140 kVA	350	10.68*	10.29**	Si IGBT	-
Toyota Camry 2013 [8]	HEV	PMSynRM	-	650	11.5	12.7	Si IGBT	WEG
Nissan Leaf 2012 [10]	BEV	PMSynRM	80 kW	375	7.1	4.94	-	-
Sonata HSG 2012 [8]	HEV	PMSM	23 kW	270	7.3	6.9	Si IGBT	Ethylene Glycol
Toyota Prius 2010 [16]	HEV	IPMSM	-	650	5.9	6.9	Si IGBT	Water-Glycol
Lexus 2008 [16]	HEV	IPMSM	-	650	10.6	7.7	Si IGBT	Double Sided W-G
Toyota Camry 2007 [8]	HEV	IPMSM	70 kW(peak)	650	11.7	9.3	Si IGBT	Water-Glycol
Honda Accord 2006 [8]	HEV	PMSM	12 kW	-	2.4	2.9	Si IGBT	Air cooled Heat Sink
Toyota Prius 2004 [16]	HEV	IPMSM	50 kW	500	3.8	4.5	Si IGBT	Water-Glycol

-unknown, *estimated, IM: Induction Motor, PMSynRM: Permanent Magnet Assisted Synchronous Reluctance Machine, IPMSM: Internal Permanent Magnet Machine, W-G: Water-Glycol, WEG: Water-Ethylene-Glycol

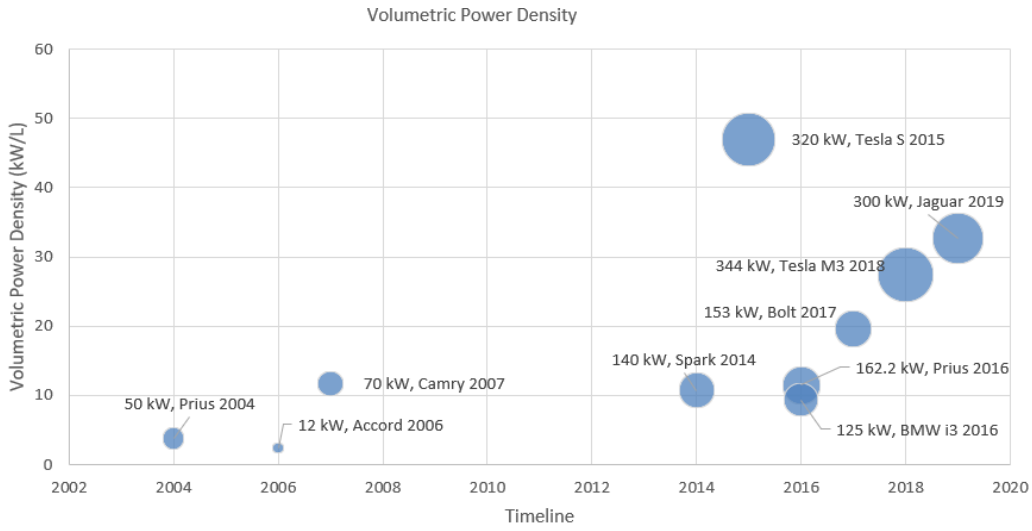

Figure 2.9. Trend in volumetric power density of commercially available traction inverters from the year 2004 to 2020 [2-16].

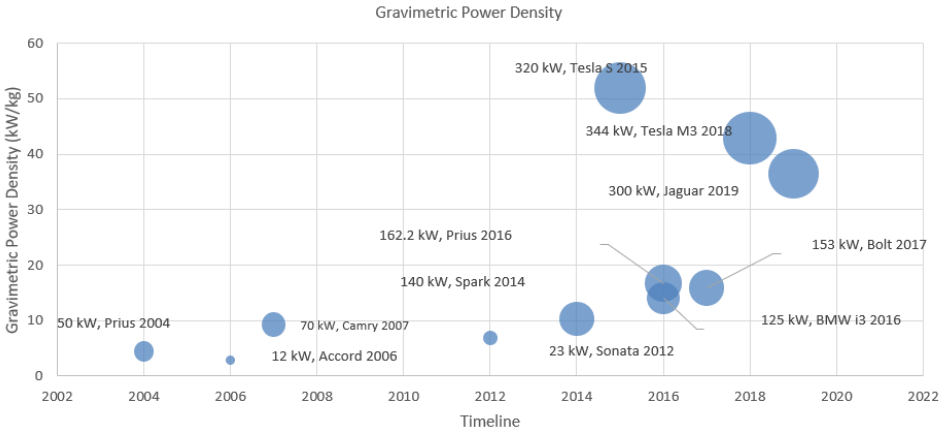

Figure 2.10. Trend in gravimetric power density of commercially available traction inverters from the year 2004 to 2020 [2-16].

2.3.1. Selection of Topology of Traction Inverters

The way the traction inverter's circuit is set up depends on how the motor's coils are arranged. For a motor with open-ended winding and six terminals out, a dual inverter setup is often chosen [46]. In the case of switched reluctance motors, an asymmetrical bridge inverter topology is used [47]. If the goal is to power AC traction motors, the classic three-phase traction inverter topology is a good fit. Using fewer switching devices in a three-phase inverter can enhance Volumetric Power Density (VPD) and Gravimetric Power Density (GPD) but opting for a dual inverter setup with an optimized design can double these measures [48].

The way the system is controlled is illustrated in Figure 3 and involves several levels. There's an outer loop for speed, another loop for torque, and inner loops for current. Two established methods for controlling speed below the rated level are Maximum Torque Per Ampere (MTPA) and Field Weakening (FW) control [49-51]. To determine the motor's torque constant in N/m and speed constant in V/rpm, tests like the static torque test (locked rotor test) and back EMF test (open circuit test) are conducted on the traction motor. These constants are then used in the MPTA and FW control algorithms.

Traction motors need to work effectively across a wide range of speeds, especially in the constant power region. This means that when the fundamental frequencies at which traction motors operate are higher, the traction inverters need to switch at higher frequencies too. To ensure stability while the motor operates at various speeds and torques, it's important to set the right sampling rates for the phase currents. Since the fundamental frequency of traction motors is higher than that of conventional motors, it calls for increased switching frequencies. This, in turn, necessitates higher sampling rates for the

current measurements and the subsequent control loops that manage the motor's performance.

The choice of sampling rates is a crucial part of designing the control system for the motor's speed and torque. It's essential for the motor to remain stable and responsive. The required sampling rates for different control loops in the speed and torque design must align with the sampling frequencies defined in equations (2.2) to (2.6). These equations essentially provide the guidelines for determining the appropriate sampling frequencies to achieve reliable and effective control of the traction motor.

$$\text{Current loop sampling frequency}(f_i) = f_{sw} \tag{2.2}$$

$$\text{Speed loop sampling frequency}(f_n) = \frac{1}{5} \times f_{sw} \tag{2.3}$$

$$\text{Current loop cross over frequency}(f_{cri}) == \frac{1}{10} \times f_{sw} \tag{2.4}$$

$$\text{Speed loop cross over frequency}(f_{crn}) == \frac{1}{10} \times f_{cri} \tag{2.5}$$

$$\text{Torque loop cross over frequency}(f_{crn}) == \frac{1}{10} \times f_{cri} \tag{2.6}$$

MTPA and FW controllers generate a pair of d-axis and q-axis currents which will be fed to the inner current control loop. Inner current controller loops must be sampled at the switching frequency of the inverter. A flag has been set to choose the reference signals of currents either from the MTPA controller or FW controller based on the speed and torque requirements. The inner current controller chooses the reference currents generated by the MTPA controller for below-rated speeds or else reference currents generated by the FWA controller will be fed to the inner current controller. Characteristics of permanent magnet-

based traction motor are defined by current and flux dependent instantaneous voltage equations (2.7) and (2.8).

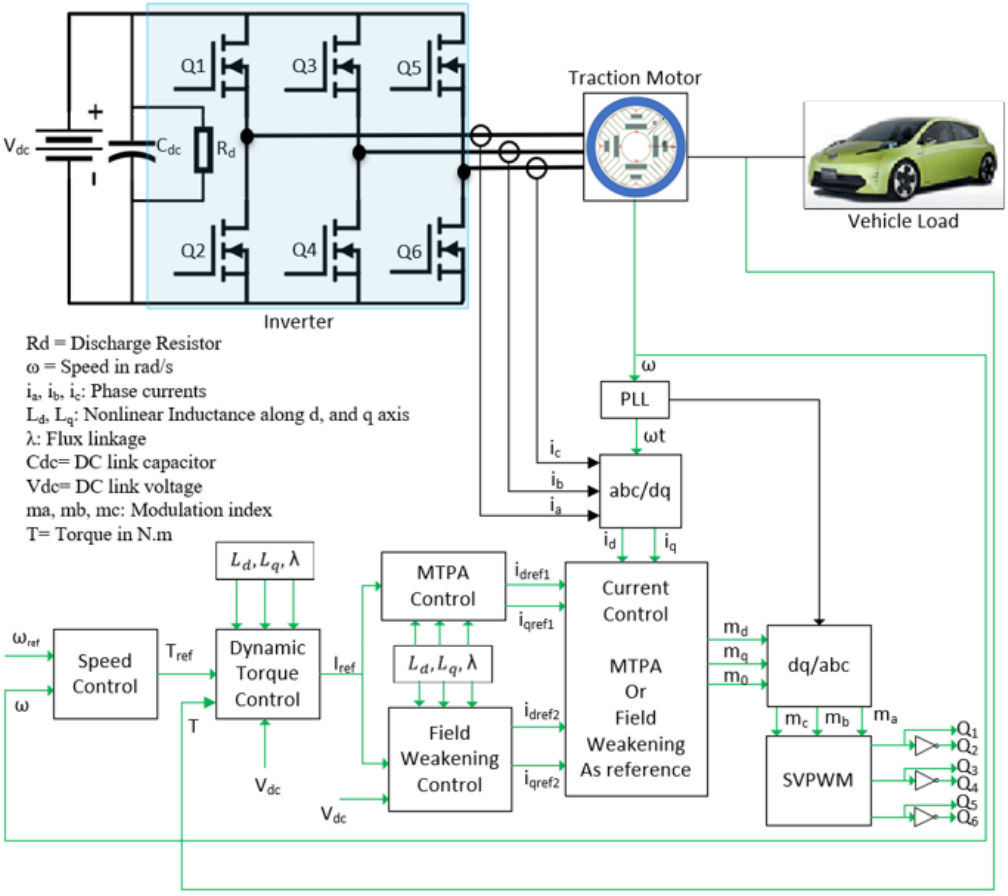

Figure 2.11. Simplified schematic of speed and torque control block diagram of traction inverter.

2.3.2. Review of Traction Motor Drive Control Methodologies

A review of traction motor drive control methods is presented in this section. Based on saliency of the motor, different torque or current control methods are employed. From the plant model of the PMSM, voltages in synchronous reference frame are expressed as,

$$v_d^e = Ri_d^e - \omega_e L_q i_q^e + \frac{d}{dt}(L_d i_d^e) \tag{2.7}$$

$$v_q^e = Ri_q^e + \omega_e L_d i_d^e + \frac{d}{dt}\left(L_q i_q^e\right) + \omega_e \psi_{pm} \tag{2.8}$$

At steady state, the rate of change of flux linkages (transient voltages) and drop due to resistance are neglected. Thus, DQ voltages are approximated as,

$$v_d^e = -\omega_e L_q i_q^e \tag{2.9}$$

$$v_q^e = \omega_e (L_d i_d^e + \psi_{pm}) \tag{2.10}$$

Thus, magnitude of terminal voltage of the motor is expressed as,

$$\hat{V}_s = \sqrt{(\omega_e L_q i_q^e)^2 + (\omega_e (L_d i_d^e + \psi_{pm}))^2} \tag{2.11}$$

An expression for mechanical speed considering number of poles is expressed as,

$$\omega_m = \omega_{base} = \left(\frac{2}{P}\right) \frac{V_{max}}{\sqrt{(L_q i_{q\mathrm{m}}^e)^2 + (L_d i_{d\mathrm{m}}^e + \psi_{pm})^2}} \tag{2.12}$$

The torque for the PMSM with saliency such as IPM and PM-SyRM is expressed as,

$$T_e = \frac{3}{2} P(\psi_{pm} i_q^e + (L_d - L_q)\, i_d^e i_q^e) \tag{2.13}$$

Similarly, the torque for PM based machines with non-saliency such as surface permanent magnet machine (SPM) and flux switching permanent magnet machine (FSPM) is expressed as,

$$T_e = \frac{3}{2}P(\psi_{pm} i_q^e + (L_d - L_q)\, i_d^e i_q^e) \approx \frac{3}{2}\left(\frac{P}{2}\right)\left(\psi_{pm} i_q^e\right) \tag{2.14}$$

The torque capability of the motor is limited by the current carrying capability of the inverter and thermal rating of the motor whichever is lower, expressed as a current constraint (2.15). The rated current of the inverter is usually 2 to 3 times of the electric machine's capability during acceleration.

$$Current\ constraint: i_q^e = \sqrt{\hat{I}_s^{\,2} - i_d^{e\,2}}\ \ \&\ \hat{I}_s \leq I_{max} \tag{2.15}$$

For the machines with saliency, the maximum torque is achieved by controlling both q-axis current and d-axis current (negatively). A maximum torque per Ampere current control strategy [57] is employed in the case of IPM and PM-SyRM. Constant torque angle control in which d-axis current is zero is employed for machines without saliency such as SPM and FSPM [57-59].

From the expressions of mechanical speed and electromagnetic torque, the speed is limited by maximum voltage across the inverter terminals or phase voltage of the motor. An alternative way to increase the speed without increasing voltage is by injecting d-axis flux linkages against PM flux linkages to weaken overall flux in the airgap. Thus, speed control above rated speed is achieved by increasing d-axis current negatively without increasing voltage across inverter or motor terminals i.e induced EMF reaches maximum voltage and remains constant at rated speed. Speed control below rated speeds is achieved by maintaining constant ratio of voltage and resultant flux linkages. This type of field weakening control strategy is also called maximum torque per flux (MTPF) control. The

voltage constraint of the electric machine drive system is expressed as (2.16) is a modified form of (2.12).

$$Voltage\ constraint: \frac{\left(\left(\frac{\psi_{pm}}{L_d}\right)+i_d^e\right)^2}{\frac{{V_s}^2}{(\omega_e L_d)^2}} + \frac{i_q^{e\,2}}{\frac{{V_s}^2}{(\omega_e L_q)^2}} = 1\ \&\ V_s \leq V_{max} \tag{2.16}$$

Characteristic current of an electric machine with PMs is expressed as (2.17), a ratio of flux linkage constant and d-axis inductance. It is a key specification of demagnetization index, defines maximum allowable current along d-axis without affecting performance of PM.

$$Characteristic\ Current: I_{ch,d} = \frac{\psi_{pm}}{L_d} \tag{2.17}$$

Considering constraints of current, voltage, and characteristic current, speed and torque control capability curves of the motor drive system has been plotted as shown in figure 2.11. Maximum torque is achieved along the MTPA and MTPF curve of the plot. Infinite speeds are possible for machines with characteristic current is less than maximum but constrained by mechanical abilities of the electric machine. In this regard, maximum torque per voltage control is implemented in the filed weakening regime by maintaining d-axis current as constant to avoid infinite speed operating point [60].

For the machines with non-saliency behavior, the current and speed circles are resembled in circular shape. Maximum torque is achieved by constant torque angle control along q-axis and field weakening is achieved by MTPF and MTPV control strategies depending on the magnitude of characteristic current [60]. More insights into the current control strategies are detailed in Chapter 5 and Chapter 6.

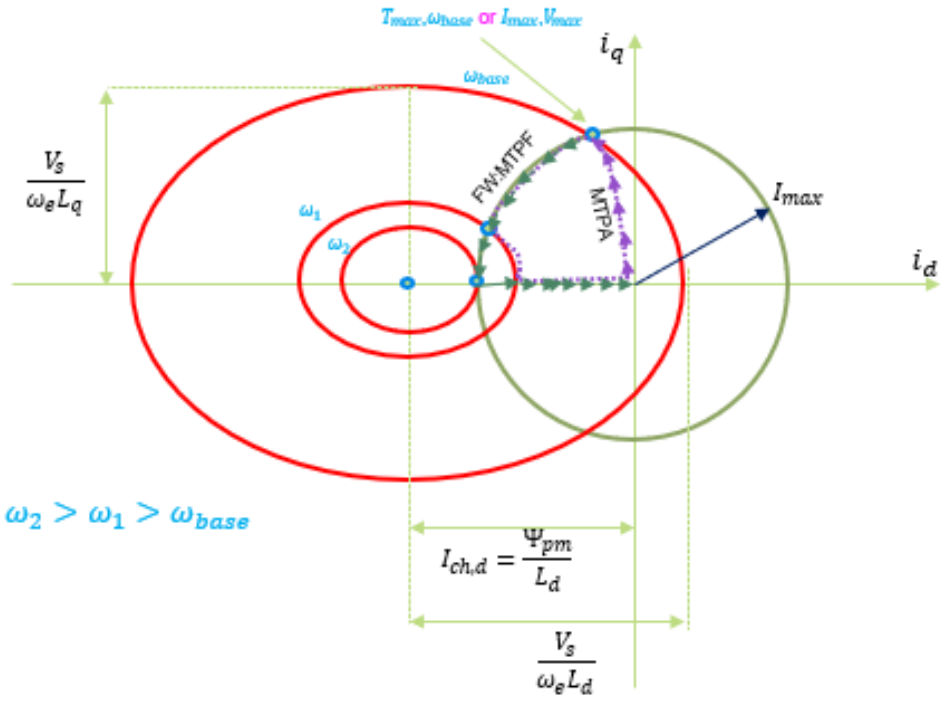

Figure 2.12. Plot of i_d^e versus i_q^e illustrating constraints, speed, and torque capabilities for the PMSM (IPM or PM-SyRM): MTPA trajectory for speeds below rated speed and MTPF field weakening trajectory for the speeds above rated speed [57-59].

A summary of generation of reference currents for salient and non-salient pole PMSMs is reported in TABLE 2.9. and TABLE 2.10. In a model-based approach, the reference currents reported in the tables are generated as look-up tables considering the effect of saturation of flux linkages using post-processing features of finite element analysis software such as design of experiments (DoE). Thus, a high-fidelity control trajectory is achievable employing model-based design methodology.

TABLE 2.9: EXPRESSIONS FOR REFERENCE CURRENTS EMPLOYING MTPA CONTROL

	SPM/FSPM [58-59]	IPM/PM-SyRM [57]
i_d^e	0	$\frac{\Psi_{pm} - \sqrt{{\Psi_{pm}}^2 + 8(L_q - L_d)^2 \hat{I}_s^2}}{4(L_q - L_d)}$
i_q^e	$\hat{I}_s$	$\sqrt{\hat{I}_s^2 - {i_d}^2}$

TABLE 2.10: EXPRESSIONS FOR REFERENCE CURRENTS EMPLOYING FW CONTROL

	SPM/FSPM [58-59]		IPM/PM-SyRM [57]
	CCCP [57]	CVCP [58]	VCLMT [57]
i_d^e	$-\frac{\hat{I}_s}{\omega_e}\sqrt{{\omega_e}^2 - {\omega_{base}}^2}$	$\frac{\omega_{base}}{\omega_e}\frac{\Psi_{pm}}{L_d} - \frac{\Psi_{pm}}{L_d}$	$\frac{-\Psi_{pm}L_d + \sqrt{(\Psi_{pm}L_d)^2 - \left({L_d}^2 - {L_q}^2\right)\left({\Psi_{pm}}^2 + {L_q}^2\hat{I}_{max}^2 - \left(\frac{v_{max}}{\omega_e}\right)^2\right)}}{\left({L_d}^2 - {L_q}^2\right)}$
i_q^e	$\frac{\omega_{base}}{\omega_e}\hat{I}_s$	$\frac{\omega_{base}}{\omega_e}\hat{I}_s$	$\sqrt{\hat{I}_s^2 - {i_d}^2}$

CCCP: Constant Current Constant Power, CVCP: Constant Voltage Constant Power, and VCLMT: Voltage & Current Limited Maximum Torque

2.3.3. Selection of Components for Traction Inverter

Busbars: The power loop inductance of the traction inverter plays a crucial role in determining the switching frequency and consequently affects the control of the vehicle's speed. This inductance can introduce delays in the turn-on and turn-off times of the switching devices. Even a small delay in these times, particularly in MOSFETs, can negatively impact the inverter's performance at higher frequencies [52]. To address this issue, using laminated busbars separated by insulating material can be quite effective. These busbars help significantly decrease the loop inductance, which, in turn, improves the controller's stability and enhances power density. These busbars can be tailored to match the specific packaging needs of the traction inverter. An example of a custom laminated

busbar developed by Rogers Corp, Inc., is depicted in Figure 2.12. This innovation has successfully reduced the power loop inductance to 12 nH [53].

Power Modules: When selecting power modules, it's important to opt for those that exhibit minimal ringing in switching voltages. These modules should also be capable of functioning at higher switching frequencies to produce elevated fundamental frequencies. Furthermore, they should accommodate higher rated current and voltage in order to align with the targets set by the DoE. Having over-current, over-voltage, and temperature sense terminals on these power modules would be beneficial when assembling the components [54] as one package. The overall design and size of the power modules, including the gate driver, should prioritize being compact while meeting the objectives for high power density.

Capacitors: When choosing capacitors, it's important to focus on their ability to effectively manage the fluctuations in current and voltage, particularly in the presence of spatial harmonics during both motoring and regeneration modes. To align with the Volumetric Power Density (VPD) and Gravimetric Power Density (GPD) targets, capacitors should be designed with minimal volumetric size and weight. Additionally, the form factor of the capacitor has a significant impact on how the entire traction inverter is packaged. To avoid issues like bondage failures caused by improper soldering, capacitors with screw-type connections that can be fitted onto customized busbars are recommended. For automotive applications, polypropylene capacitors of coaxial type are a suitable choice. These capacitors offer advantages like high peak ripple absorption, lightweight design, and compact size, making them well-suited for automotive applications.

Coolant: For high-power traction motors, liquid cooling is essential. A mix of Glycol, Ethylene, and Water is often pumped through cooling plates to keep the power modules at the right temperature during heavy use. Using micro-finned cooling plates improves heat absorption by creating more surface contact with the power modules. Opting for double-sided cooling instead of single-sided can further boost cooling capacity and enhance Volumetric Power Density (VPD) and Gravimetric Power Density (GPD). An example from Wolfspeed, a dual inverter for traction applications (Figure 2.13), demonstrates the effectiveness of double-sided cooling, achieving a power density of 72.5 kW/L [55].

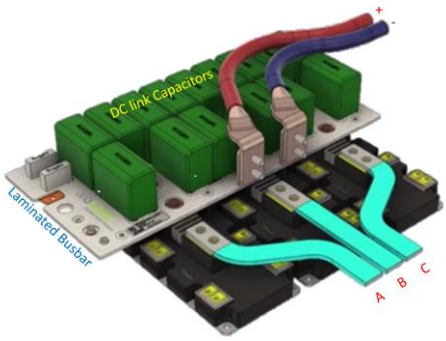

Figure 2.13. Conceptual 3D image of ROLINX CapLink busbars customized for WolfSpeed XM3 Power Modules [55].

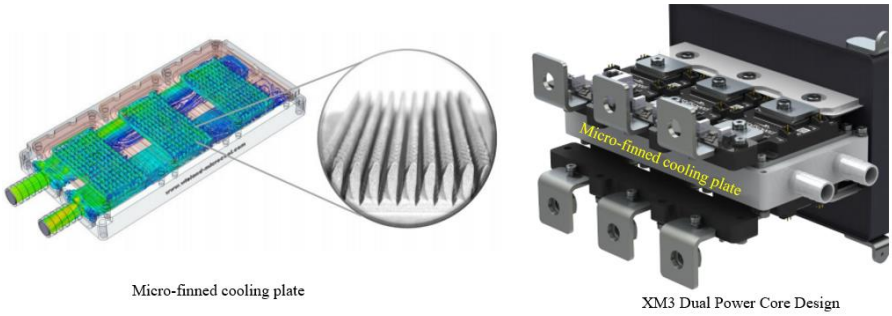

Figure 2.14. Conceptual 3D images of micro-finned cold plate and Wolfspeed XM3 Dual power core inverter [56].

CHAPTER 3: DOUBLY SALIENT MACHINES

3.1. Introduction

Chapter 3 provides a detailed analysis of mechanically doubly salient machines that are shown in figure.3.1. and figure.3.2. In particular, magnet-free doubly salient machines, such as the flux switching machine and the switched reluctance machine, are discussed in Sections 3.2 and 3.3. Additionally, two different variants of doubly salient machines with permanent magnets, including the doubly salient permanent magnet machines introduced by Thomas Lipo and Charles Joe Flynn, are presented in Sections 3.4 and 3.5. The analysis and principle of operation of a special doubly salient permanent magnet machine, which employs parallel path magnetic technology and is the focus of this dissertation, are detailed in Section 3.6.

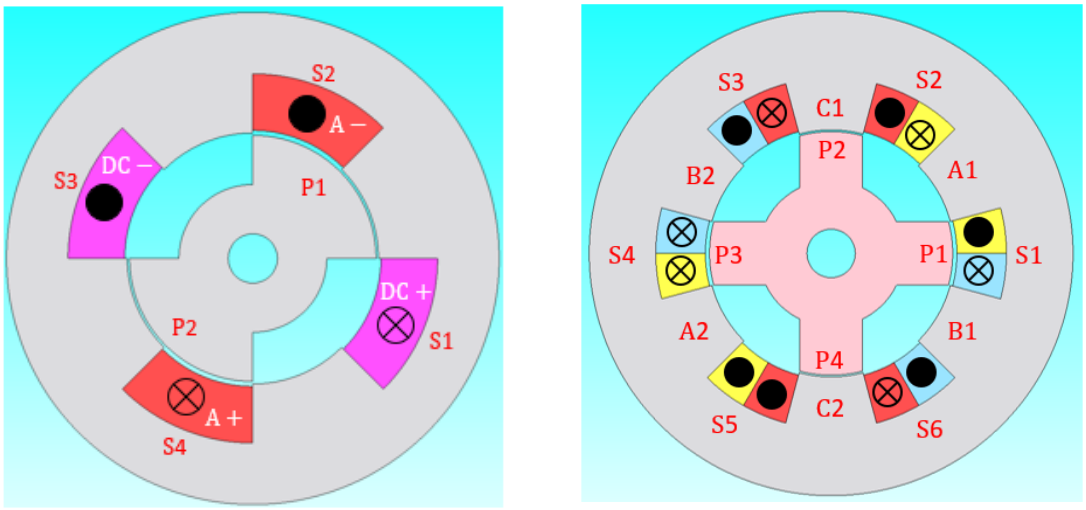

(a) (b)

Figure.3.1. FEA schematics of magnet-free mechanically doubly salient machines

(a). Flux switching machine (b). Switched reluctance machine.

Definition of doubly saliency has been attributed to the mechanically doubly salient shape of the stator and rotor with protrusions and depressions around the inner and outer

circumference of the respective cores. The analysis of these doubly salient machines is used to explain the principle of operation of a special doubly salient machine in Section 3.6, using frequency domain methodology.

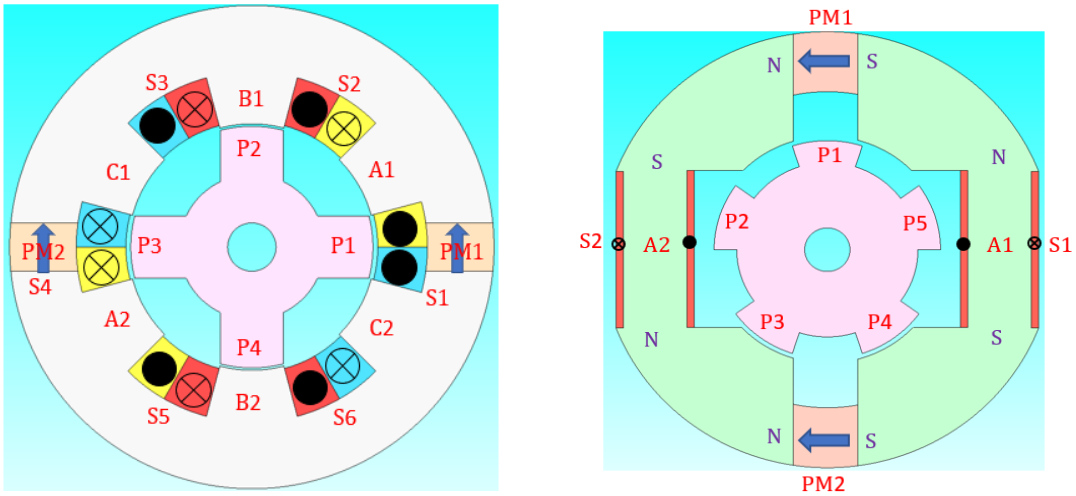

(a) (b)

Figure.3.2. FEA schematics of mechanically doubly salient machines with permanent magnets (a). Doubly salient permanent magnet machine (b). PPMT machine.

3.2. Flux Switching Machine

In 1999, Charles Pollock proposed a flux switching machine (FSM) with a 1-phase, 4-slot, and 2-rotor protrusion design [61]. The FSM's topology is depicted in figure 3.3, and it features a DC field winding and an armature winding, both housed in a pair of slots in the stator. This particular FSM topology is considered a DC motor without magnets or brushes because the stator carries both the DC and armature windings and does not require brushes or a commutator to feed or collect current from the stationary armature winding.

The slots in the FSM are positioned at 90° intervals spatially and labeled S1, S2, S3, and S4. A DC current is used to excite the field winding, while a bipolar or alternating current of square shape is used to excite the armature winding. The DC field winding is

embedded in slots S1 and S3, which are 180° apart, while the armature winding is located in slots S4 and S2, also 180° apart. As a result, the FSM features two fully-pitched, concentrated-wound coils. The FSM's rotor has two pole protrusions, which are equivalent to four magnetic poles.

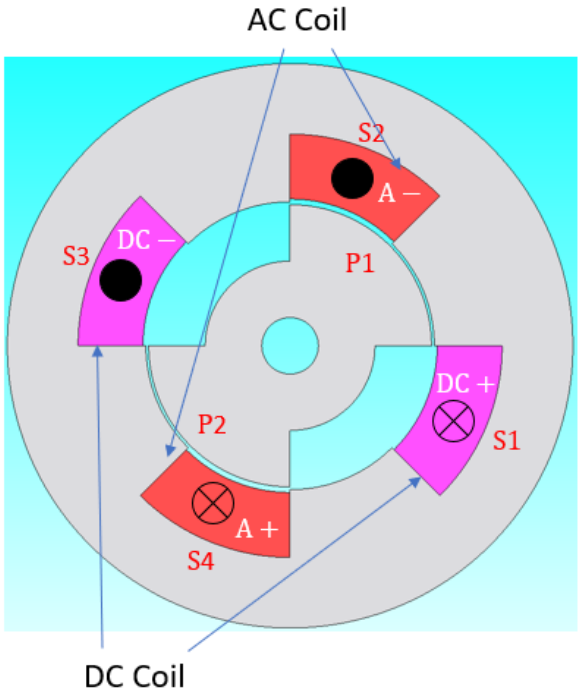

Figure.3.3. 2D FEA schematic of FSM with 4 slots to house field winding and armature winding in stator and 2 rotor protrusions.

3.2.1. Principle of operation of the FSM

Open circuit flux linages with armature winding while field winding is excited with DC current for various rotor positions has been shown in figure.3.4. The flux created by the DC field winding follows a low reluctance path through the salient pole protrusions of the rotor and links with the armature winding via the airgap. The maximum flux linkages with the armature winding occur at positions 1 and 3 when rotor pole P1 aligns with the teeth of

the stator segment, while the minimum flux linkages occur at position 2 when rotor pole P1 aligns with slot S3 of the DC field winding in the stator. Figure 3.5 shows the properties of the flux linkages with the armature winding for different rotor positions. As a result, the rate of change of flux linkages with the armature winding generates induced voltages or back EMF.

During full-load operation, the armature winding is excited with bipolar or alternating current of square shape. The fully-pitched DC field winding and concentrated armature windings generate magnetomotive forces perpendicular to each other, producing a torsional force on the rotor and causing it to rotate in the respective direction. Figure 3.6 shows the exciting current through the armature winding, the properties of the flux linkages with the armature and DC field windings, the back EMF with the armature winding, and the respective torque versus rotor position.

The flux linkages with the armature winding have been observed to be bipolar. However, the transition of the excited armature winding current from positive to negative, with high di/dt, results in large spikes in back EMF, which is not safe for bearings. Despite significant torque ripple, an average positive torque of 7.44 Nm has been observed.

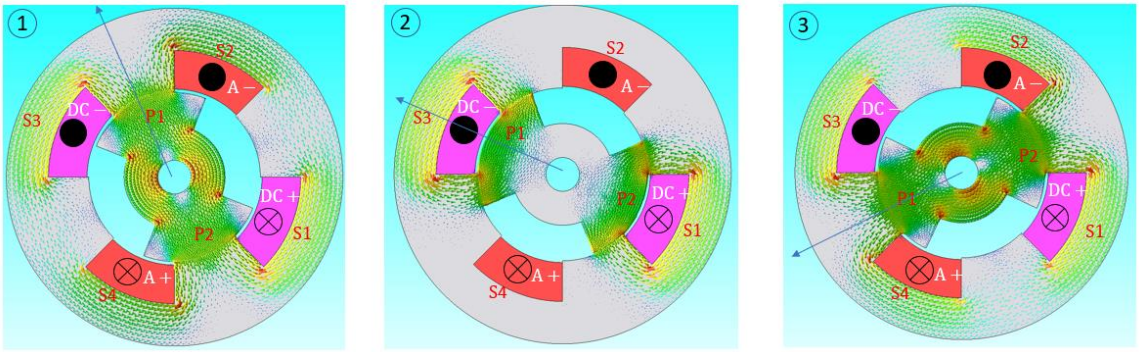

Figure.3.4. Model of FSM for 2D FEA and properties of flux linkages with armature winding at different rotor positions.

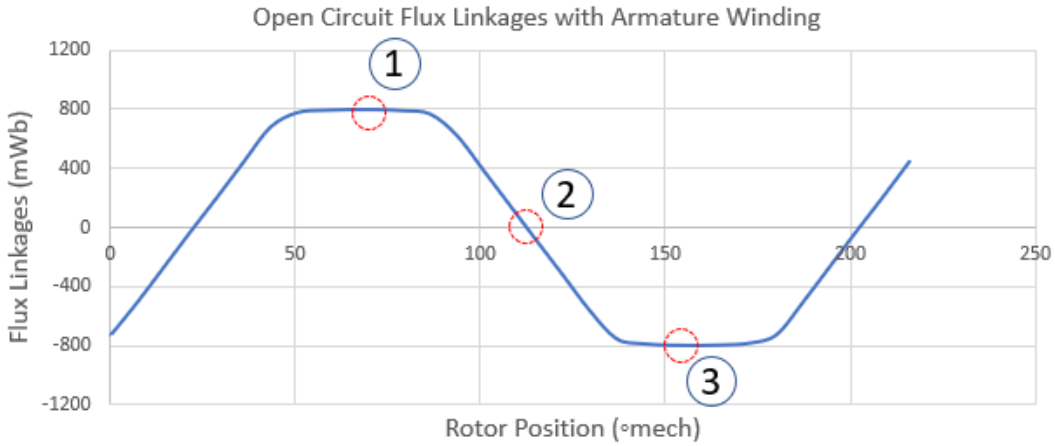

Figure. 3.5. Plot of flux linkages vs rotor position, depicting properties of flux linkages with armature winding under open circuit condition.

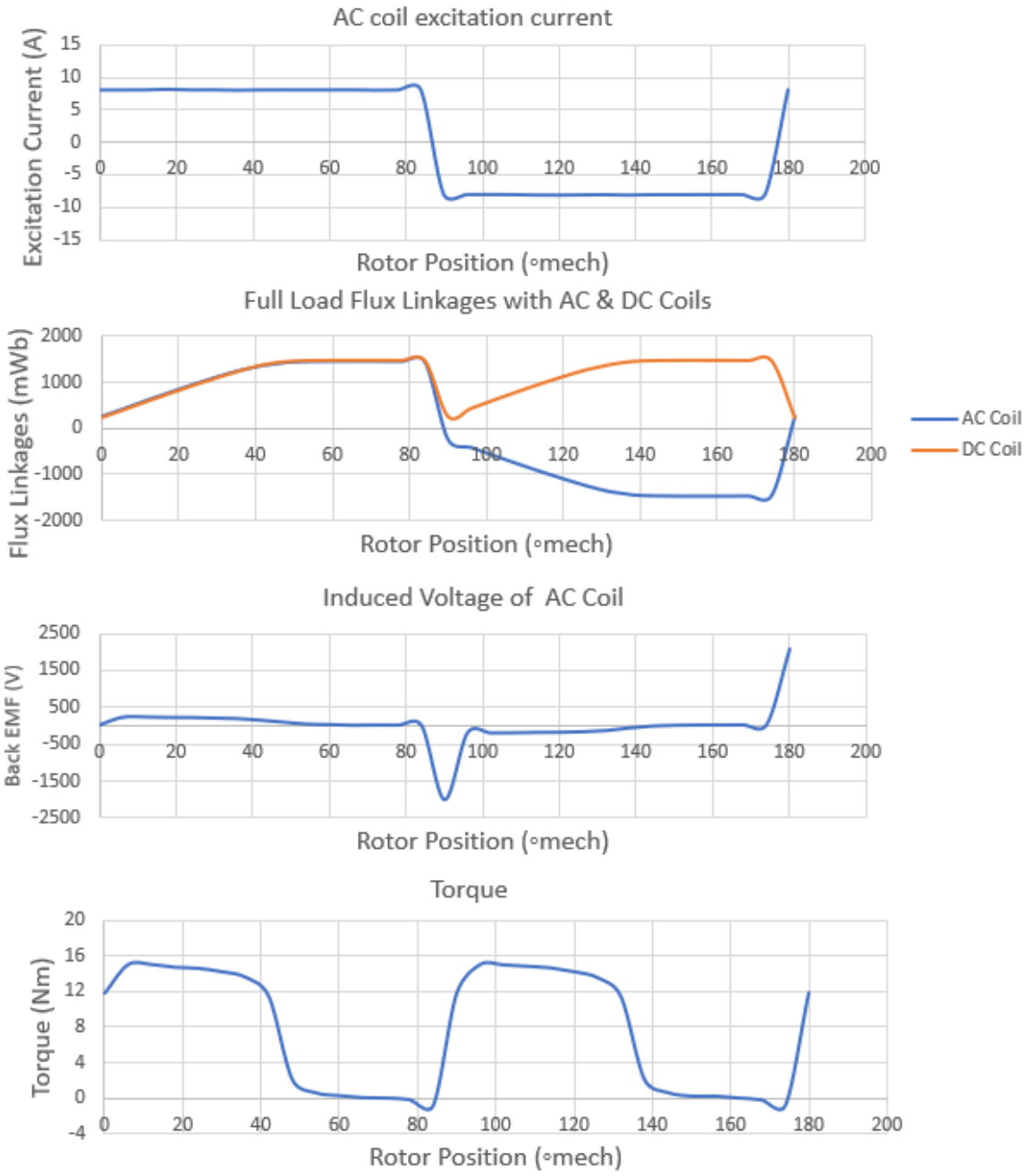

Figure.3.6. Plots of current through armature winding, full load flux linkages with AC/armature winding and DC field winding, back EMF, and torque versus rotor position for the FSM.

3.3. Switched Reluctance Machine

The switched reluctance machine (SRM) is considered a magnet-free mechanically doubly salient machine because of the saliency in both the stator and rotor. Figure 3.7 shows a 3-phase SRM with 6 slots in the stator and 4 rotor protrusions. The stator slots are denoted as S1, S2, ..., S6, and they are placed spatially 60° apart from each other around the inner circumference of the stator core. Each phase has two concentrated wound coils connected in series, which are denoted as A1, A2, B1, B2, C1, and C2. The two coils under each phase are wound around the teeth of the stator in opposite directions to each other to accumulate the flux linkages with the coils under the respective phase [62].

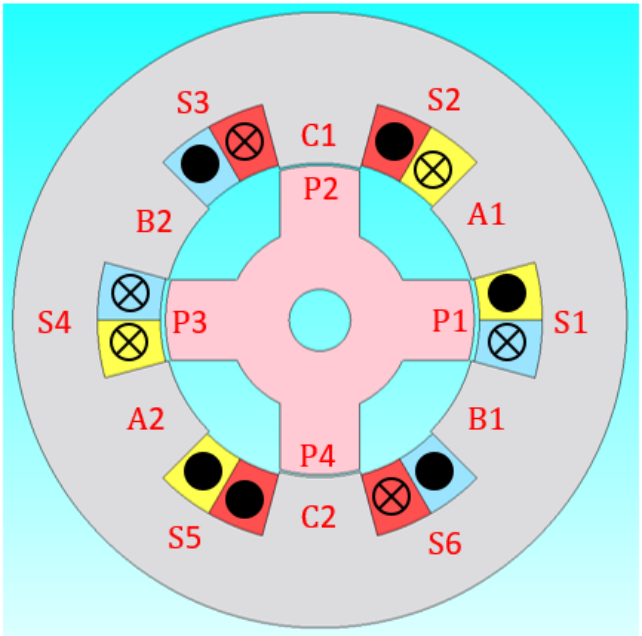

Figure.3.7. 2D FEA schematic of three-phase SRM with 6 slots and 4 rotor protrusions.

3.3.1. Principle of operation of the SRM

The working principle of an SRM is based on the change in magnetic reluctance that occurs depending on the rotor position. The concentrated coils of an SRM are wound in a

manner that generates a magnetomotive force and corresponding flux in the radial direction. Unlike DC machines, synchronous machines, and FSMs, the SRM doesn't have a separate field winding. Each phase of the SRM is excited for 120° electrical to avoid mutual flux linkages with other phases.

Properties of flux linkages versus rotor position for coils under phase-A are shown in Figure 3.8. The coils under phase-A are excited for 120° electrical, as shown in Figure 3.9. The flux linkages and airgap flux density in the airgap due to coils A1 and A2 under phase-A are minimum at rotor positions 1 and 3, where pole P1 aligns with slot S1 and slot S2. The flux linkages and airgap flux density in the airgap due to coils A1 and A2 under phase-A are maximum at rotor position 2, where pole P1 aligns with slot S3 and slot S4. A plot of flux linkages with phase-A versus rotor position is shown in Figure 3.10. Thus, the flux linkages and airgap flux density due to the respective phase depend on the change of the magnetic reluctance with respect to the rotor position.

The three-phase current excitations, flux linkages with coils under respective phases, back EMF due to the rate of change of flux linkages, and respective torque versus rotor position are shown in figure.3.11. A sudden transition in current excitation and respective flux linkages is reflected as a spike in the back EMF. Despite the ripple in the magnitude of the torque, an average positive torque of 4.2 Nm has been observed.

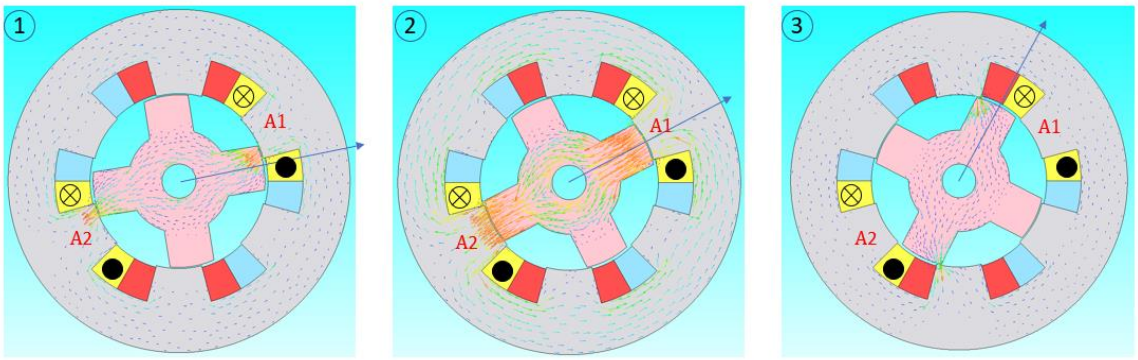

Figure.3.8. Model of SRM for 2D FEA and properties of flux linkages with coils A1 and A2 under phase-A at different rotor positions.

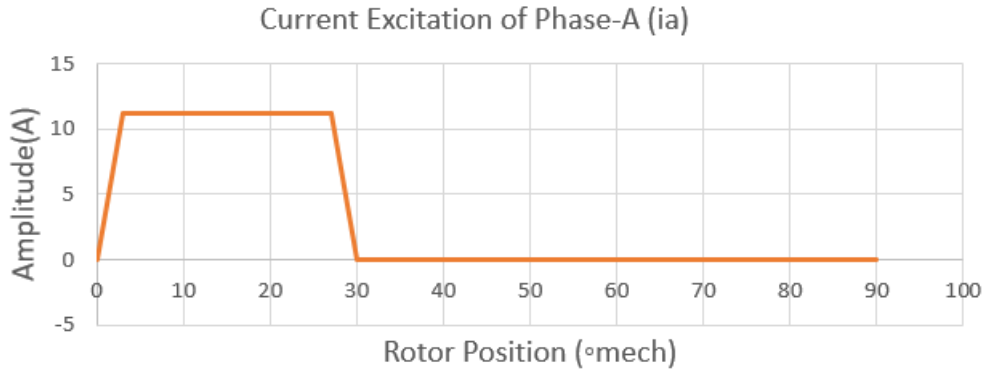

Figure.3.9. Plot of current through coils A1 and A2 under phase-A versus rotor position for the SRM.

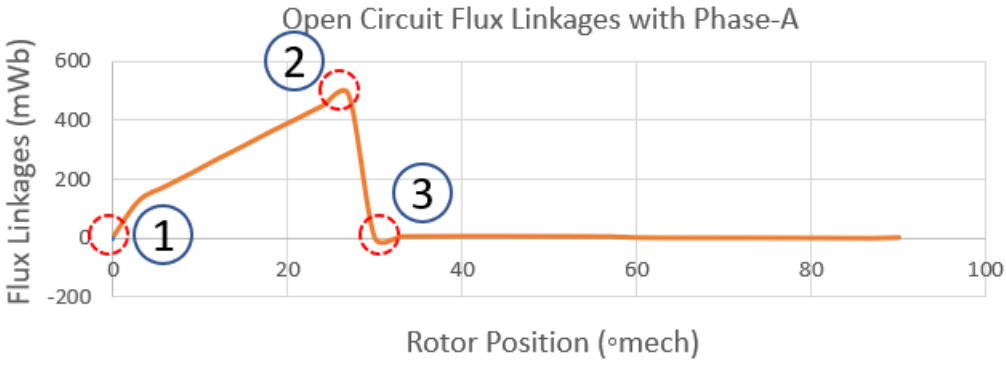

Figure.3.10. Plot of flux linkages with coils A1 and A2 under phase-A versus rotor position for the SRM.

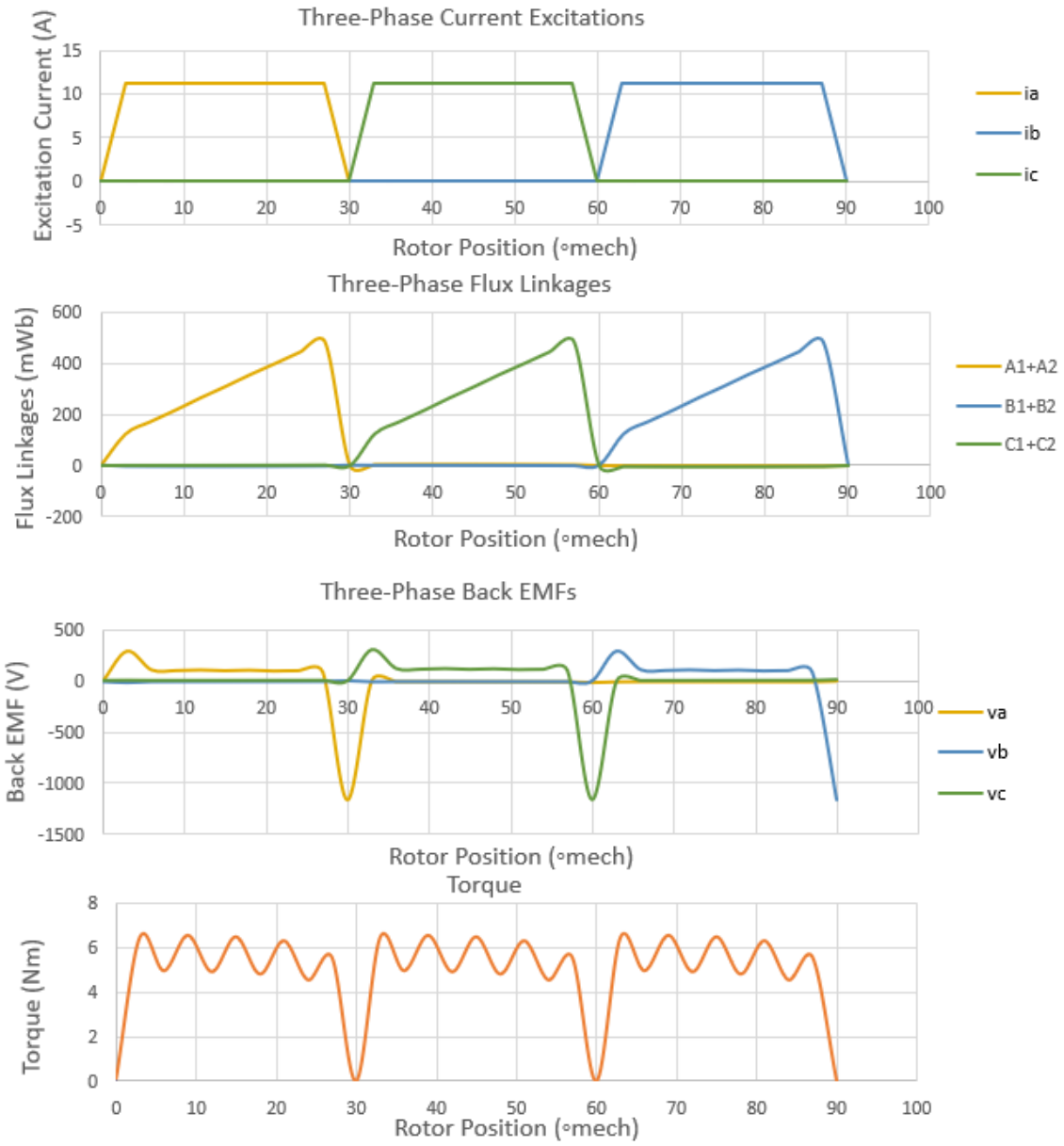

Figure.3.11. Plots of three-phase currents, full load flux linkages with three-phases, back EMF, and torque versus rotor position for the SRM.

3.4. Doubly Salient Permanent Magnet Machine

A DSPM machine with three phases, six slots to house six coils in the stator, four rotor protrusions, and two PMs in the back iron of the stator was introduced in [63], as shown in figure 3.12. This topology of DSPM was intended to replace the field winding in the stator of FSM with PMs. The two PMs are placed in the back iron of the stator core, with one PM placed 180° apart from the other. The stator slots are denoted as S1, S2, ..., S6, and they are placed spatially 60° apart from each other around the inner circumference of the stator core. Each phase has two concentrated wound coils connected in series, which are denoted as A1, A2, B1, B2, C1, and C2. The two coils under each phase are wound around the teeth of the stator in opposite directions to each other to accumulate the flux linkages with the coils under the respective phase. The PMs have been placed spatially 180° apart, separate coils A1, B1, C1 and coils A2, B2, C2 spatially.

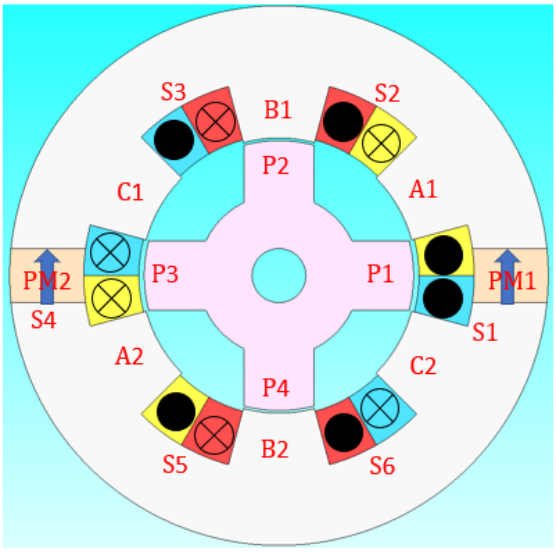

Figure.3.12. 2D FEA schematic of three-phase DSPM with 6 slots and 4 rotor protrusions.

3.4.1. Principle of operation of the DSPM

The working principle of the DSPM can be understood by observing the flux linkages of the coils of the respective phase with respect to the position of the rotor, as shown in figure 3.13. The coils A1 and A2 under phase-A experience maximum flux linkages and contribute to the maximum airgap flux density at positions 1 and 3 where pole P1 aligns with the teeth of the stator core under coils A1 and A2. The coils A1 and A2 under phase-A experience minimum flux linkages and contribute to the minimum airgap flux density at position 2 where pole P1 partially aligns with slots S2 and S4. The properties of flux linkages with coils under phase-A via the airgap and the low reluctance path created by salient poles versus the rotor position are shown in figure 3.14. Thus, flux linkages are unipolar or homopolar irrespective of the position of the rotor.

Under full load operation, a quasi-trapezoidal excitation, as shown in figure 3.15, has been applied to the three phases. The resultant flux linkages with respective phases, the respective back EMF, and torque have been shown in the same figure. A transition in excited currents from positive to negative magnitude reflects a sudden drop in flux linkages, and a spike in the respective back EMFs has been observed. Despite the ripple in the magnitude of the torque, an average positive torque of 15Nm has been observed.

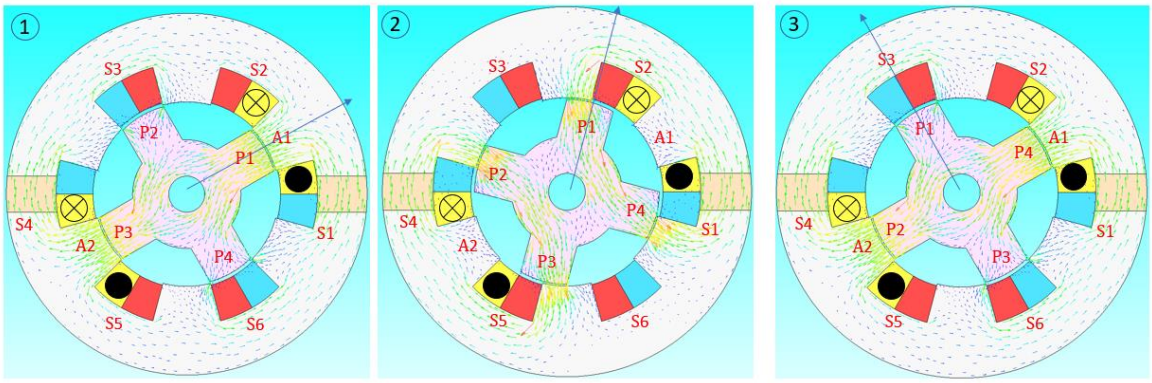

Figure.3.13. Model of DSPM machine for 2D FEA and properties of flux linkages with coils A1 and A2 under phase-A at different rotor positions.

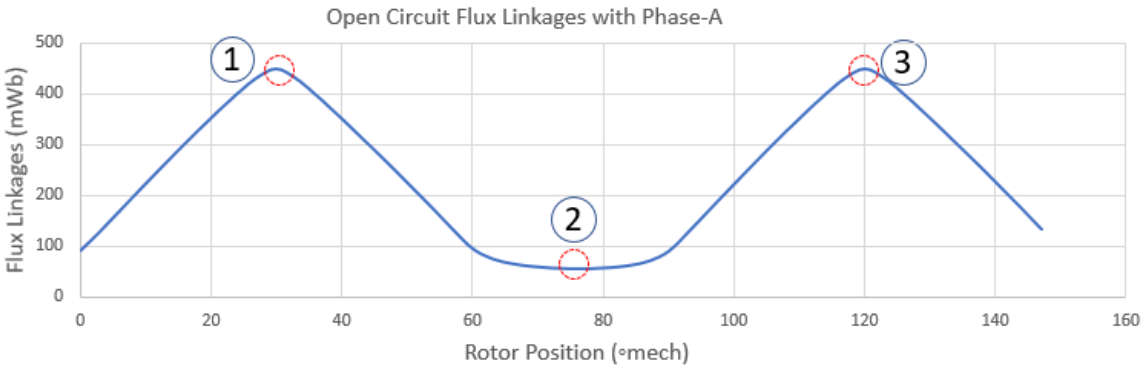

Figure.3.14. Plot of flux linkages with coils A1 and A2 under phase-A versus rotor position for the DSPM.

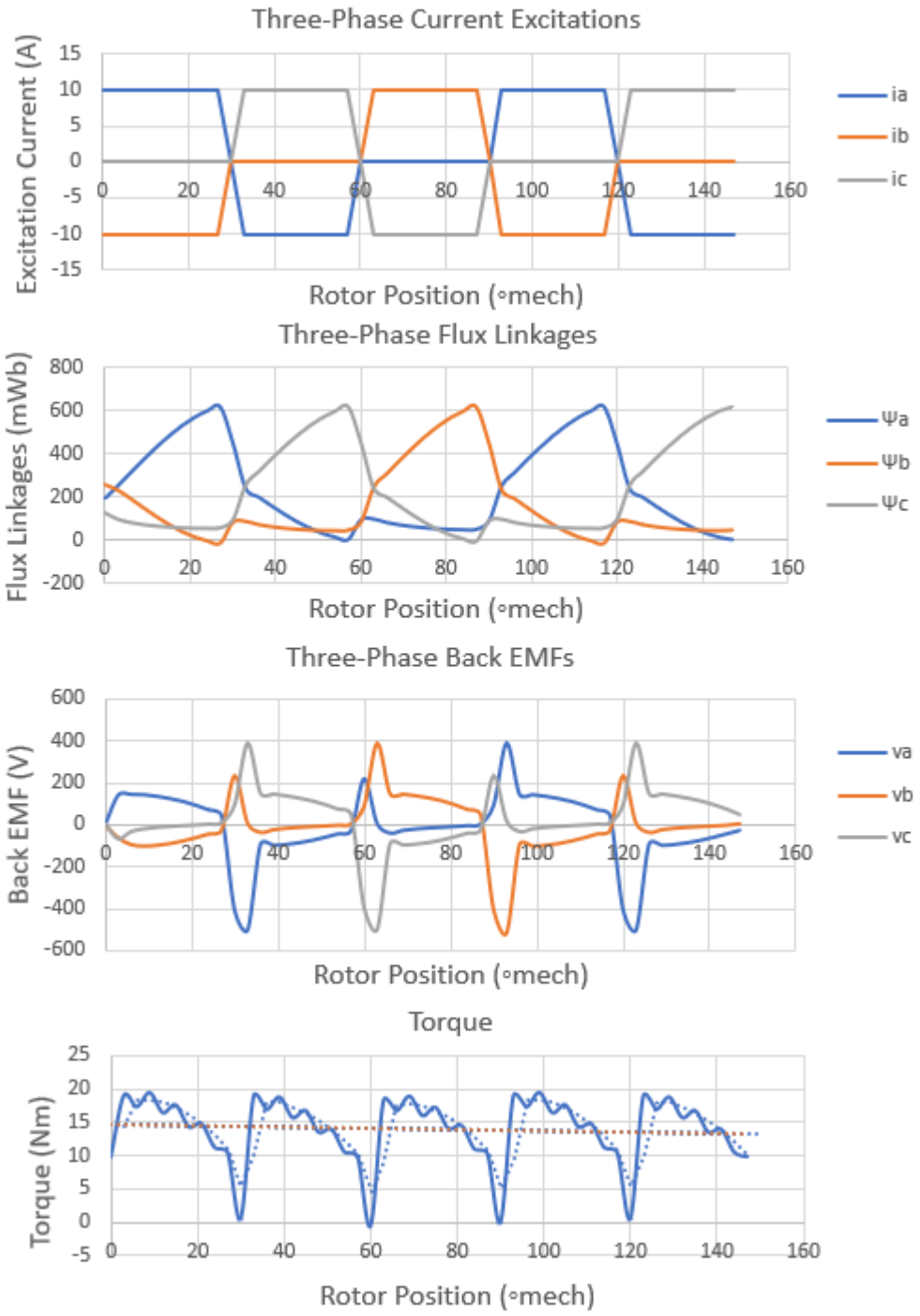

Figure.3.15. Plots of three-phase currents, full load flux linkages with three-phases, back EMF, and torque versus rotor position for the DSPM.

3.5. Doubly Salient Permanent Magnet Machine employing PPMT

Parallel Path Magnetic Technology (PPMT) was introduced by Charles Joe Flynn in [64]. Analysis of a linear actuator and a rotary electric machine employing PPMT has been detailed in this section.

3.5.1. Principle of Operation of Linear Actuator and DSPM Machine employing PPMT

The principle of operation of the novel motor employing PPMT has been discussed with respective electric power and torque equations. The PPMT uses permanent magnets and field coils also called steering coils to form a magnetic circuit. Flux setup by permanent magnets in the magnetic circuit is controlled by steering coils. A basic PPMT actuator as shown in figure.3.16 and figure.3.17 has been considered to explain the PPMT.

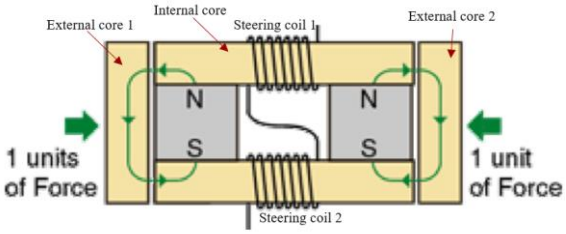

Figure.3.16. Flux path in the magnetic actuator with steering coils off [64].

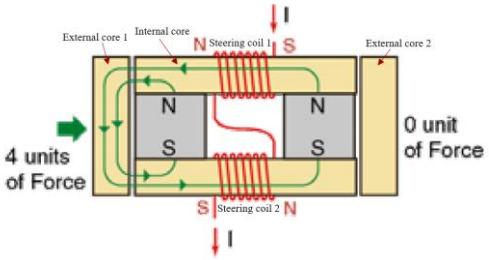

Figure.3.17. Flux path in the magnetic actuator with steering coils energized [64].

Case 1: Steering coils off

Flux setup by permanent magnets finds the paths to external core 1 and external core 2 through the internal core and small air gap as shown in figure.1. Magnetomotive force 'F' experienced by external core 1 or external core 2 is proportional to the flux 'Ø' delivered by a permanent magnet may be expressed as,

$$F \propto \emptyset \propto B_{PM}A \tag{3.1}$$

Thus, magnetomotive force is proportional to the product of flux density of permanent magnet 'B_{PM}' and cross-sectional area of the core 'A'.

Case 2: Steering coils on

Steering coils are excited in a way to steer the effective flux into the external core 1 through airgap and no flux steers into external core 2. Thus, the magnetomotive force experienced by the external core 1 is proportional to the effective flux delivered by two permanents and two steering coils may be expressed as,

$$F \propto \emptyset \propto (2B_{PM} + 2B_{coil})A \tag{3.2}$$

Thus, the maximum flux will be steered into external core 1 when flux setup by steering coil 1 is equal to flux set up by the permanent magnet.

$$B_{PM} = B_{coil} \tag{3.3}$$

Thus,

$$F \propto \emptyset \propto (4B_{PM})A \tag{3.4}$$

Therefore, one unit of flux density in case 1 is reflected as 4 units of flux density in case 2.

3.5.2. Application of Parallel Path Magnetic Technology (PPMT)

Based on PPMT, a single-phase motor topology has been shown in figure.3.18. It consists of 15 poles on the rotor core, 6 coils, and 6 permanent magnets of opposite poles in the stator core. The stator core is similar to the internal core (fig.3.16.), the rotor core is

similar to the external core and the coil is similar to the steering coil used in the previous analysis.

The coils are excited in a way to steer the flux into the rotor to provide unidirectional torque and hence the rotor rotates.

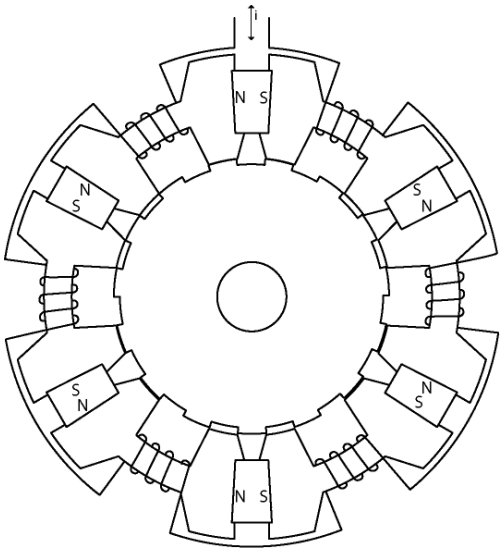

Figure 3.18. Schematic of a 6 coil, 6 permanent magnet, single-phase motor [64].

Case 1: coils are not excited

Permanent magnets set up the flux through three pairs of rotor poles and thus the rotor is locked in position as shown in figure.3.19.

Case 2: coils are turned on

Coils are excited in a way that the effective flux steers through minimum reluctance path setup by three different pair of rotor poles as shown in figure.3.20. Thus, the rotor rotates in the counter-clockwise direction.

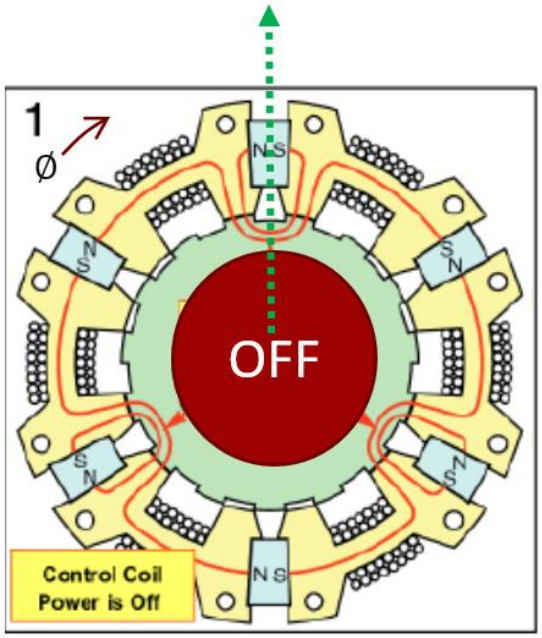

Figure.3.19. Flux path in the single-phase PPMT motor during no excitation current through coils.

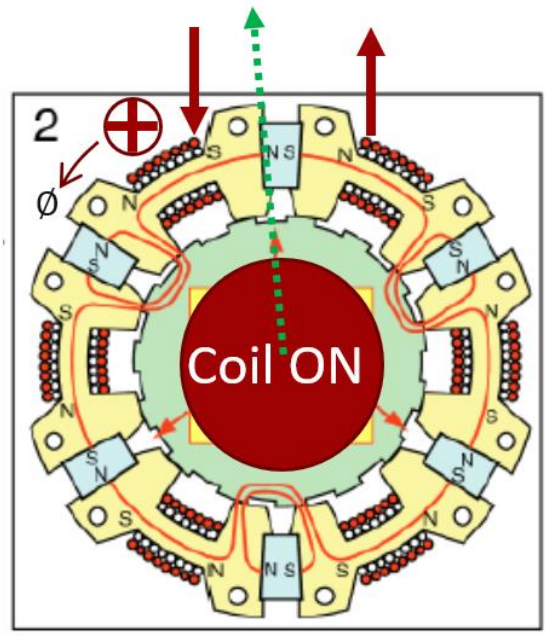

Figure.3.20. Flux path in the single-phase PPMT motor when the coils are excited and forces the rotor to rotate in CCW direction.

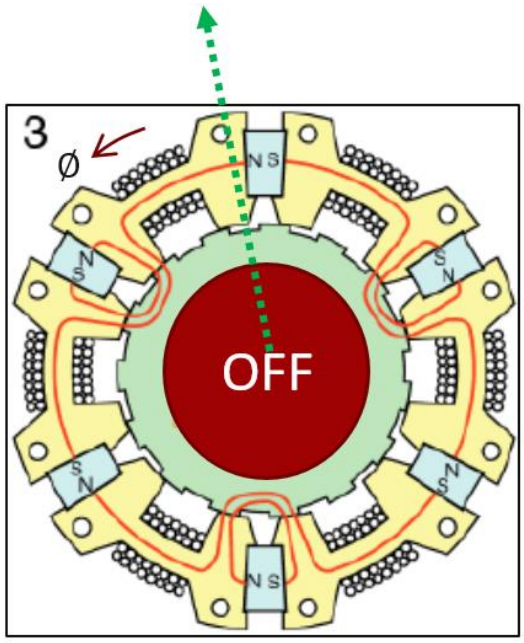

Figure.3.21. Flux path in the single-phase PPMT motor when coils are turned off and rotor poles are slightly aligned.

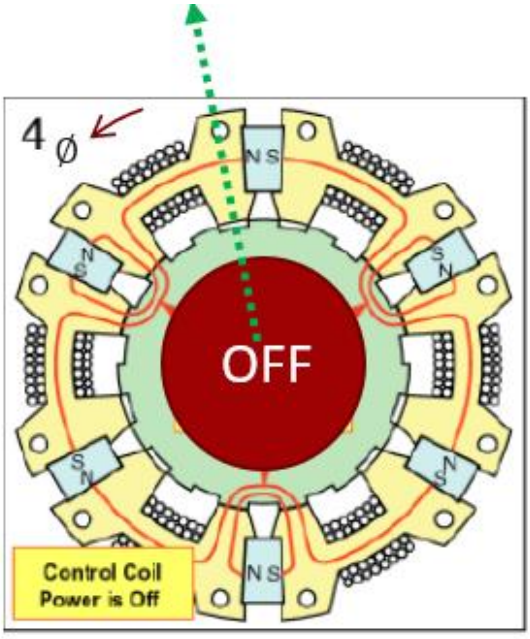

Figure.3.22. Completely aligned position of the rotor with flux path setup in the stator of the single-phase PPMT motor when coils are turned off.

Case 3: coils are turned off

Three different pairs of rotor poles are in a slightly aligned rotor position inherited from the previous state rotate to achieve more alignment with respect to flux path as shown in figure.3.21.

Case 4: coils are turned off

Thus, the rotor continues to rotate till it achieves full alignment with flux path setup by permanent magnets as shown in figure.3.22.

Case 5: coils are excited in opposite polarity

Coils are excited in an opposite polarity such that the flux path aligns with another three different pairs of rotor poles of minimum reluctance path as shown in figure.3.23. Thus, the rotor experiences magnetomotive force and hence continue to rotate in the counter-clockwise direction.

Case 6: coils are turned off

Three different pairs of rotor poles are in a slightly aligned position inherited from the previous state rotates to achieve more alignment with respect to flux path as shown in figure.3.24.

Thus, the rotor continues to rotate till it achieves full alignment with stator flux as shown in the figure.3.19 (case i) and the cycle continues.

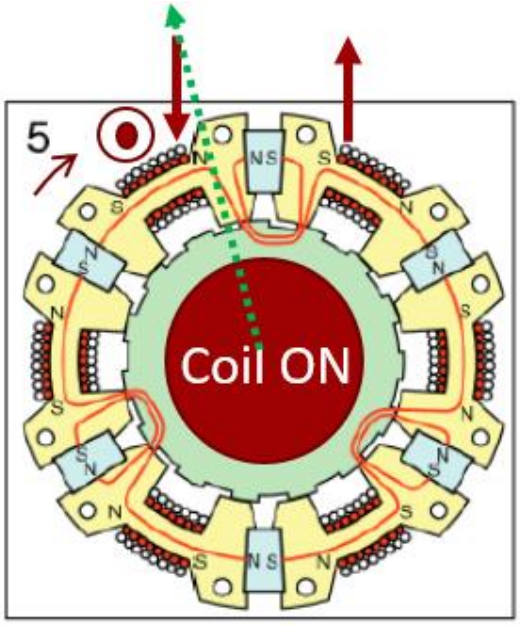

Figure.3.23. Flux path in the single-phase PPMT motor when the coils are excited with a current of opposite polarity and forces the rotor continues to rotate in CCW direction.

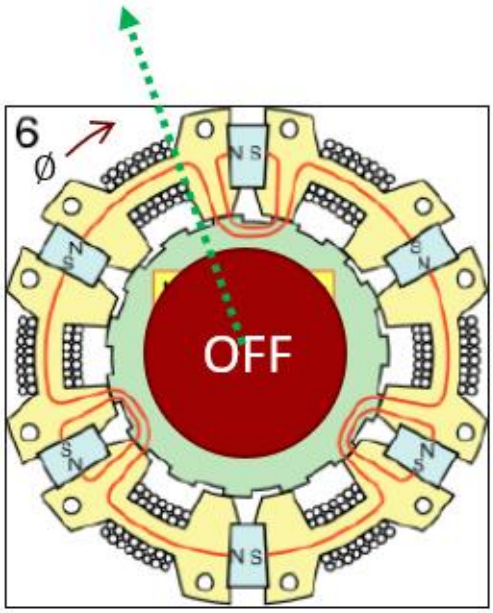

Figure.3.24. Flux path in the single-phase PPMT motor when coils are turned off and rotor poles are slightly aligned.

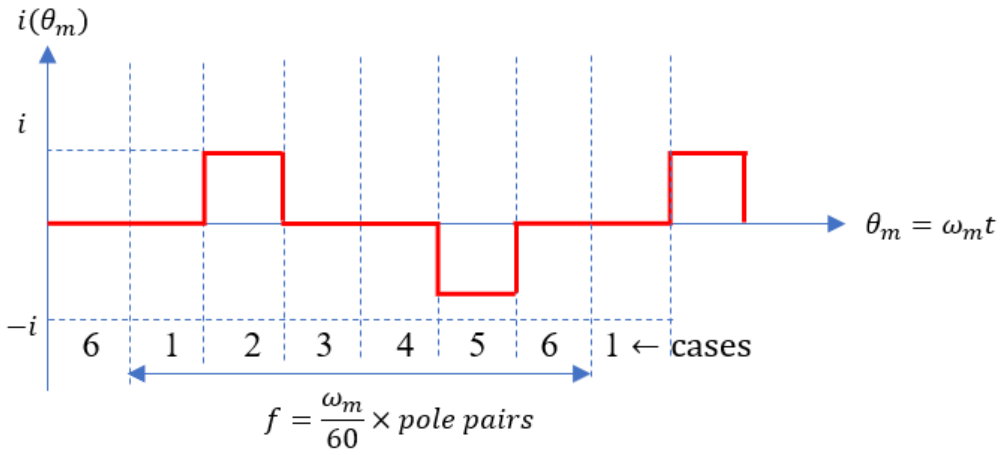

Figure.3.25. Waveform of the current excitation and sequence of events from case 1 to 6.

3.5.2. Analysis of Single-phase PPMT Motor

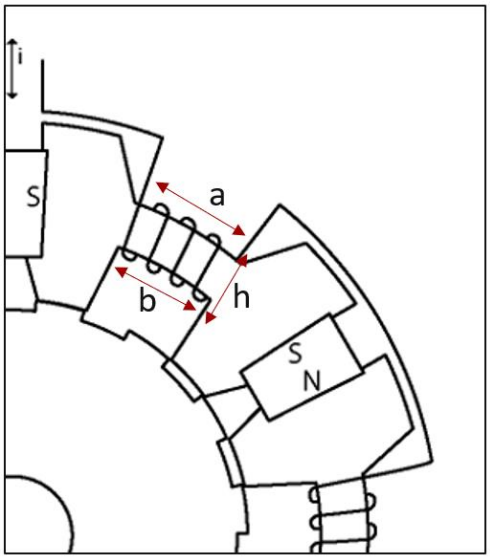

Figure.3.26. Schematic of quarter symmetry of single-phase PPMT motor.

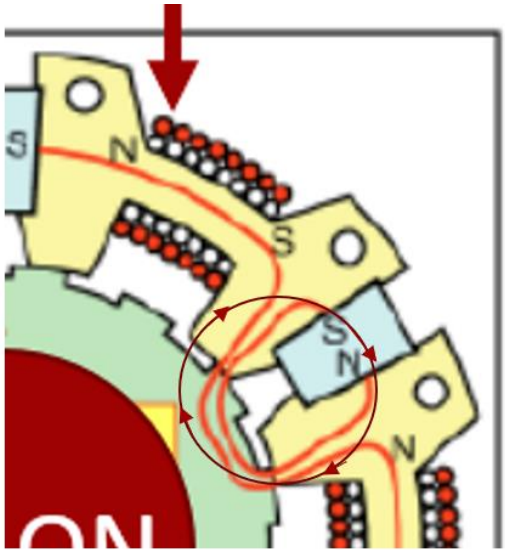

Figure.3.27. Effective flux path in the core of stator, rotor, permanent magnet and airgap of single-phase PPMT motor.

$$area\ of\ axial\ cross\ section\ of\ the\ coil: A_{coil} = l \times h \tag{3.5}$$

$$Flux\ density\ of\ the\ coil: B_{coil} = \frac{\mu ni}{l_{flux}} \tag{3.6}$$

where,

$l = stack\ lentgh\ of\ the\ motor$

$h = radial\ thickness\ of\ the\ coil$

$l_{flux} = length\ of\ flux\ path\ in\ the\ stator\ core\ and\ rotor\ core\ (l_c) + length\ of\ airgap\ (l_g) + width\ of\ permanent\ magnet\ (l_{w-pm})$

$i = current\ through\ the\ coil$

$\mu = permeability\ of\ the\ overall\ flux\ path\ (i.e\ core, air, and\ permanent\ magnet)$

$n = number\ of\ turns\ of\ the\ coil$

$$Flux\ setup\ by\ the\ coil: \emptyset_{coil} = B_{coil} \times A_{coil} = \frac{\mu ni}{l_{flux}} \frac{(a+b)}{2} h \tag{3.7}$$

The topology of the PPMT motor has 6 coils per phase. Thus, flux setup by coils under one phase may be expressed as,

$$\emptyset_{phase} = 6\frac{\mu ni}{l_{flux}} lh = \frac{\mu Ni}{l_{flux}} lh \tag{3.8}$$

where,

$$N = number\ of\ turns\ per\ phase = 6n$$

Similarly, flux set up by a permanent magnet may be expressed as,

$$\emptyset_{pm} = B_r A_{pm} \tag{3.9}$$

where,

B_r

$= residual\ flux\ density\ of\ permanent\ magnet\ (obtained\ from\ charectiristics)$

$A_{pm} = axial\ cross\ sectional\ area\ of\ permanent\ magnet$

$= (radial\ thickness \times axial\ length)$

Flux linkages:

$$\begin{bmatrix} \lambda_a \\ \lambda_{pm} \end{bmatrix} = \begin{bmatrix} L_{aa} & L_{a-pm} \\ L_{pm-a} & L_{pm} \end{bmatrix} \begin{bmatrix} i_a \\ i_{pm} \end{bmatrix} \tag{3.10}$$

where,

$i_{pm} = Fictitious\ current\ due\ to\ perment\ magnet$

$L_{pm} = Fictitious\ inductance\ of\ permanent\ magnet$

A permanent magnet can be modeled as a fictitious winding of one turn. Thus, the magnetomotive force of permanent magnet may be expressed as,

$$1 \times i_{pm} = H_c l_{pm} = B_r A_{pm} R_{pm} \tag{3.11}$$

where,

$H_c = Coercive\ force\ of\ permanent\ magnet$

$R_{pm} = Reluctance\ of\ permanent\ magnet$

Voltage Equation:

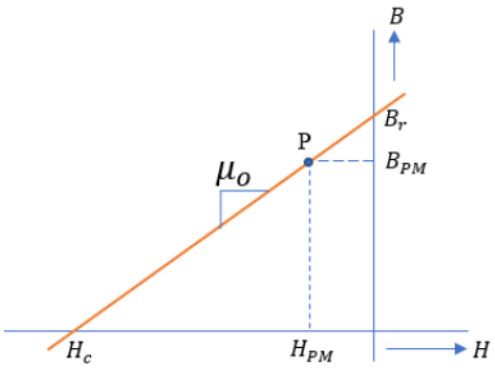

Figure.3.28. Generic characteristic of permanent magnet.

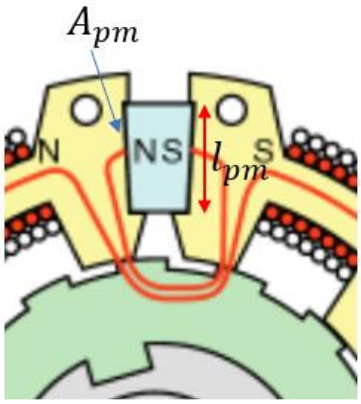

Figure.3.29. Geometry of permanent magnet.

$$v = ri + \frac{\mathrm{d}}{\mathrm{dt}}(\lambda + \lambda_{pm}) \tag{3.12}$$

Power Equation:

A generic simplified form of instantaneous power by neglecting winding resistance may be expressed as [63],

$$p = iL\frac{di}{dt} + i^2\frac{dL}{dt} + i\frac{d\psi_{pm}}{dt} \tag{3.13}$$

Another form of representation of (13),

$$p = \frac{1}{2}i^2\frac{dL}{dt} + Li\frac{di}{dt} + \frac{1}{2}i^2\frac{dL}{dt} + i\frac{d\psi_{pm}}{dt} \tag{3.14}$$

where,

$\psi_{pm} = flux\ linkages\ due\ to\ permanent\ magnet$

By replacing $dt = \frac{d\theta}{\omega_r}$,

$$p = \frac{d}{dt}\left(\frac{1}{2}Li^2\right) + \left[\frac{1}{2}i^2\frac{\partial L}{\partial \theta} + i\frac{\partial \psi_{pm}}{\partial \theta}\right]\omega_r \tag{3.15}$$

$$p = \frac{d}{dt}(W_f) + [T]\omega_r \tag{3.16}$$

where,

$W_f = armature\ reaction\ field\ energy\ per\ phase = \frac{1}{2}Li^2$

$T = Instantaneous\ Torque\ per\ phase = \frac{1}{2}i^2\frac{\partial L}{\partial \theta} + i\frac{\partial \psi_{pm}}{\partial \theta}$

$$T = Reluctance\ Torque + Magnetic\ Torque = T_r + T_m \tag{3.17}$$

$$T_r = \frac{1}{2}i^2\frac{\partial L}{\partial \theta} \tag{3.18}$$

$$T_m = i\frac{\partial \psi_{pm}}{\partial \theta} \tag{3.19}$$

Considering permanent magnet as a fictitious winding with fictitious current and inductance, two-phase instantaneous torque equation may be expressed as [63],

$$T = \frac{1}{2}[i]^T\frac{\partial [L]}{\partial \theta}[i] \tag{3.20}$$

Similarly, two-phase instantaneous armature reaction field energy may be expressed as [63]

$$W_f = \frac{1}{2}[i]^T[L][i] \tag{3.21}$$

where,

$$[i] = \begin{bmatrix} i_a \\ i_{pm} \end{bmatrix} \tag{3.22}$$

$$\begin{bmatrix} \lambda_a \\ \lambda_{pm} \end{bmatrix} = \begin{bmatrix} L_{aa} & L_{a-pm} \\ L_{pm-a} & L_{pm} \end{bmatrix} \begin{bmatrix} i_a \\ i_{pm} \end{bmatrix} \tag{3.23}$$

Thus, substituting (25) and (26) in (22) results in the following expression,

$$T = \left[\frac{1}{2}\left({i_a}^2 \frac{\partial L_{aa}}{\partial \theta}\right)\right] + \left(i_a i_{pm} \frac{\partial L_{a-pm}}{\partial \theta}\right) + \frac{1}{2} {i_{pm}}^2 \frac{\partial L_{pm}}{\partial \theta} \tag{3.24}$$

Thus, the instantaneous torque equation of the PPMT motor consists of three terms. The first terms consist of torque due to variation of self and mutual inductances of the motor phases also called reluctance torque. Interaction of magnetic field due to permanent magnets and current through stator windings results in the second term. The third term is solely due to variation in self-inductance with the respective permanent magnetic field [66]. Various components of instantaneous torque from (3.24) may be expressed as,

$$Reluctance\ Torque = \frac{1}{2}\left({i_a}^2 \frac{\partial L_{aa}}{\partial \theta}\right) \tag{3.25}$$

$$Magnetic\ Torque = i_a i_{pm} \frac{\partial L_{a-pm}}{\partial \theta} \tag{3.26}$$

$$Cogging\ Torque = \frac{1}{2} {i_{pm}}^2 \frac{\partial L_{pm}}{\partial \theta} \tag{3.27}$$

3.5.3. Analysis of Single-Phase PPMT Machine using FEA

A single-phase PPMT machine with two slots to house two coils in the stator, five rotor protrusions, and two PMs separating two stator segments was introduced in [64], as shown in figure 3.30. The stator slots are denoted as S1 and S2 and they are placed spatially 180° apart from each other around the inner circumference of the stator core. The two coils A1 and A2 under each phase are wound toroidally along the axial direction to generate magnetomotive force in counter clock wise direction. The PM1 and PM2 generates magnetomotive forces in counter clock wise and clock wise directions.

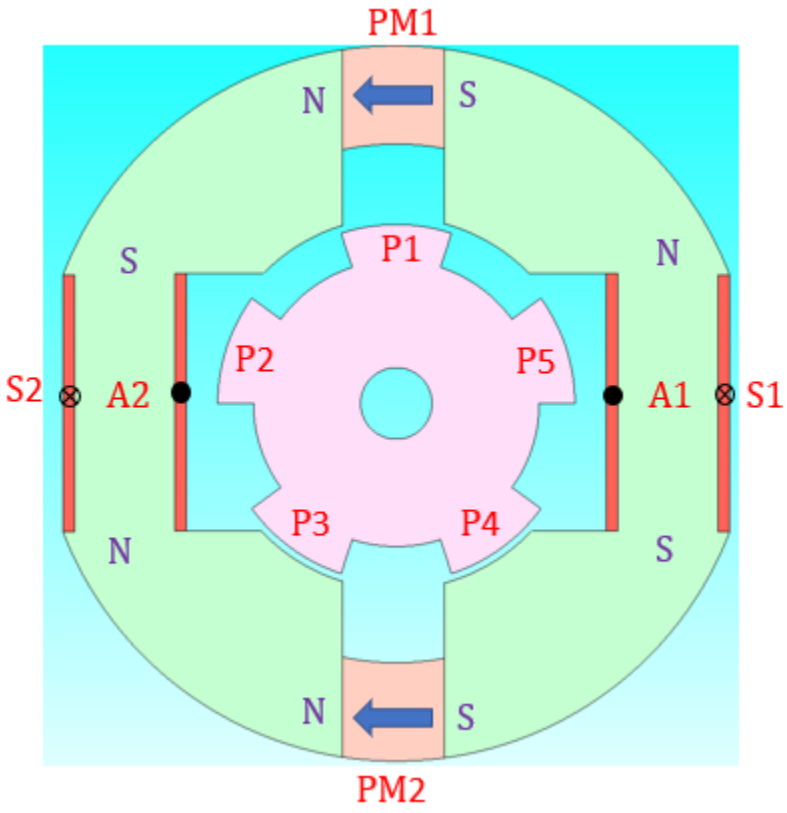

Figure.3.30. 2D FEA schematic of single-phase PPMT machine with 2 slots, 2 PMs and 5 rotor protrusions.

3.5.4. Principle of Operation of Single-Phase PPMT Machine using FEM

The working principle of the single-phase PPMT machine can be understood by observing the flux linkages of the coils with respect to the position of the rotor, as shown in figure 3.31. The coils A1 and A2 under the single-phase experience maximum flux linkages and contribute to the maximum airgap flux density at positions 1 and 3 where poles P3, P4 and P1, P5 aligns with the teeth of the stator core. The coils A1 and A2 under the single-phase experience minimum flux linkages and contribute to the minimum airgap flux density at position 2 where poles are not aligned or partially aligned with teeth of stator core. The properties of flux linkages with coils A1 and A2 via the airgap through the low reluctance path created by salient poles versus the rotor position are shown in figure 3.32. Thus, flux linkages are observed to be bipolar.

Under full load operation, a bipolar or alternating square shape current has been applied to coils A1 and A2 of the phase [64], as shown in figure 3.33. The resultant flux linkages with the coils A1 and A2, the respective back EMF, and torque have been shown in the same figure. A transition in excited currents from positive to negative magnitude reflects a sudden drop in flux linkages, and a spike in the respective back EMFs has been observed. Despite the ripple in the magnitude of the torque, an average positive torque of 4Nm has been observed.

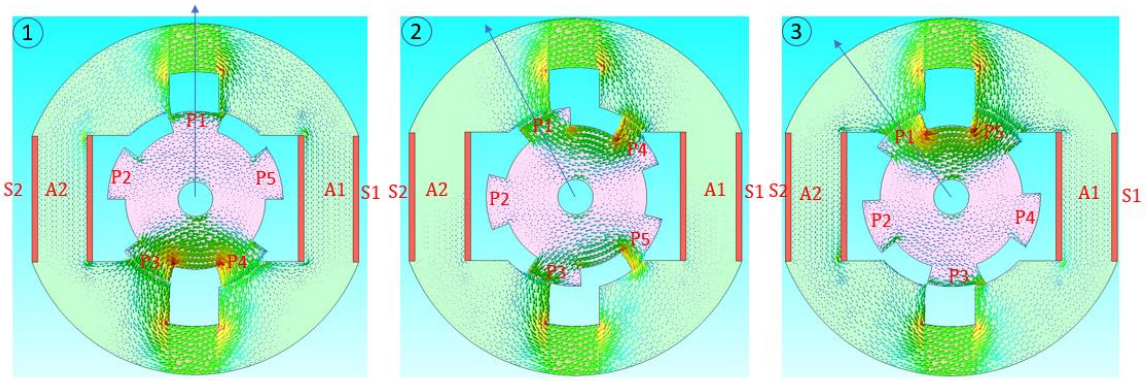

Figure.3.31. Model of single-phase PPMT machine for 2D FEA and properties of flux linkages with coils A1 and A2 of respective phase at different rotor positions.

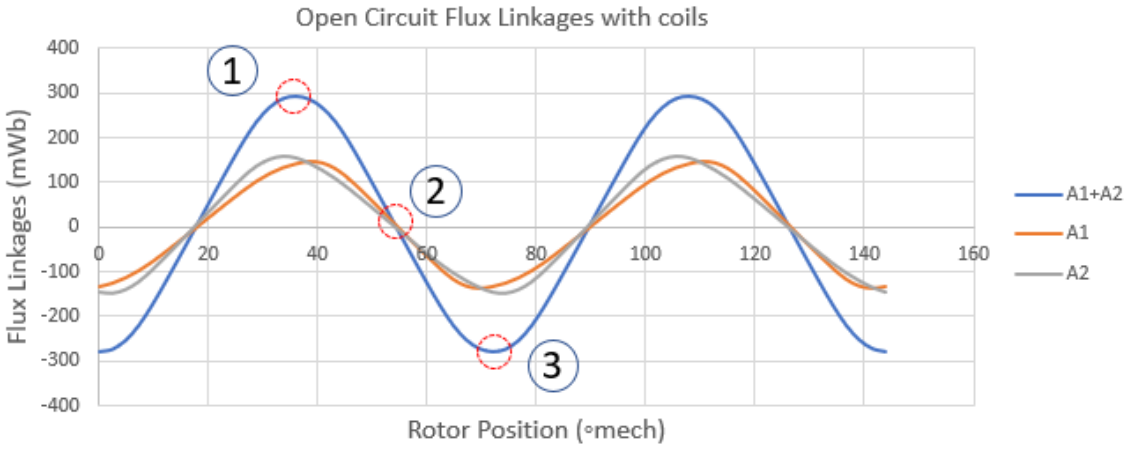

Figure.3.32. Plot of flux linkages with coils A1 and A2 versus rotor position for the single-phase PPMT.

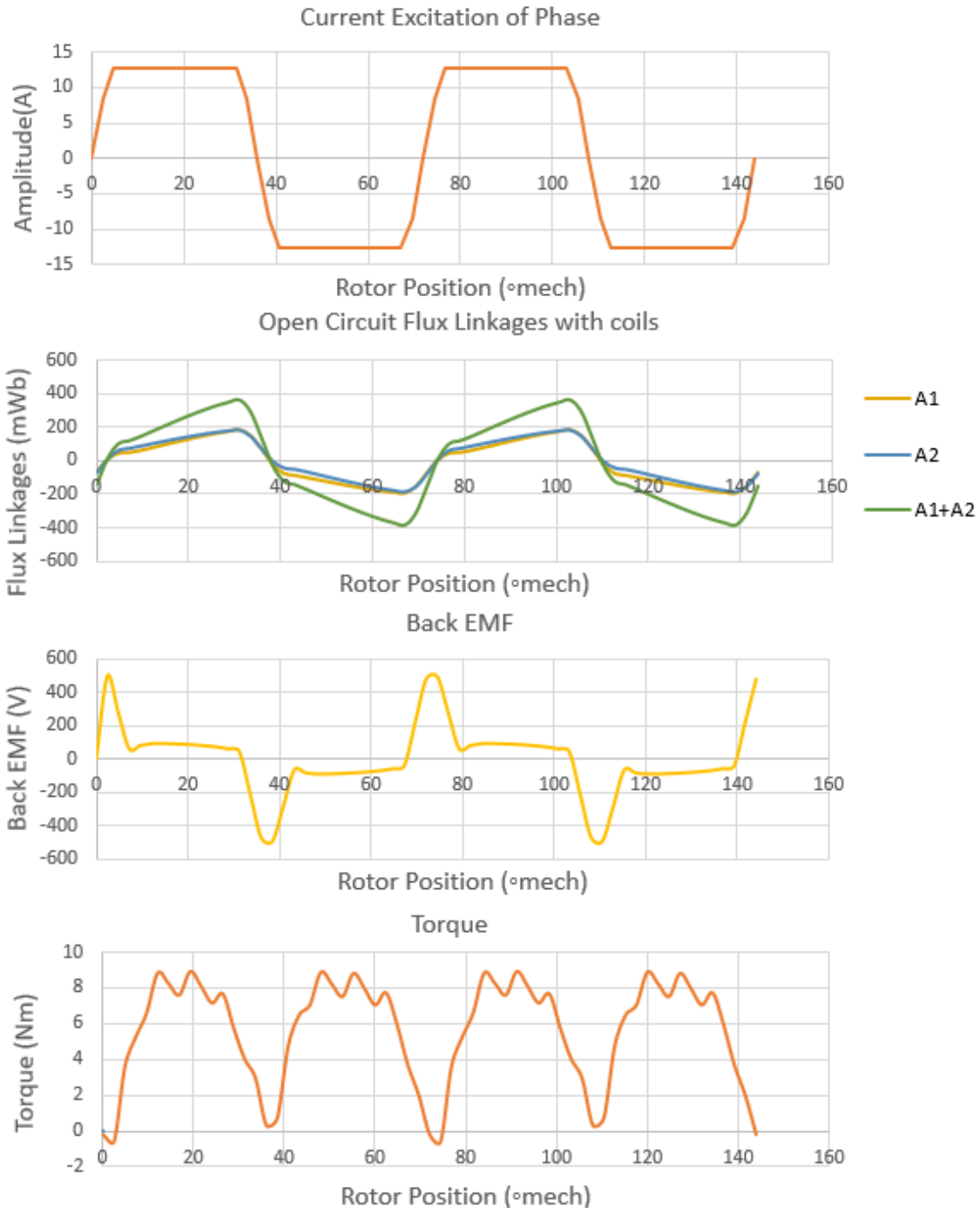

Figure.3.33. Plots of single-phase current, full load flux linkages with coils A1 and A2, back EMF, and torque versus rotor position for the single-phase PPMT motor operation.

3.6. Analysis of a Three-Phase Doubly Salient Permanent Magnet Machine employing PPMT

A special doubly salient permanent magnet machine employing PPMT is introduced in this dissertation, as shown in figure 3.34. The stator of the studied electric machine includes 12 modules of concentrated coils in toroidal shape, which are separated by permanent magnets of opposite polarity inserted in the core, and a rotor with a castellated core structure. This topology is designed to have three phases, 4 coils per phase, 12 PMs, and a 10-pole reluctance type rotor with double saliency. Magnetic field distribution for the proposed machine is shown in the same figure.

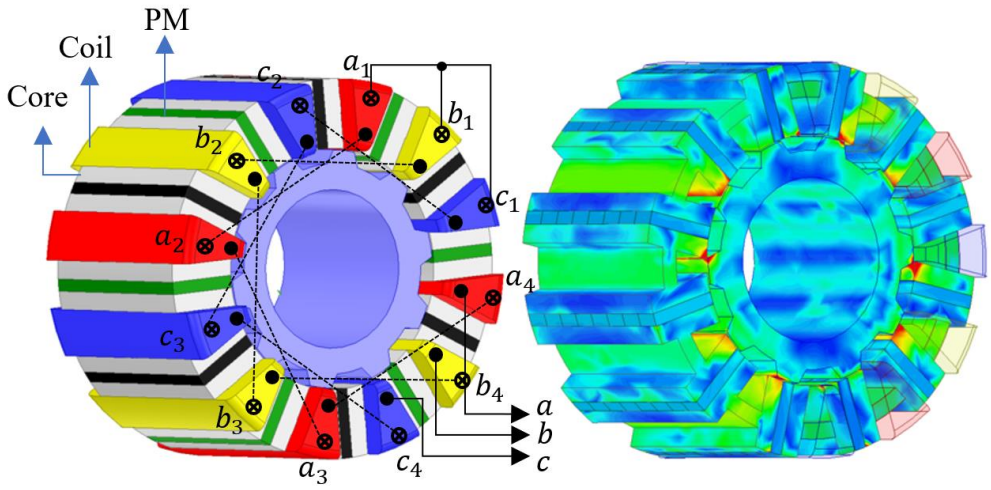

Figure.3.34. Model for 3D FEA and example magnetic field distribution for generator operation of the three-phase special modular machine with 12 concentrated coils and 12 PM in the stator. The reluctance rotor has 10 core protrusions, equivalent to a 20 consequent magnetic pole arrangement.

3.6.1. Principle of Operation of Three-Phase Doubly Salient Permanent Magnet Machine employing PPMT using FEM

The working principle of the proposed special machine can be understood by observing the flux linkages of the coils of the respective phase with respect to the position of the rotor using finite element method, as shown in figure 3.35. A half symmetry of the machine geometry is considered to analyze principle of operation. The coils A1 and A2 under phase-A experience maximum flux linkages and contribute to the maximum airgap flux density at positions 1 and 3 where pole P3 aligns with the teeth of the stator segment S4. The coils A1 and A2 under phase-A experience minimum flux linkages and contribute to the minimum airgap flux density at position 2 where pole P3 aligns with airgap of the stator segment S4 and at and position 4 where pole P3 aligns with teeth of the stator segment S5. The properties of flux linkages with coils under phase-A via the airgap through the low reluctance path created by salient poles versus the rotor position are shown in figure 3.36. Thus, the flux linkages are bipolar and sinusoidal in shape. These results have been verified using lumped parameter magnetic equivalent circuits which will be detailed in Chapter. 4.

Under full load operation, three-phase sinusoidal currents have been applied, as shown in figure 3.37. The resultant flux linkages with respective phases, the respective back EMF, and torque have been shown in the same figure. A transition in excited currents from positive to negative magnitude is smooth because of the sinusoidal shape, reflects as sinusoidal flux linkages and sinusoidal back EMFs. A spike in magnitude of back EMFs has been reported in previous sections for FSM, SRM, DSPM, and single-phase PPMT because of non-sinusoidal excitation. An average electromagnetic torque of 41Nm has been observed from the FEM results.

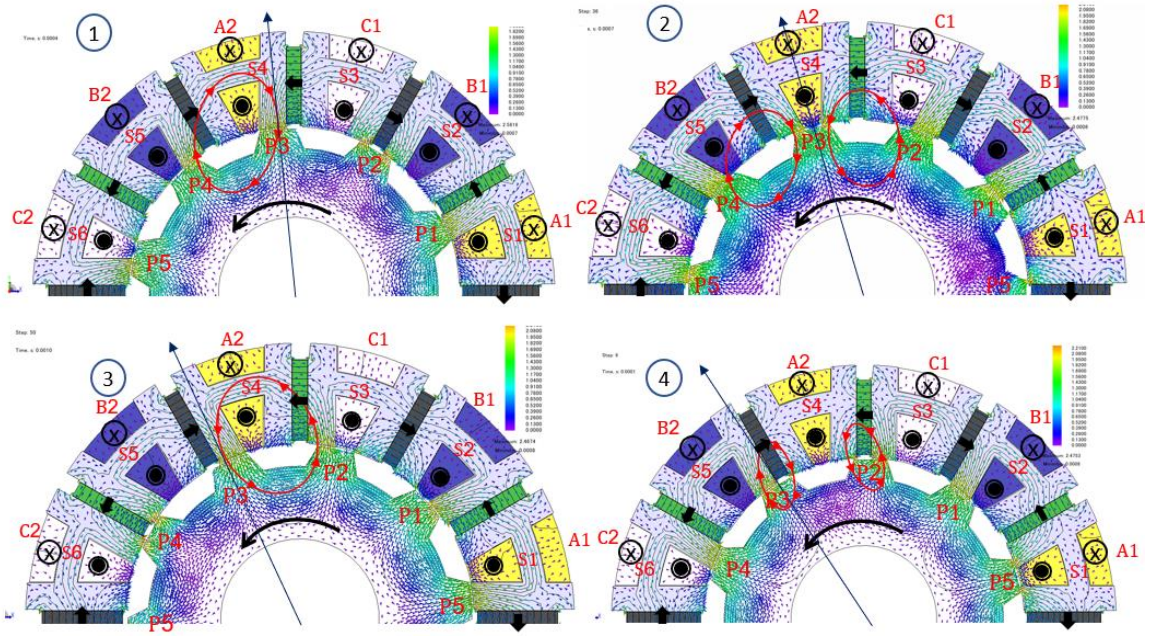

Figure.3.35. Model for 2D FEA and properties of magnetic flux linkages employing FEM with coils of Phase-A from PMs for the proposed DSPM at different rotor positions.

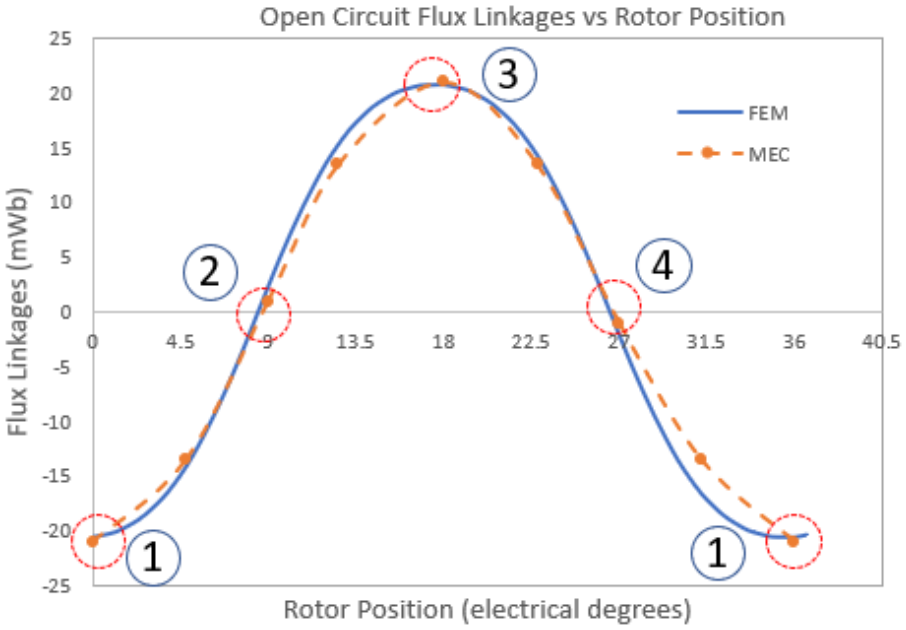

Figure.3.36. Plot of flux linkages with coils under phase-A versus rotor position for the proposed DSPM at different rotor positions using FEM and MEC.

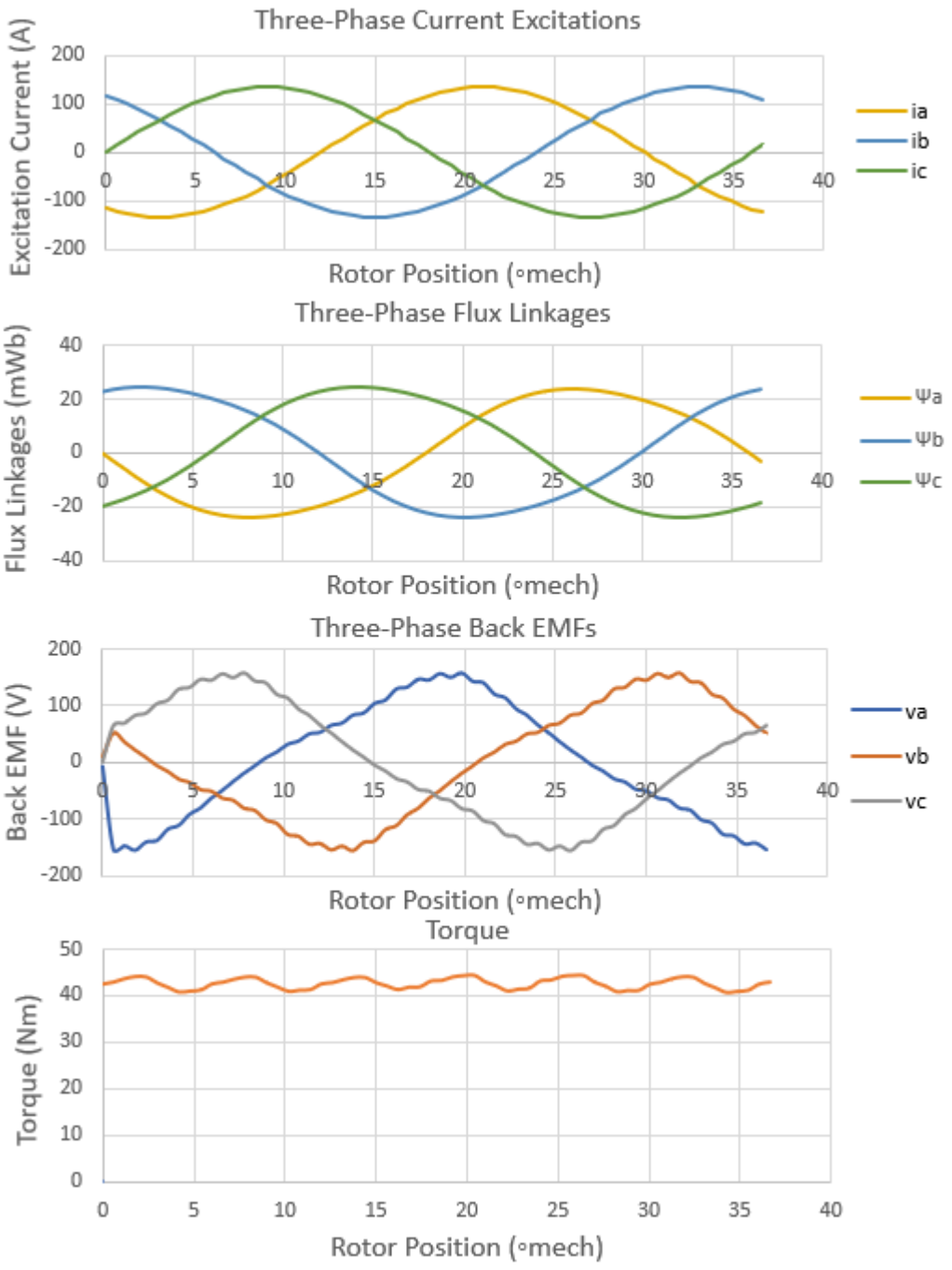

Figure.3.37. Plots of three-phase currents, full load flux linkages with three-phases, back EMF, and torque versus rotor position for the proposed DSPM.

3.6.2. Principle of Operation of Three-Phase Doubly Salient Permanent Magnet Machine employing PPMT using Frequency Domain Analysis

This section presents a study on the winding functions and their respective magnetomotive force (MMF) functions for the proposed doubly salient permanent magnet machine. The MMF functions of the permanent magnets (PMs), stator winding, and airgap permeance functions are analyzed in the frequency domain to identify the spatial harmonics responsible for the torque production mechanism [66]. In machines with a doubly salient structure, the production of torque is proportional to the airgap flux density resulting from the PMs and the windings in the stator [66]. However, it is important to note that while these theoretical MMF functions help identify spatial harmonics that contribute to torque, they may not provide a detailed picture of the magnitudes of the torque [62]. To evaluate the overall performance of the proposed machine, the finite element method and lumped parameter magnetic equivalent circuits have been utilized, and will be further elaborated in Chapter 4.

The proposed machine consists of 12 toroidal coils and 12 PMs, resulting in the creation of multiple poles in the stator. As a result, this machine exhibits MMF functions with multiple harmonics. Frequency domain analysis has been employed to identify the spatial harmonics that are multiples of the fundamental frequency of the airgap permeance function, which corresponds to the 10 pole protrusions.

Magnetomotive Force due to permanent magnets (F_{pm}):

The proposed special machine is equipped with 12 PMs of opposite polarity, which are placed equidistantly between the stator segments. The MMF due to the PMs in the counter-

clockwise direction is considered positive, and vice versa. The top portion of figure 3.38 displays a normalized function of PM MMF, Fpm, for the 12 PMs. Fourier transform is then conducted to identify the harmonic components of the PM MMF, F_{pm} waveform, as shown in the middle portion of figure 3.38. Additionally, the bottom portion of figure 3.38 displays two lower-order spatial harmonics, namely the 6^{th} and 18^{th}, which are superimposed on the PM MMF, F_{pm} waveform.

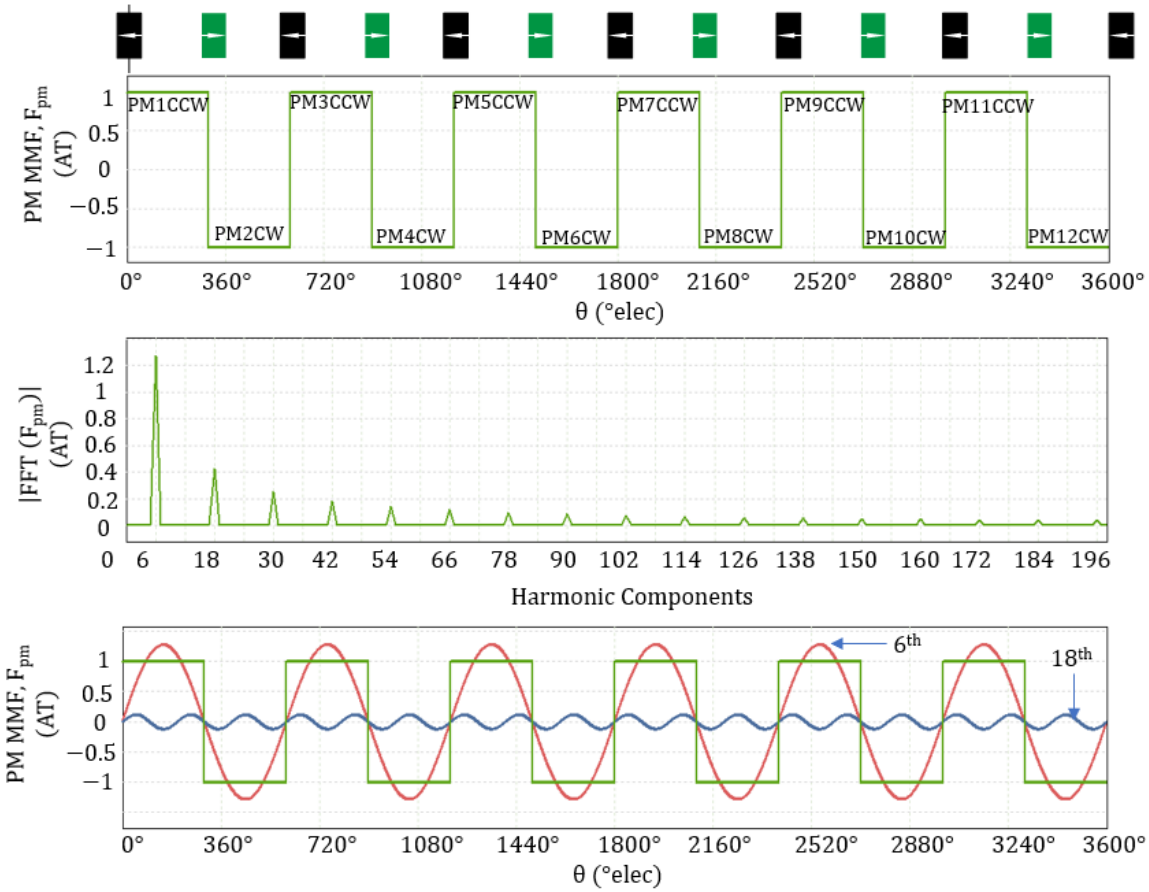

Figure.3.38. Illustration of plots of normalized PM MMFs versus rotor position for the special DSPM with 12 slots, 12 PM, and 10 pole protrusions (top), spatial harmonic content of the PM MMFs (middle), and superimposed two lower order spatial harmonic content of PM MMFs vs rotor position (bottom).

Airgap Permeance Function:

The airgap permeance is a function of space and time as the rotor rotates. The airgap permeance for 10 protrusions and 10 depressions of the salient reluctance type rotor is depicted in the top portion of figure 3.39. The high and low permeances reflect the rotor position at which the airgap is at its minimum and maximum, respectively. The Fourier transformation tool is employed to identify the harmonic components of the airgap permeance function, as shown in the middle portion of figure 3.39. Additionally, the bottom portion of figure 3.39 displays two lower-order spatial harmonics of the airgap permeance function, namely the 10^{th} and 20^{th}.

Airgap Flux Density due to PMs (B_{pm}):

The airgap flux density due to PMs alone, denoted as B_{pm} is a product of the overall PM MMF, F_{pm} in the airgap and the permeance of the airgap. Consequently, an airgap flux density function is obtained, as shown in the top portion of Figure 3.40. By performing Fourier transformation, the harmonic components are identified and shown in the middle portion of figure 3.41 for the first 200 components. Additionally, the bottom portion of figure 3.42 presents two lower-order spatial harmonics, namely the 4^{th} and 6^{th}, which are superimposed on the airgap flux density function.

Turns Functions:

One of the distinctive features of the proposed DSPM machine is the presence of toroidal coils wound axially on the H-shaped stator segment, which generates MMF in a counter-clockwise direction. Although the coil winding appears similar to a concentrated winding, the turns are spatially distributed over 20 degrees. Therefore, in terms of turns, it

resembles a fractional wave winding pattern that is spread out over 20 degrees. Figure 3.43 depicts a 2D FEA schematic of the stator segment and the pattern of the turns.

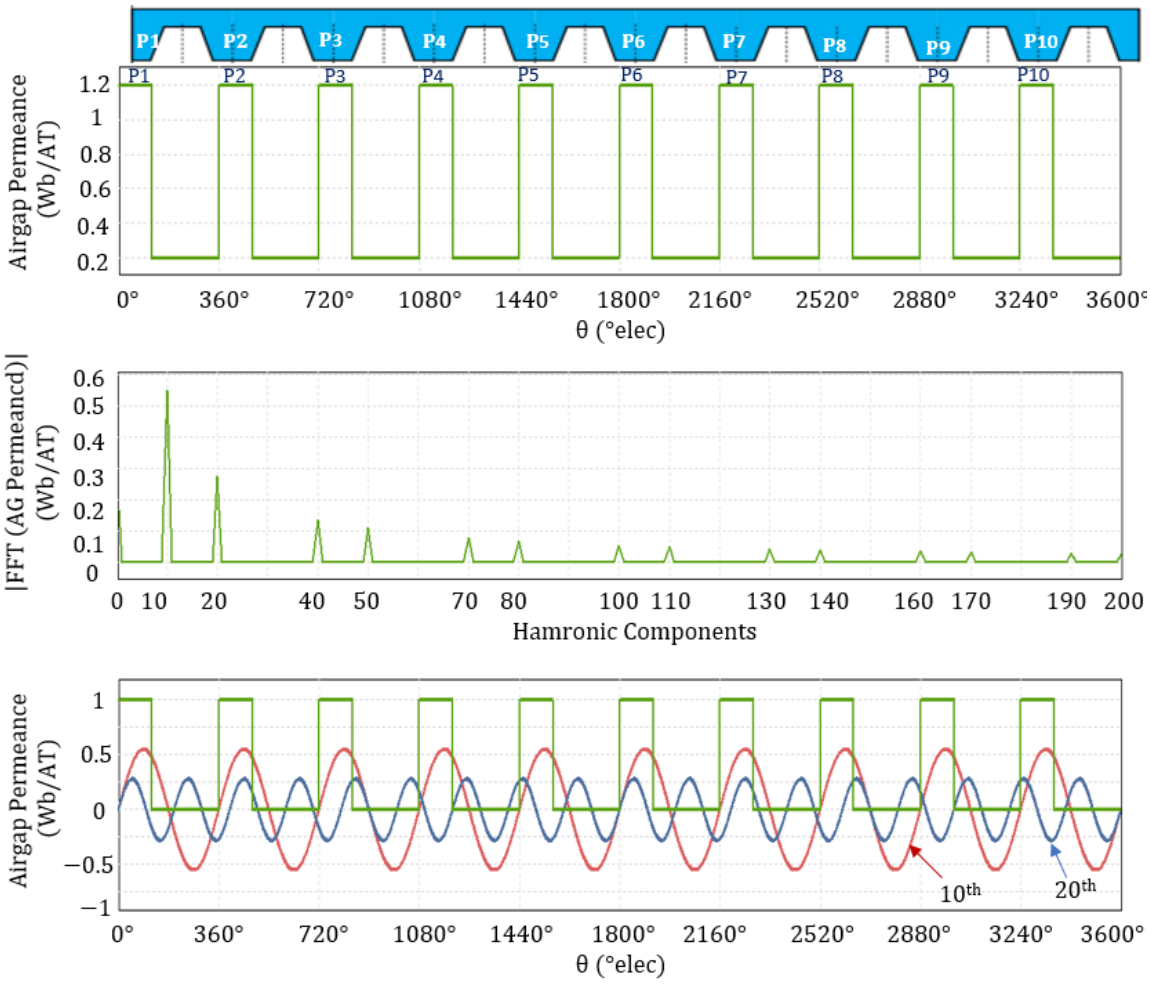

Figure.3.39. Illustration of plots of normalized airgap permeance function versus rotor position for the special DSPM with 12 slots, 12 PM, and 10 pole protrusions (top), spatial harmonic content of the airgap permeance function (middle), and superimposed two lower order spatial harmonic content of airgap permeance function vs rotor position (bottom).

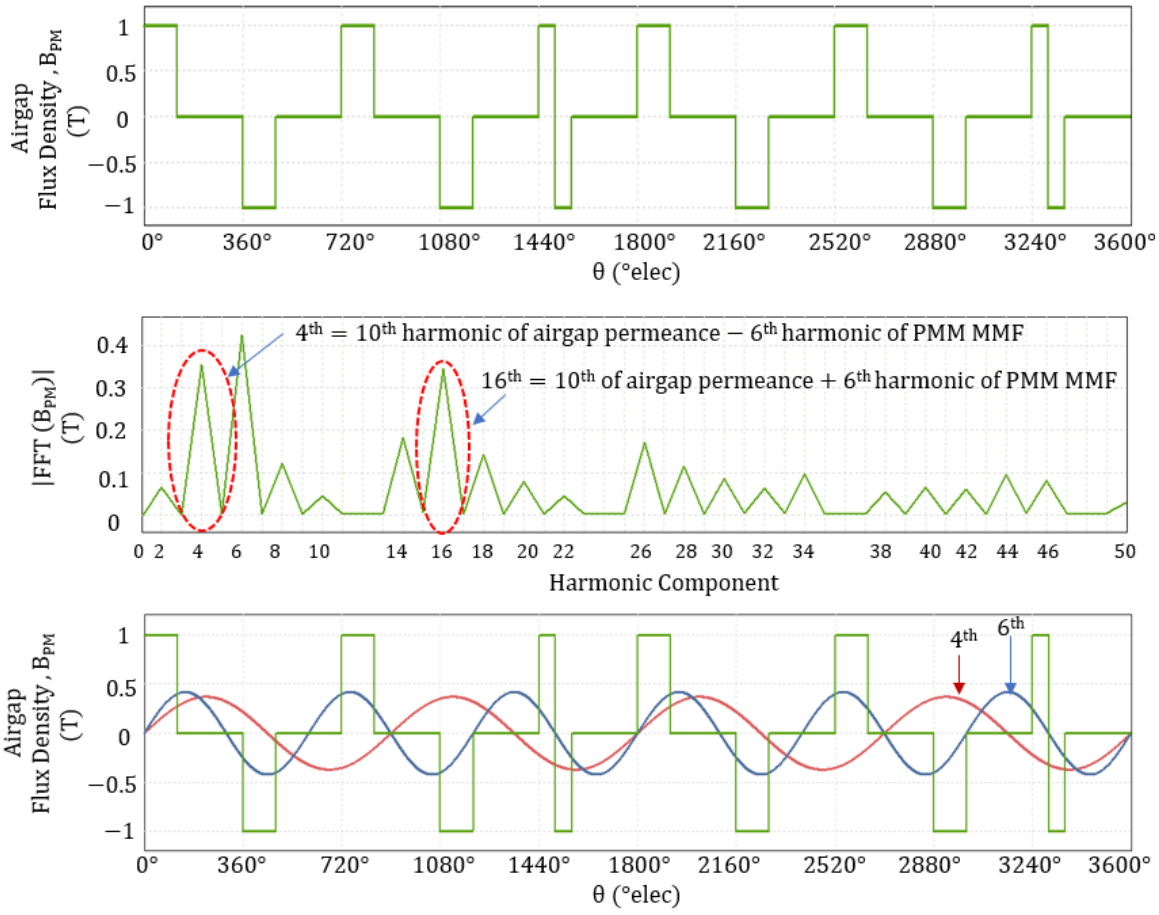

Figure.3.40. Illustration of plots of normalized airgap flux density function B_{pm} versus rotor position for the special DSPM with 12 slots, 12 PM, and 10 pole protrusions (top), spatial harmonic content of the airgap flux density function B_{pm} (middle), and superimposed two lower order spatial harmonic content of airgap flux density function B_{pm} vs rotor position (bottom).

Figure.3.44 illustrates the turns function for the toroidal coil. The turns function is determined by considering the orientation of the turns in the top and bottom portions. The turns function is deemed positive for the conductor that carries current inwards (into the page), which is situated in the top portion of the stator segment, and approaches zero for the conductor that carries current outwards (out of the page), located in the bottom portion of the stator segment. As a result, the coil with seven turns has seven positive and zero pulses throughout the spatial span of 20 degrees.

The turns function of a coil with spatially distributed turns contains a large number of high spatial frequency harmonics due to its pulsating shape with a high frequency. To facilitate harmonic analysis, an approximate lumped model of the toroidal coil is presented in figure.3.45. The turns function is simplified by considering the lumped conductor in the top and bottom portions as a single positive pulse spread spatially over 20°, as shown in figure.3.46. This approach is extended to the turns for each phase, where four coils are connected in series, as shown in figure.3.47.

Winding Functions:

The turns functions were adjusted to realize winding functions for each phase according to the definition of generalized winding function in [67], may be expressed as (3.28). This adjustment ensured that each winding function had an even symmetry and zero average, as shown in figure.3.46. Once the winding functions were obtained, they were used to calculate the airgap MMF, F_w by considering the instantaneous three-phase currents.

$$N(\emptyset) = n(\emptyset) - < n(\emptyset) > \tag{3.28}$$

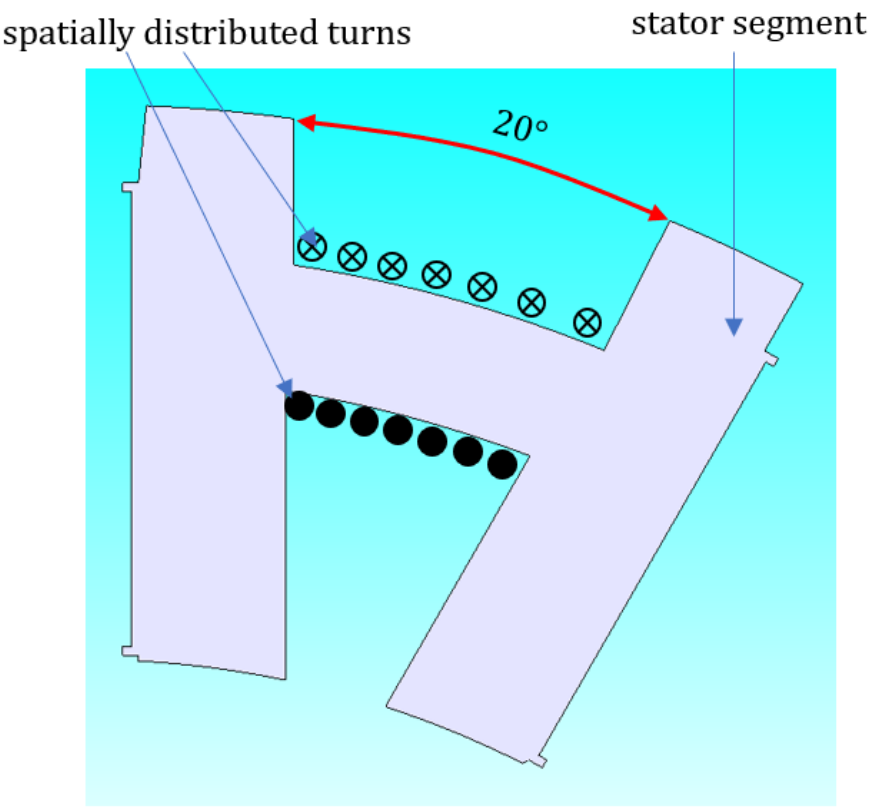

Figure.3.43. 2D model of a toroidal coil with stator segment, showing pattern of spatially distributed turns for a span of 20°.

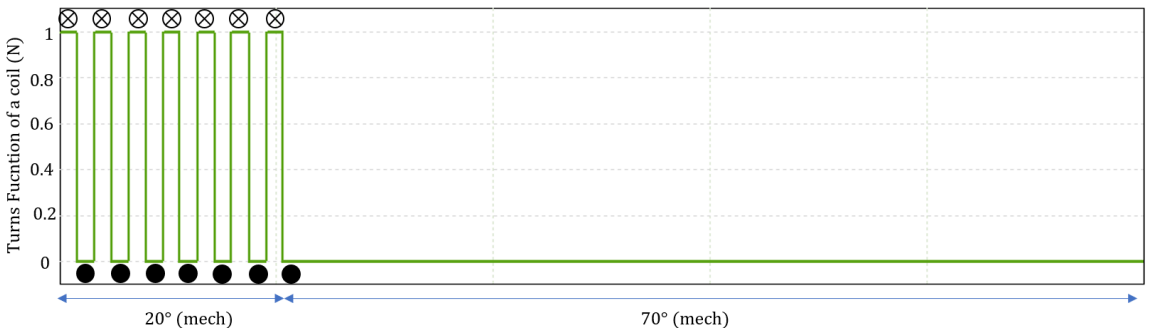

Figure.3.44. Illustration of turns function for a toroidal coil with spatially distributed turns for a span of 20°.

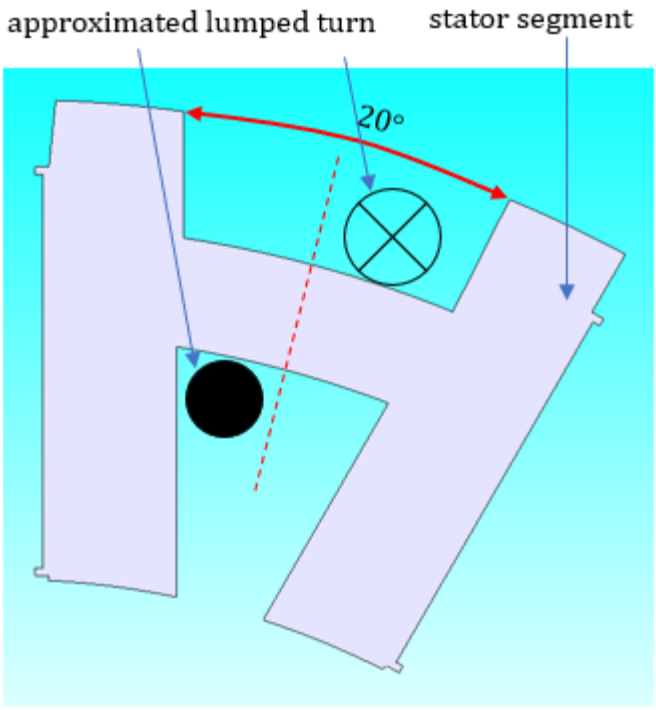

Figure.3.45. 2D model of a toroidal coil with stator segment, showing pattern of lumped model of a turn for a span of 20°.

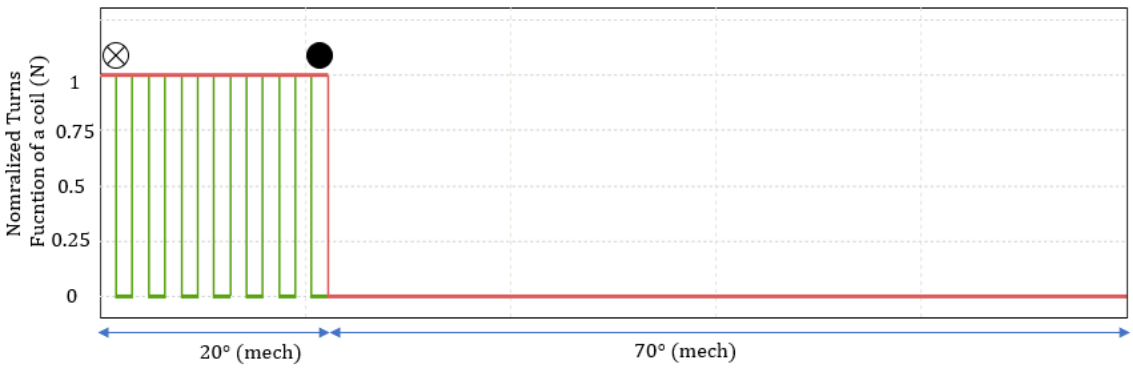

Figure.3.44. Illustration of turns function for a toroidal coil with lumped model of a lumped model of a turn for a span of 20°.

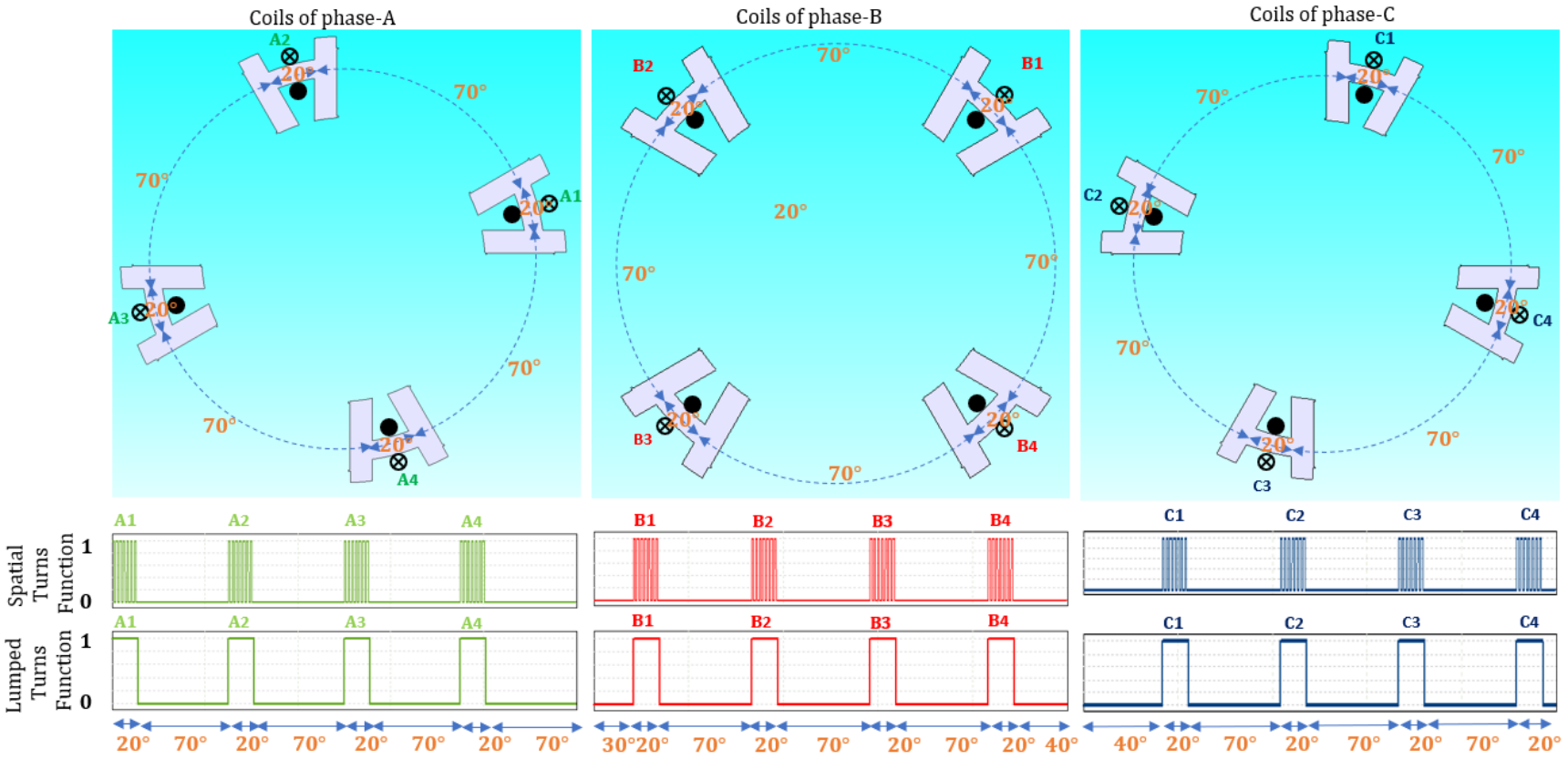

Figure.3.45. 2D FEA schematic of stator segments with toroidal coils, illustration of spatially distributed turns functions, and approximated lumped turns functions for coils under each phase.

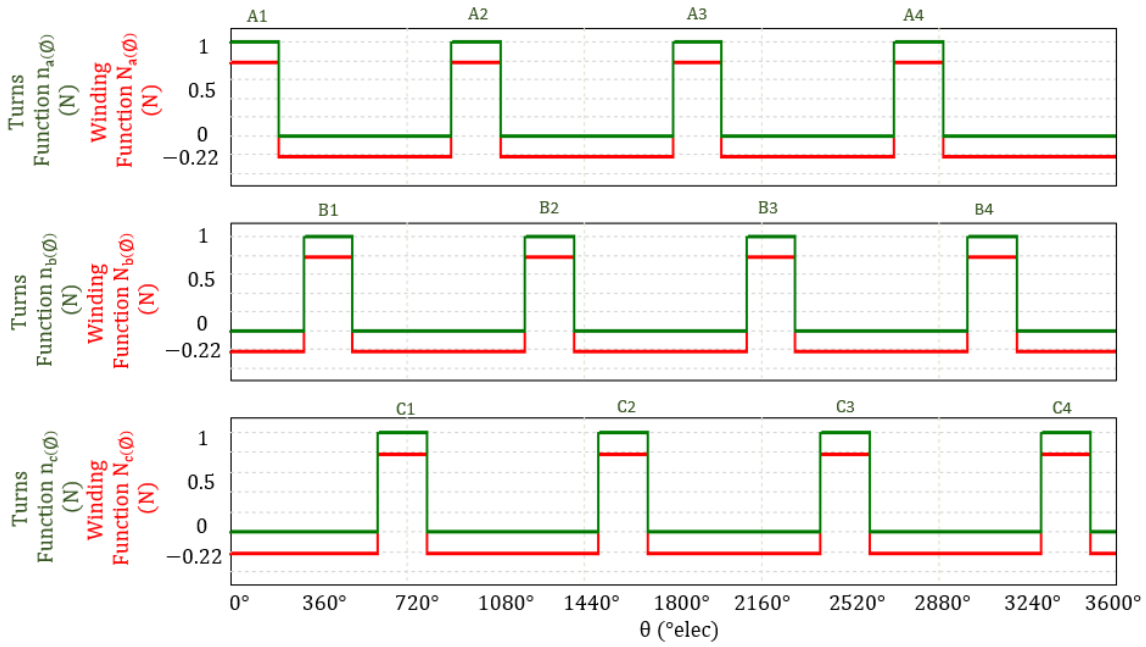

Figure.3.46. Illustration of plots of turns functions and winding functions versus rotor position for each phase for a span of 360° (mech).

Airgap MMF due to Stator Winding (F_w):

The airgap MMF due to the stator winding, denoted as F_w, is the product of the winding functions and instantaneous currents of the respective phases. The three-phase airgap MMF is defined as sum of the individual airgap MMFs from each phase,

$$\text{Airgap MMF}, F_w = F_a + F_b + F_c = N_a(\emptyset)i_a + N_b(\emptyset)i_b + N_c(\emptyset)i_c \qquad (3.29)$$

Figure.3.47 shows the instantaneous winding functions and currents of respective phases, as well as the resulting three-phase airgap MMF. To identify the harmonic components in the three-phase airgap MMF, F_w, a Fourier transform is performed. The analysis reveals lower order spatial harmonics of 6th and 18th. These harmonics are then superimposed on the three-phase airgap MMF, F_w, as shown in figure.3.48.

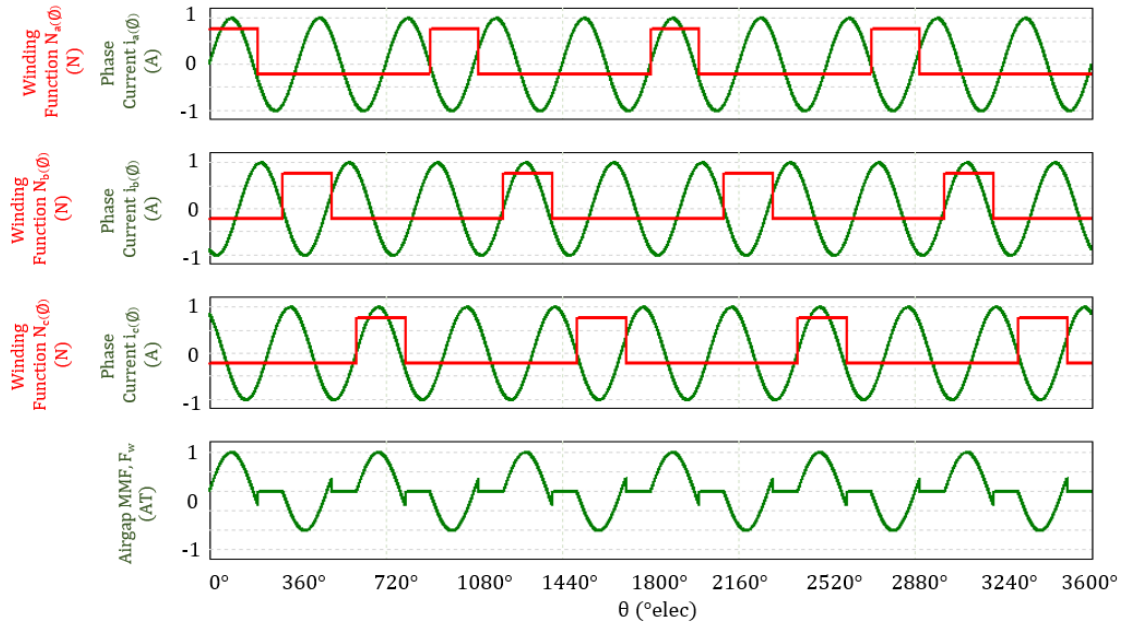

Figure.3.47. Illustration of plots of winding functions, instantaneous currents, and airgap MMF, F_w versus rotor position for a span of 3600° (elec).

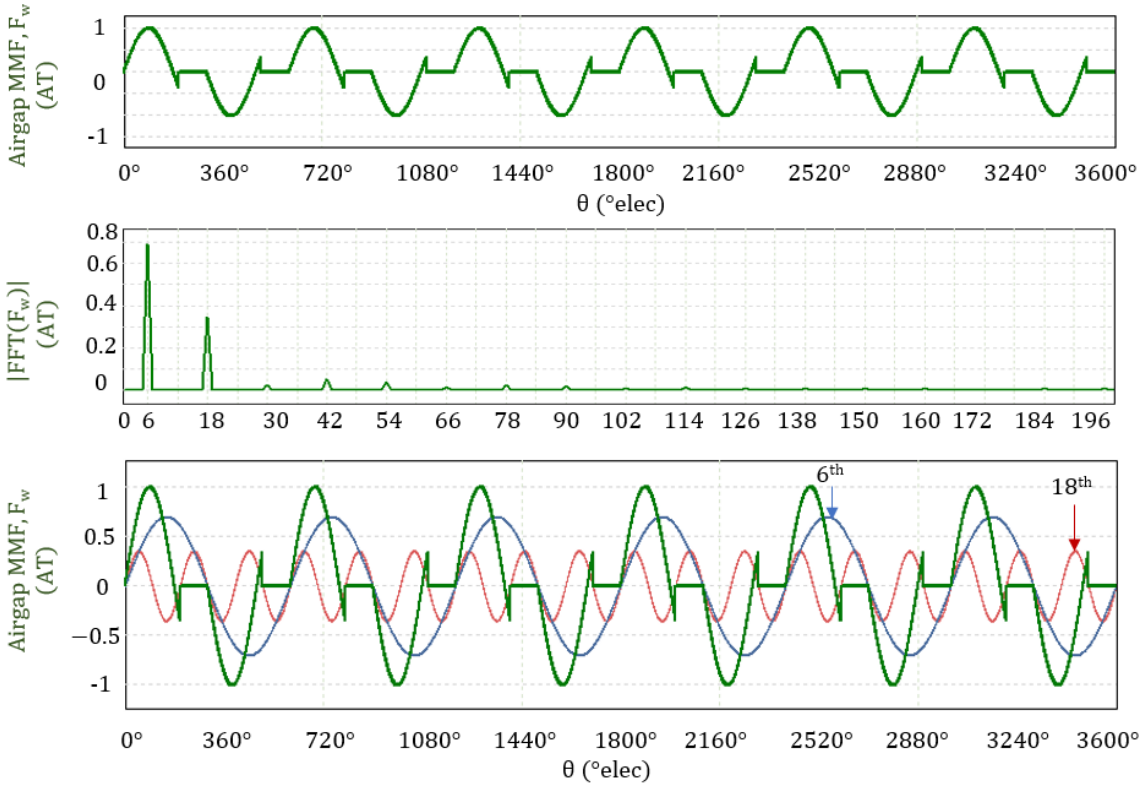

Figure.3.48. Illustration of plots of normalized airgap MMF, F_w versus rotor position for the special DSPM with 12 slots, 12 PM, and 10 pole protrusions (top), spatial harmonic content of the airgap MMF: F_w (middle), and superimposed two lower order spatial harmonics content of airgap MMF, F_w vs rotor position (bottom).

Airgap Flux Density due to Stator Winding:

The airgap flux density due to the stator winding, B_w, is obtained by multiplying the three-phase airgap MMF, F_w, with the airgap permeance. The plot of airgap flux density, Bw, versus rotor position is shown in figure 3.49. Fourier transform is performed on B_w waveform to identify the first fifty harmonic components, which are shown in the third plot from the top in the figure 3.49. Two lower-order spatial harmonics are superimposed on the airgap flux density Bw, as shown in the bottom plot of the figure 3.49.

Spatial Harmonics in Airgap MMFs and Airgap Permeance:

The primary spatial harmonic component of the PM MMFs, F_{pm} and winding MMF, F_w waveforms is the sixth harmonic for the 12-PM, 12-slot, and 10-pole DSPM, as shown in the figures 3.38 and 3.48. The order of this primary spatial harmonic in the respective MMFs is equal to half of the number of permanent magnets and half of the number of slots that are circumferentially magnetized or electromagnetized. The primary spatial harmonic component of the airgap permeance waveform for the proposed DSPM is equal to the number of protrusions on the salient rotor, which is 10, as shown in the figure.3.39."

Spatial Harmonics in Airgap Flux Densities:

Spatial harmonics of the 4^{th} and 16^{th} orders are observed in the airgap flux densities B_w and B_{pm} waveforms for the 12-PM, 12-slot, and 10-pole DSPM, as shown in the figure.3.49 and figure.3.40. These harmonic components result from the frequency modulation of the winding airgap MMF function, F_w with 12 slots or the magnet airgap MMF function, F_{pm} with 12 PMs and the airgap permeance function with 10 rotor pole protrusions.

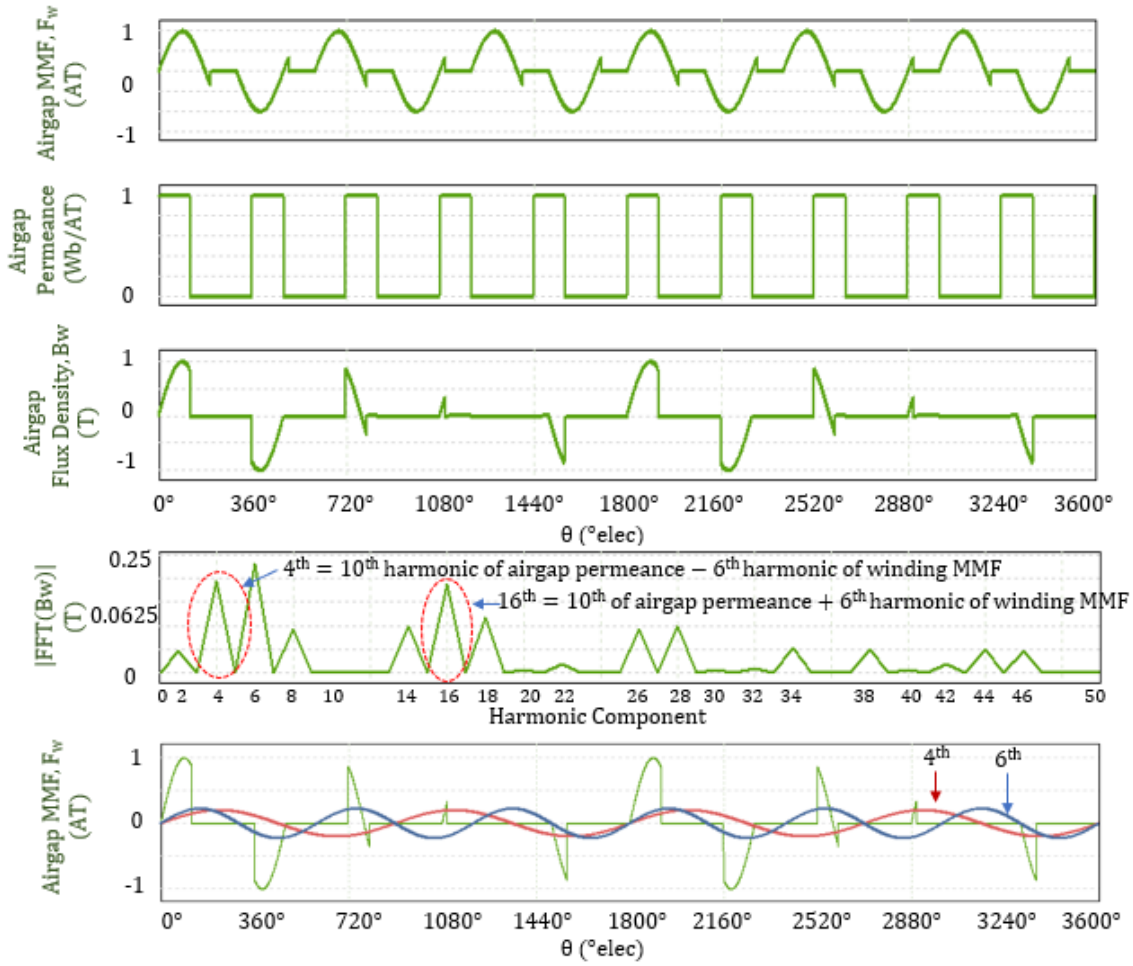

Figure.3.49. Illustration of plots of normalized airgap MMF, F_w versus rotor position for the special DSPM with 12 slots, 12 PM, and 10 pole protrusions (top), airgap permeance versus rotor position (2nd from the top), airgap flux density due to winding: B_w versus rotor position (3rd from the top), and superimposed two lower order spatial harmonic content of airgap flux density, B_w vs rotor position (bottom).

The 4th spatial harmonic component in the airgap flux densities, B_w and B_{pm} waveforms is due to the difference between the 10th harmonic in the airgap permeance waveform and

the 6^{th} harmonic in the respective MMFs, F_w and F_{pm} waveforms. Similarly, the 16^{th} spatial harmonic in the airgap flux densities B_w and B_{pm} is due to the addition of the 10^{th} harmonic in the airgap permeance waveform and the 6^{th} harmonic in the respective MMFs, F_w and F_{pm} waveforms.

Thus, 4^{th} and 16^{th} spatial harmonics of winding airgap flux density B_w and magnet airgap flux density B_{pm} are in synchronous, rotate at the same temporal frequency in the same direction. Interaction of 4^{th} and 16^{th} harmonics of winding airgap flux density B_w and magnet airgap flux density B_{pm}, produce a non-zero average torque. The average of these two spatial harmonics of order 4^{th} and 16^{th} is synchronous with primary spatial harmonic component of the airgap permeance waveform.

Thus, the 4^{th} and 16^{th} spatial harmonics in the winding airgap flux density, B_w and magnet airgap flux density, B_{pm} are synchronous and rotate at the same temporal frequency in the same direction. The interaction of these two harmonics produces a non-zero average torque. The average of these two spatial harmonics of order 4^{th} and 16^{th} is synchronous with the primary spatial harmonic component of the airgap permeance waveform.

More insight into the electromagnetic performance of the proposed DSPM is detailed in Chapter 4 of this dissertation.

CHAPTER 4: ANALYSIS OF THE MECHANICALLY DOUBLY SALIENT ELECTRIC MACHINE USING FE AND LUMPED PARAMETER MAGNETIC EQUIVALENT CIRCUIT MODELS

4.1. Introduction

Analysis of the proposed special machine topology, which features a doubly salient structure and permanent magnets in the stator and provides very high power density performance has been presented in this chapter. An analytical model for the proposed machine has been developed using lumped parameter magnetic equivalent circuits (LPMEC) of the stator segments, permanent magnets (PM), toroidal windings, air gap, and reluctance-type rotor. Previously published analytical techniques have not thoroughly explored spatial harmonics, which is done in the proposed methodology, yielding a high-fidelity model. The machine analyzed is highly suited for electric vehicle traction applications and consists of 12 stator segments and coils, separated by 12 PMs in the stator, and a reluctance-type rotor with 10 protrusions. The LPMEC model has been analyzed to compute flux linkages, open circuit back EMF, and inductances with respect to the rotor position, and these results have been verified using finite element method. The analysis shows that despite its doubly salient structure, the proposed machine exhibits the characteristics of a non-salient machine, and this behavior has been validated by analyzing spatial harmonics and static torque test.

Electromagnetic fields of an electric machine can be determined analytically using various methods such as magnetic equivalent circuits (MEC) [67], Carter factor relative permeance model [68], complex relative permeance model [69], and conformal mapping

[70]. Application of MEC to determine magnetic fields of induction machine, switched reluctance machine, internal permanent magnet machine, and flux switching machines were reported in [71]-[74].

The LPMEC methodology presented in [69] and [74] for FSPM has been employed to analyze performance of the proposed DSPM considering PMs in stator. The proposed DSPM consists of 12 coils and 12 PMs in the stator, and a reluctance-type rotor with 10 protrusions, which is equivalent to 20 electrical poles. This three-phase machine has rated torque and speed ratings of 41 Nm and 5000 rpm respectively. A 2D FEA schematic of the proposed machine, example of magnetic field distribution, and an open frame laboratory prototype (OFLP) were shown in Figure 4.1, Figure 4.2, and Figure 4.3.

4.2. Analysis of Magnetic Equivalent Circuits

Design matrices listed in TABLE 4.1 have been used to solve the magnetic equivalent circuits. Nomenclature listed in TABLE 4.2 has been used throughout the chapter. Stator tooth reluctance R_{sxtx}, stator tooth leakage reluctance R_{msxtx}, circular core reluctance R_{six}, and PM reluctances R_{pm} have been expressed as (4.1) to (4.4). MMF due to PM F_{pm} and concentrated coil F_w are expressed as (4.5) and (4.6). Reluctances of airgap has been realized by employing flux tubes shown in Figure 4.7.

The LPMECs for the DSPM have been realized by considering the MMF of coils and PMs, as well as the reluctances of the airgap, stator teeth, stator back iron, PMs, rotor poles, and rotor back iron. An operating point of PM has been considered as per the characteristic of BH curve of Arnold N42H magnet as shown in Figure 4.5. Flux density of stator and

rotor core has been chosen iteratively to solve the magnetic circuits as per the BH curve of M19 steel shown in Figure 4.6.

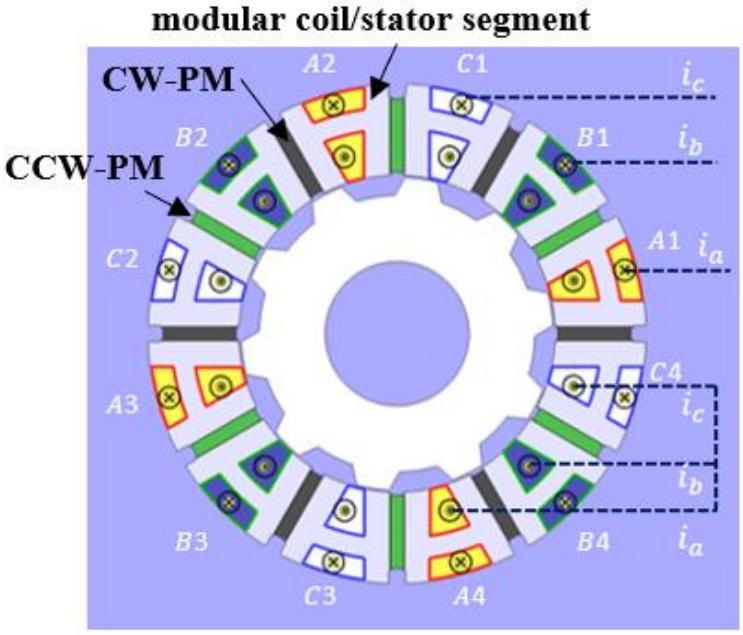

Figure 4.1. Model for 2D FEA schematic of the three-phase special modular machine with 12 concentrated coils and 12 PMs in the stator and 12 protrusions in the rotor.

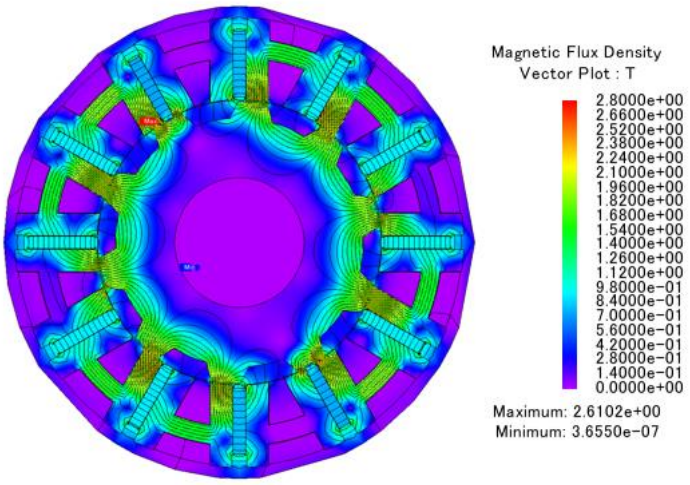

Figure 4.2. Example magnetic field distribution for the motor operation of the three-phase special modular machine with 12 concentrated coils and 12 PMs in the stator and 12 protrusions in the rotor.

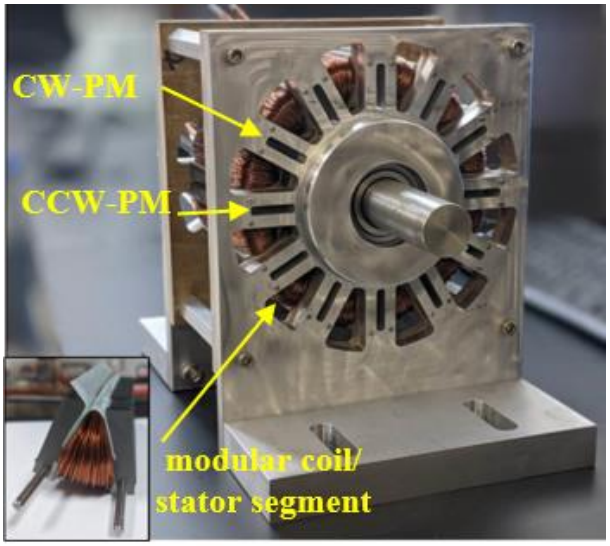

Figure 4.3. Open frame laboratory prototype of the three-phase special modular machine with 12 concentrated coils and 12 PMs in the stator and 12 protrusions in the rotor.

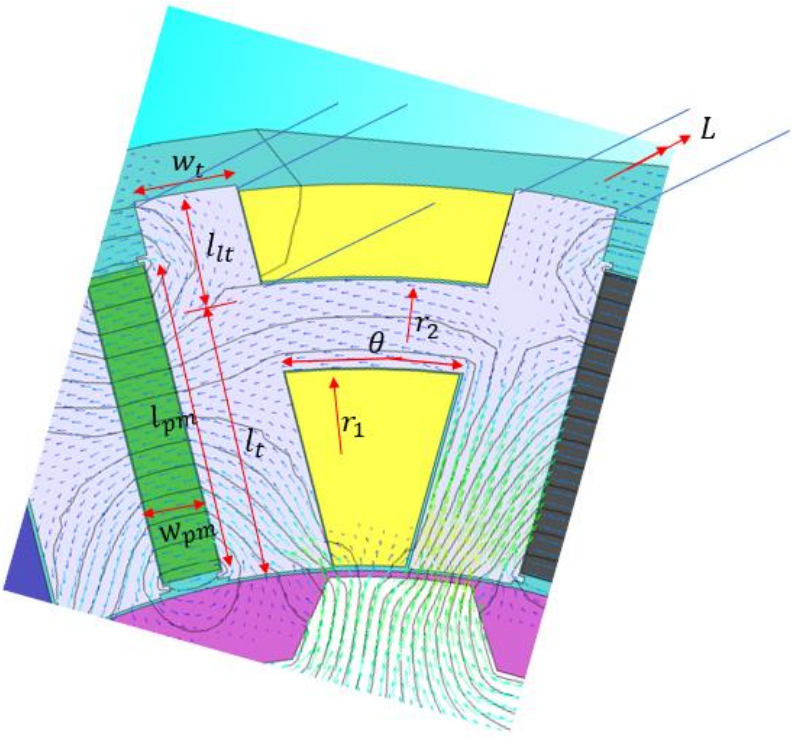

Figure 4.4. 2D schematic of FEA illustrating dimensions of stator segment and PM.

The flux tube methodology reported in [69] was employed to determine the reluctances of the airgap, inner and outer flux leakage paths of stator segments and PMs, the circular part of the stator segments, and the rotor. These flux tubes fall under the category of one of those five variants shown in Figure 4.7. Design matrices of the stator segment and PM have been used to model the MEC for several rotor positions, as shown in Figure 4.4. and Figure 4.8. An LPMEC for the DSPM at a rotor position of 0° was shown in Figure 4.9. The effect of saturation of stator teeth and rotor pole tips has been neglected under open circuit conditions.

TABLE 4.1: DESIGN MATRICES OF STATOR SEGMENT AND PM OF DSPM

Stack Length L	101.66mm
Tooth width w_t	8.38mm
Effective tooth length l_t	23.33mm
Leakage tooth length l_{lt}	8.24mm
Inner radius of core r_1	71.12mm
Outer radius of core r_2	78.26mm
Arc length θ	14.4mm
Width of PM w_{PM}	4.8mm
Radial Length of PM l_{PM}	25.86mm

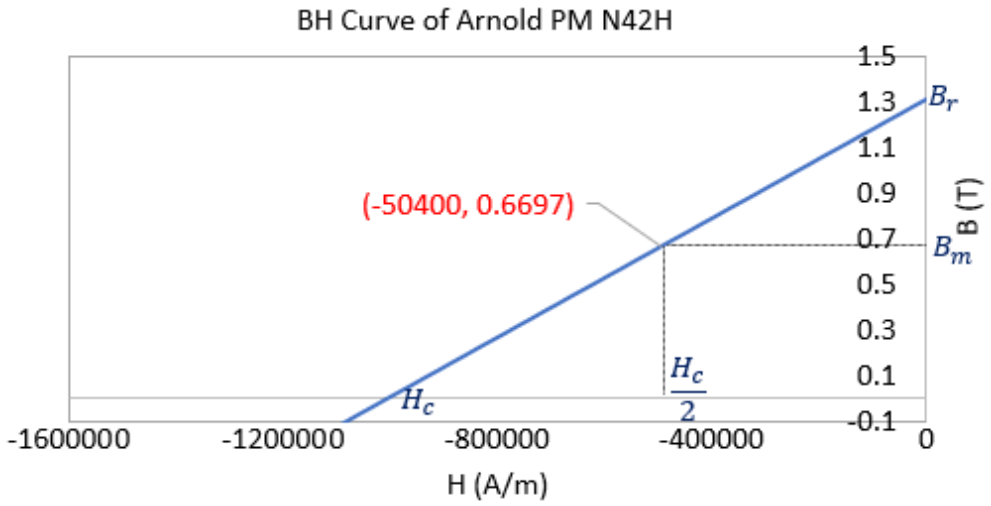

Figure 4.5. Plot of BH curve of Arnold N42H PM showing operating point of the PM.

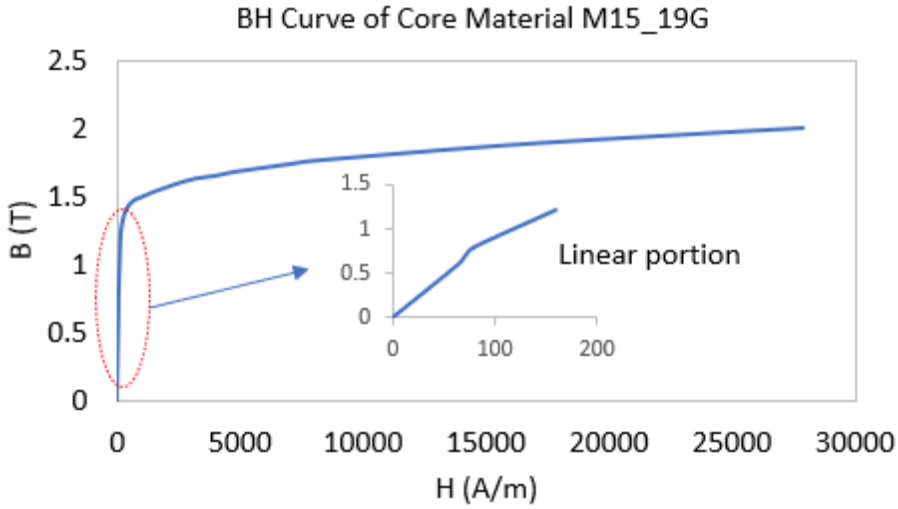

Figure 4.6. Plot of BH curve of stator and rotor core material M19 showing linear portion that has been used to adopt the operating points iteratively to solve LPMECs.

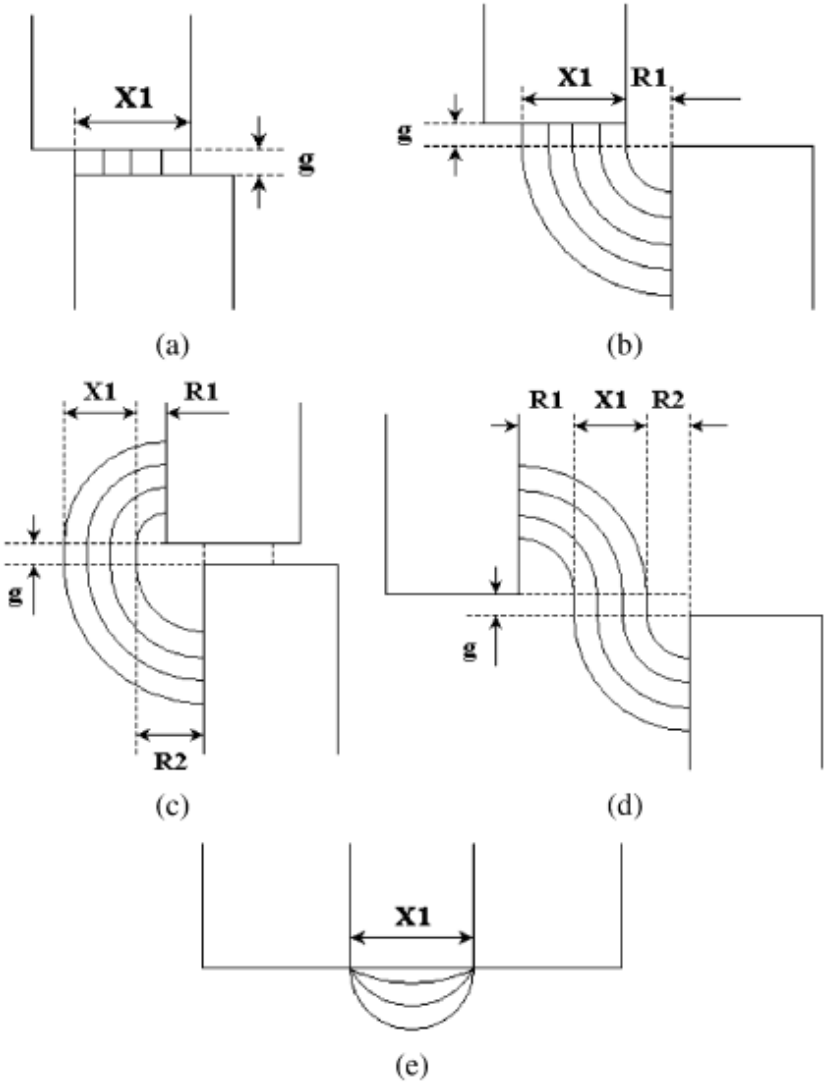

Figure 4.7. Schematic of possible shape of fluxtubes between the stator teeth and pole protrusions [69].

TABLE 4.2: NOMENCLATURE

R_{sol}	Outer leakage reluctance due to flux path in the airgap between upper section of teeth of stator segment
R_{mol}	Outer leakage reluctance due to PM self-linkage flux path in the airgap
R_{msxtx}	Leakage reluctance of x^{th} stator segment of x^{th} teeth of upper section
R_{sxtx}	Reluctance of x^{th} stator segment of x^{th} teeth
R_{sxtxpx}	Reluctance between x^{th} stator segment of x^{th} teeth and x^{th} pole
R_{six}	Reluctance of circular section of the x^{th} stator segment
R_{ri}	Reluctance of circular section of the rotor back iron
R_{pm}	Reluctance of PM
R_{rp}	Reluctance of rotor pole protrusion
F_{pm}	MMF of PM
F_w	MMF of coil
N	Number of tuns of a coil
Ψ_x	Flux linkage of respective path or phase
L_{xx} & L_{xy}	Self and mutual inductances
L_d & L_q	Inductances of d-axis and q-axis
L_o & M_o	Offset values of self and mutual inductances
L_1, L_2, L_3 ...	Harmonic components of self-inductance
M_1, M_2, M_3 ...	Harmonic components of mutual inductance

$$R_{sxtx} = R_{s2t2} = R_{s2t1} = R_{s1t2} = R_{s1t1} = R_{s6t2} = \frac{l_t}{\mu_0 \mu_{rc} w_t L} \tag{4.1}$$

$$R_{msxtx} = R_{ms2t2} = R_{ms2t1} = R_{ms1t2} = R_{ms1t1} = R_{ms6t2} = \frac{l_{Lt}}{\mu_0 \mu_{rc} w_t L} \tag{4.2}$$

$$R_{six} = \frac{\theta}{\mu_o \mu_r \, ln\left(\frac{r_2}{r_1}\right) L} \tag{4.3}$$

$$R_{pm} = \frac{l_{pm}}{\mu_0 \mu_{rpm} w_{pm} L} \tag{4.4}$$

$$F_{pm} = \frac{w_{pm} B_r}{\mu_0 \mu_{rpm}} \tag{4.5}$$

$$F_w = N I_x \tag{4.6}$$

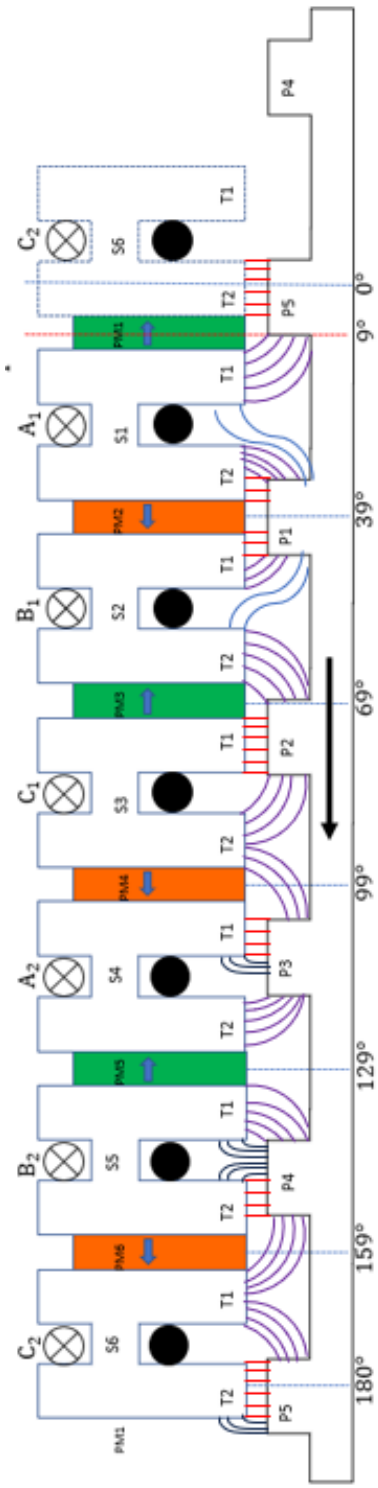

Figure 4.8. Schematic of linear representation of half symmetry model of the DSPM illustrating gramme wound coils in the H-shaped stator segment and formation of flux tubes between stator teeth and rotor pole protrusions.

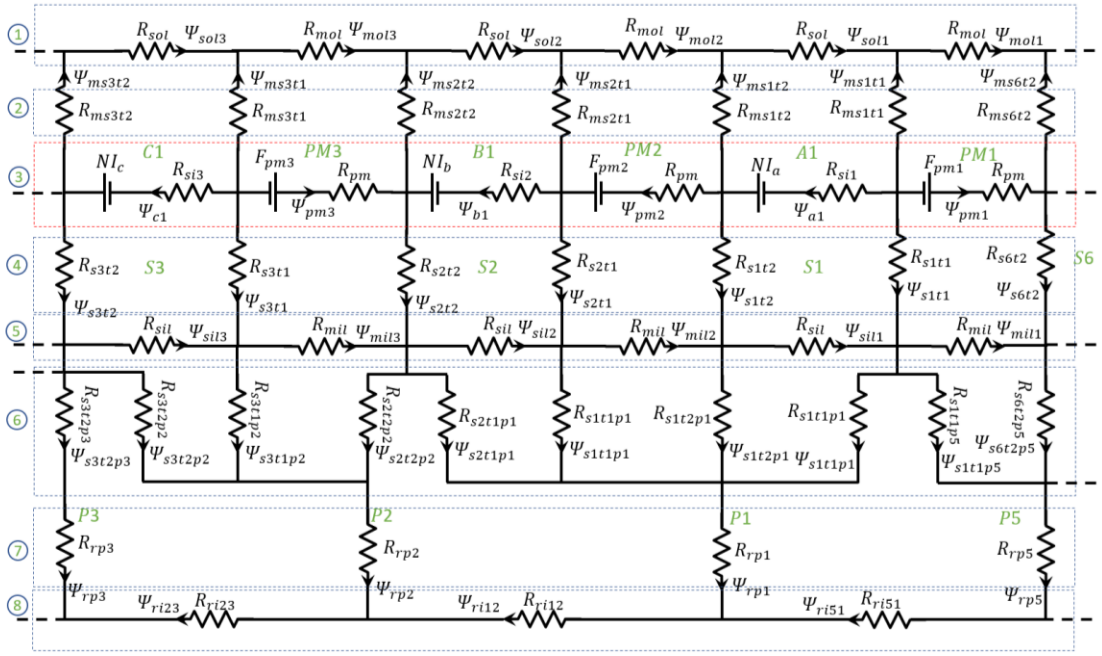

Figure 4.9. Circuit schematic of a portion of LPMEC for the proposed DSPM at a rotor position of 0°. The figure illustrates the following components: 1. Outer leakage reluctances, 2. Stator upper teeth leakage reluctances, 3. Reluctances of PM and stator back iron in series with respective MMFs, 4. Stator segment teeth reluctances, 5. Inner leakage reluctances of PM and stator teeth, 6. Airgap reluctances, 7. Reluctances of rotor pole protrusions, 8. Reluctances of rotor back iron.

4.3. Investigation of Non-Salient Behavior Using LPMEC, FEM, and Experimental Results

The LPMEC was solved for several rotor positions to determine flux linkages with coil A1 and A2 of phase-A, considering half symmetry. Open circuit flux linkages, back EMF, self-inductance, and mutual inductances of phase-A, and dq inductances were empirically solved for several rotor positions using equations (4.7) to (4.13), respective plots were shown in Figure 3, Figure 10, Figure 11, and Figure 12. It has been identified that the presence of spatial harmonics in the self and mutual inductances is almost negligible in machines with a doubly salient structure, such as the proposed DSPM and FSPM, as shown in Figure 13. According to (4.12) and (4.13), the difference between L_d and L_q is negligible due to the lower magnitude of harmonics in the self and mutual inductances. On the other hand, in IPM machines, the magnitude of the harmonics in the self and mutual inductances is high and contributes towards saliency, resulting in synchronous reluctance torque [75].

$$O.C\ flux\ linkages\ of\ phase-A, \Psi_{aPM} = 2(\Psi_{a1} + \Psi_{a2}) \tag{4.7}$$

$$O.C\ back\ EMF\ of\ phase-A, E_a = \omega \frac{d\Psi_{aPM}}{d\theta} \tag{4.8}$$

$$L_{aa} = \frac{\Psi_a}{i_a}; @\ i_b = i_c = 0, PM = air \tag{4.9}$$

$$L_{ab} = \frac{\Psi_a}{i_b}; @\ i_a = i_c = 0, PM = air \tag{4.10}$$

$$L_{ac} = \frac{\Psi_a}{i_c}; @\ i_a = i_b = 0, PM = air \tag{4.11}$$

$$L_d = (L_0 - M_0) - (0.5L_1 + M_1) - (0.5L_2 + M_2) \cdots \tag{4.12}$$

$$L_q = (L_0 - M_0) + (0.5L_1 + M_1) + (0.5L_2 + M_2) \cdots \quad (4.13)$$

Considering the non-saliency behavior as reported in Figure 14., the electromagnetic toque is expressed as (4.14).

$$T = \frac{3}{2} P \Psi_{pm} i_q \quad (4.14)$$

An experimental static toque test has been conducted to identify the torque capability of the OFLP [76]. A comparison of electromagnetic torque performance of the proposed DSPM using LPMEC, FEM, and experimental static torque setup was reported in Figure 15. A peak torque has been observed at 90º; thus, no presence of synchronous reluctance torque has been observed from analytical and experimental validation.

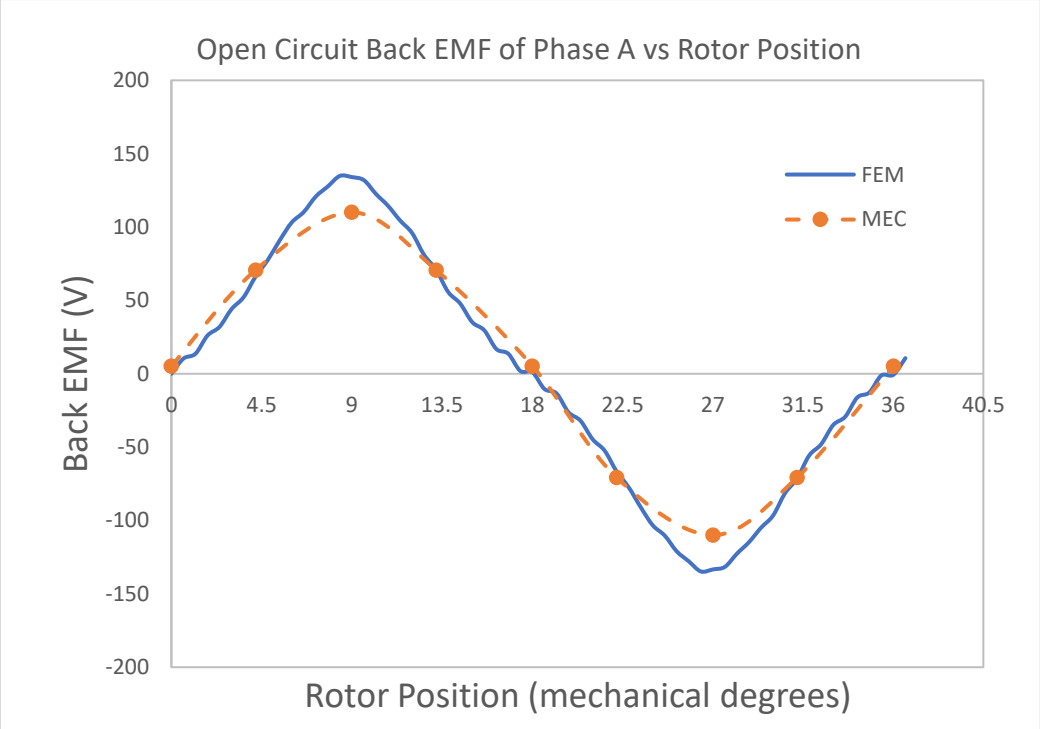

Figure 4.10. Open circuit back EMF of the DSPM from FEM and LPMEC.

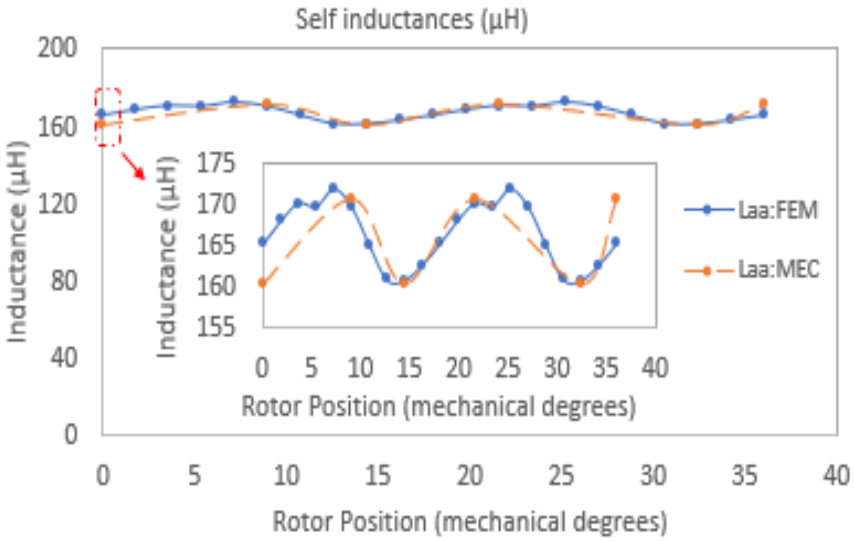

Figure 4.11. Plots of self-inductance L_{aa} phase-A vs rotor position.

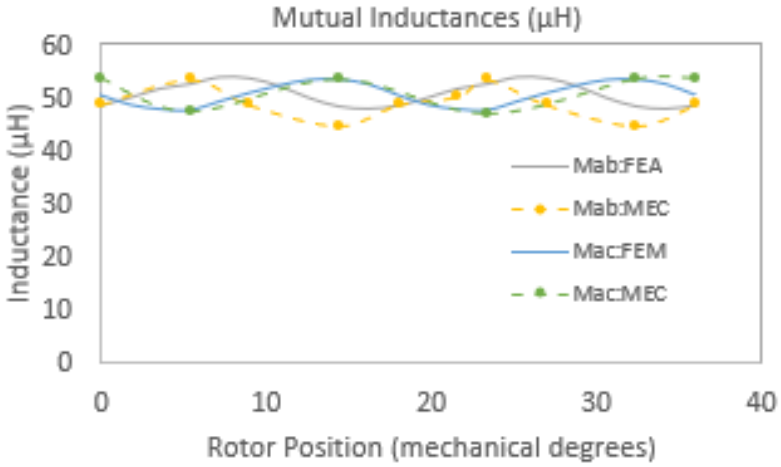

Figure 4.12. Plots of mutual inductances L_{ab} and L_{ac} of phase-A vs rotor position.

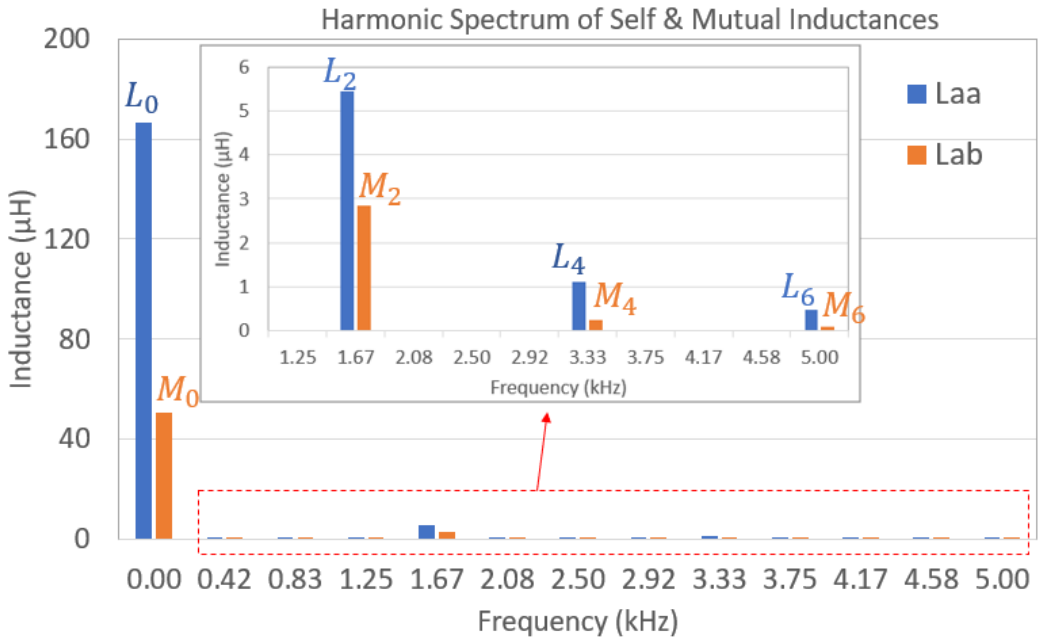

Figure 4.13. Plots of harmonic spectrum of self and mutual inductances for phase-A.

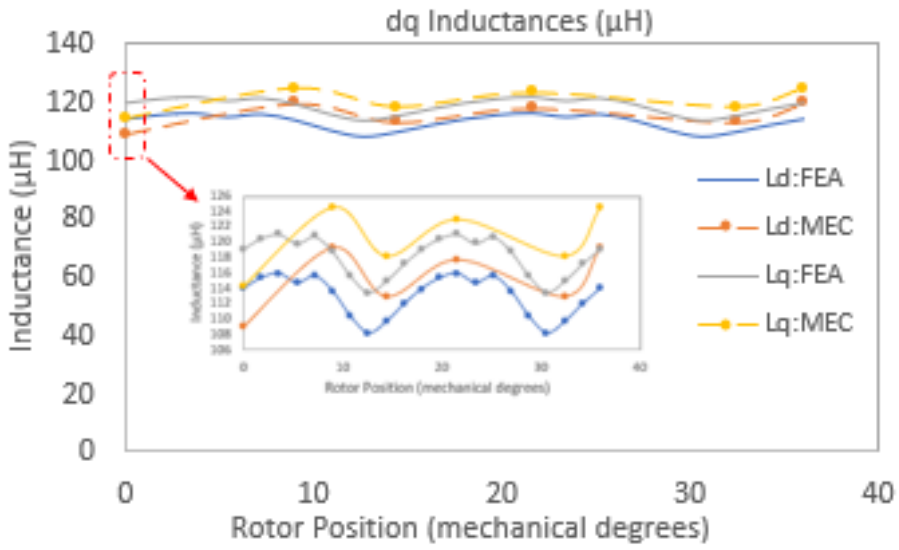

Figure 4.14. Plots of dq inductances L_d and L_q vs rotor position.

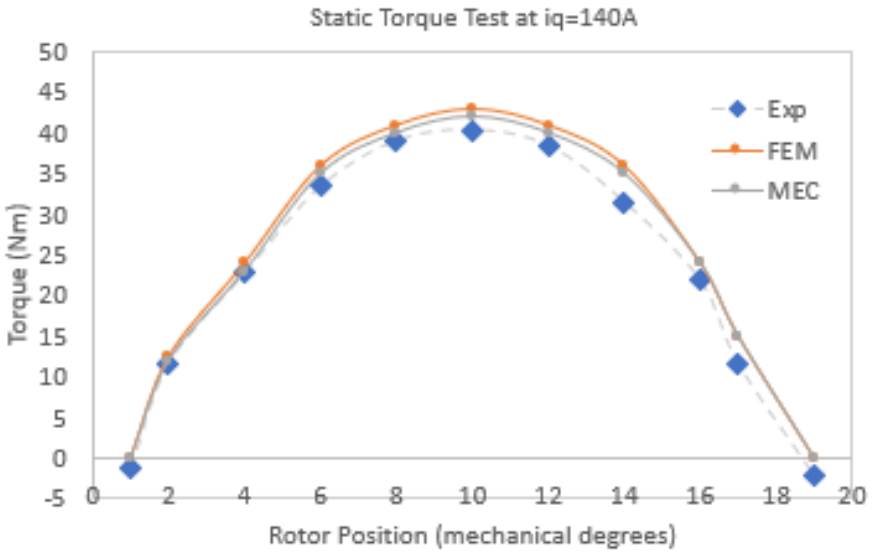

Figure 4.15. Plots of torque versus rotor position employing LPMEC, FEM, and experimental static torque test at i_d=0A and i_q=140A.

Lumped parameter magnetic equivalent circuits (LPMEC) were established for the doubly-salient special machine with PMs in the stator, yielding open circuit flux linkages, back EMF, self and mutual inductances, and dq inductances that were found to be in close agreement with results from finite element analysis. The non-saliency behavior of machine with doubly salient structure was also identified by investigating the presence of spatial harmonics in self and mutual inductances. The negligible harmonics in the self and mutual inductances of the proposed DSPM result in almost negligible equivalent saliency and synchronous reluctance torque. The LPMEC method used in this chapter helped in understanding the key performance indices of the proposed DSPM by iteratively adapting the relative permeability of the core from the BH curve. The experimental static torque test of the open frame laboratory prototype (OFLP), finite element method (FEM), and analytical LPMEC resulted in identical torque versus rotor

position plots. A peak torque of 41 Nm at 90º electrical was reported, further confirming the non-salient behavior observed through the study of spatial harmonics. An improvised method to determine complex flux density in radial and tangential direction for the proposed machine employing conformal mapping will be reported in subsequent works.

CHAPTER 5: MODEL BASED MOTOR DRIVE DEVELOPMENT

Analytical modeling and evaluation of field-oriented control for a high-power density three-phase doubly-salient special machine are presented in this chapter. The special machine contains 12 modular concentrated coils and 12 PMs in the stator and 10 pole protrusions in the rotor. The machine has been designed to operate at a rated torque of 42Nm at a base speed of 5000rpm. A generalized dynamic torque equation and an analytical model for the proposed special machine are established. The dynamic model has been used to realize an equivalent circuit by applying the synchronous reference frame theory. A high-fidelity plant model of the special machine has been developed using FEA software, and the machine characteristics have been imported into motor drive simulation software for speed control analysis. A field-oriented control technique for the special machine in synchronous reference frame has been implemented to regulate the speed over a wide range in both constant torque and field weakening regimes for electric vehicle traction applications. Stability analysis for the controller has been presented and verified by simulations in continuous domain.

5.1. Introduction

Non-salient behavior of the motor has been studied based on prior work [76]. A field-oriented control technique for the special machine has been developed similar to surface permanent magnet motor. Constant torque angle or maximum torque per Ampere (MTPA) and constant current constant power (CCCP), or constant voltage constant power (CVCP) control algorithms can be employed to the proposed motor drive system [57]. FEA simulation software has been used to analyze the electromagnetic performance and to develop a high-fidelity plant model for the proposed special machine. The high-fidelity

plant model has been imported into power electronics and drives simulation platform to implement the field-oriented control algorithms.

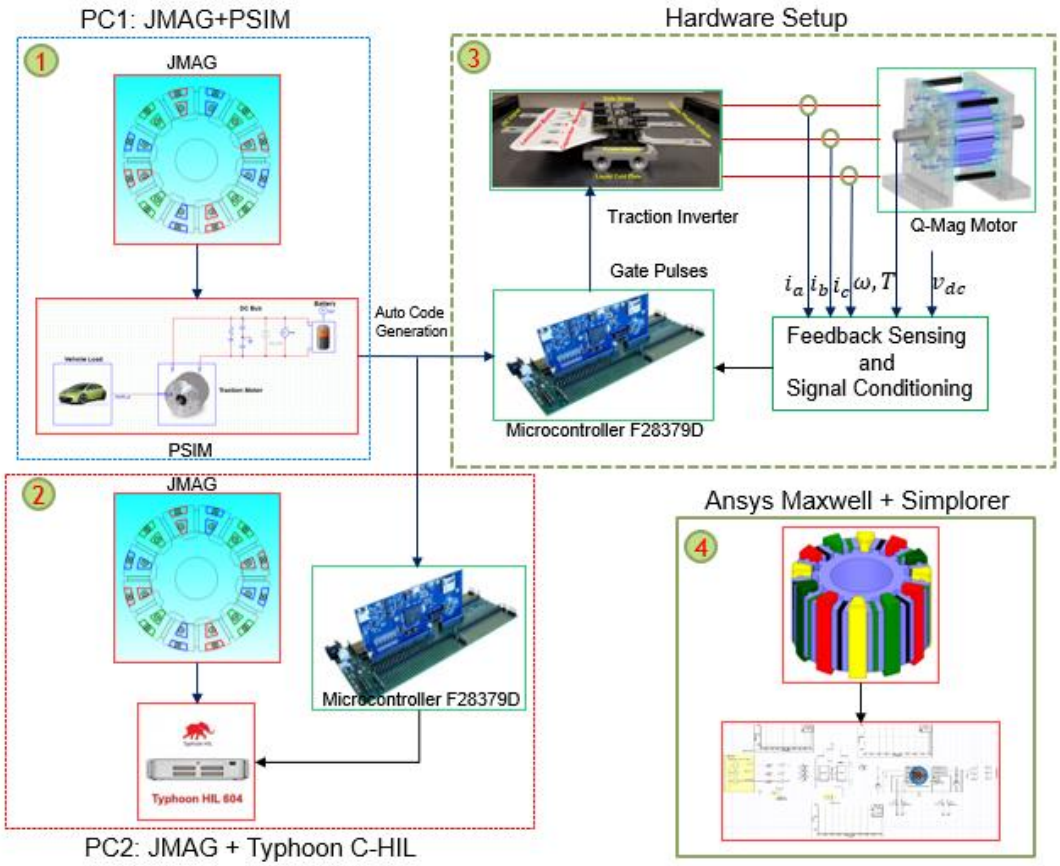

Figure 5.1. Schematic of workflow of model-based motor drive development. Step 1: Exporting high-fidelity plant model of the machine from FEA software to simulation platform. Step 2: Validation of control algorithms employing controller hardware in loop strategy (C-HIL) using TI DSP F28379D and Typhoon HIL 604. Step 3: Experimental validation of control algorithms for the OFLP of the motor and SiC based traction inverter drive system employing F28379D. Step 4: Optional co-simulation strategy to validate control algorithms.

5.2. Modeling of High-Power Density PM Motor

The behavioral characteristics of the special machine have been recognized to be similar to those of non-salient motors despite the double-saliency structure. This observation is based on the results of back EMF and static torque tests reported in [76], in which a sinusoidal back EMF and sinusoidal torque with a peak at 90° (electrical) were presented. Thus, the rotor torque in this machine is a combination of (a) electromagnetic torque caused by the interaction between the flux set up by three-phase currents and PMs and (b) cogging torque due to PMs alone [65] as expressed in (5.1). Due to the sinusoidal nature of the back EMF, the airgap flux linkages, and the rotor position-dependent electromagnetic torque, synchronous reference frame theory has been applied to the plant model.

The flux lines from the permanent magnets between the modular coils in the stator link with three-phase windings through a low reluctance path offered by the rotor. Thus, the flux linkages due to permanent magnets are a function of the rotor position as expressed in (5.2). The total flux linkages with the three-phase windings are due to the three-phase currents and permanent magnets are expressed as in (5.3). Thus, the three-phase voltages are expressed as a rate of change of total flux linkages, in addition to the voltage drop due to the winding resistance as expressed in (5.4). The three-phase voltages are transformed into the synchronous frame by applying Clarke's transformation and Park's transformation as detailed in [77] to establish (5.5).

$$T = \left(i_a i_{pm} \frac{\partial L_{a-pm}}{\partial \theta} + i_b i_{pm} \frac{\partial L_{b-pm}}{\partial \theta} + i_c i_{pm} \frac{\partial L_{c-pm}}{\partial \theta}\right) + \frac{1}{2} i_{pm}^2 \frac{\partial L_{pm}}{\partial \theta} \qquad (5.1)$$

$$\left[\Psi_{abc-pm}\right] = \begin{bmatrix}\Psi_{a-pm}\\ \Psi_{b-pm}\\ \Psi_{c-pm}\end{bmatrix} = \begin{bmatrix}cos\,\theta_r\\ cos\left(\theta_r - \frac{2\pi}{3}\right)\\ cos\left(\theta_r + \frac{2\pi}{3}\right)\end{bmatrix}\Psi_{pm} \tag{5.2}$$

$$\lambda_{total} = \begin{bmatrix}L_{aa} & L_{ab} & L_{ac}\\ L_{ba} & L_{bb} & L_{bc}\\ L_{ca} & L_{cb} & L_{cc}\end{bmatrix}\begin{bmatrix}i_a\\ i_b\\ i_c\end{bmatrix} + \begin{bmatrix}\Psi_{a-pm}\\ \Psi_{b-pm}\\ \Psi_{c-pm}\end{bmatrix} = \left[L_{abc}\right]\left[i_{abc}\right] + \left[\Psi_{abc-pm}\right] \tag{5.3}$$

$$\left[v_{abc}\right] = R\left[i_{abc}\right] + \frac{d}{dt}\left(\left[L_{abc}\right]\left[i_{abc}\right] + \left[\Psi_{abc-pm}\right]\right) \tag{5.4}$$

$$\begin{bmatrix}v_d^e\\ v_q^e\end{bmatrix} = \begin{bmatrix}R & 0\\ 0 & R\end{bmatrix}\begin{bmatrix}i_d^e\\ i_q^e\end{bmatrix} + \begin{bmatrix}L_d^e & 0\\ 0 & L_q^e\end{bmatrix}\frac{d}{dt}\begin{bmatrix}i_d^e\\ i_q^e\end{bmatrix} + \begin{bmatrix}0 & -\omega L_q^e\\ \omega L_d^e & 0\end{bmatrix}\begin{bmatrix}i_d^e\\ i_q^e\end{bmatrix} + \begin{bmatrix}0\\ \omega\end{bmatrix}\Psi_{pm} \tag{5.5}$$

By neglecting the winding resistance and assuming the rate of change in the currents in (5.5) as negligible under steady-state conditions, the output power and torque are expressed as in equations (5.6) and (5.7). An equivalent circuit of the proposed special machine has been realized from the expression (5.5) is shown in Figure 5.2.

$$P_o = \frac{3}{2}\begin{bmatrix}v_d^e & v_q^e\end{bmatrix}\begin{bmatrix}i_d^e\\ i_q^e\end{bmatrix} = \frac{3}{2}\omega\left(i_d^e i_q^e\left(L_d^e - L_q^e\right) + \Psi_{pm} i_q^e\right) \tag{5.6}$$

$$T_e = \frac{\mathrm{P}_o}{\omega_m} = \frac{3}{2}P\left(i_d^e i_q^e\left(L_d^e - L_q^e\right) + \Psi_{pm} i_q^e\right) \approx \frac{3}{2}P\Psi_{pm} i_q^e \tag{5.7}$$

A high-fidelity plant model has been developed using JMAG-RT. Using parametric sweeps, the currents versus inductances mappings as shown in Figure 5.3 were derived. These mappings were imported into PSIM software as 2D-lookup tables. The currents in synchronous frame are results of absolute power-invariant conversion [78]. These Currents may need to be scaled as amplitude invariant depending upon the transformation strategy.

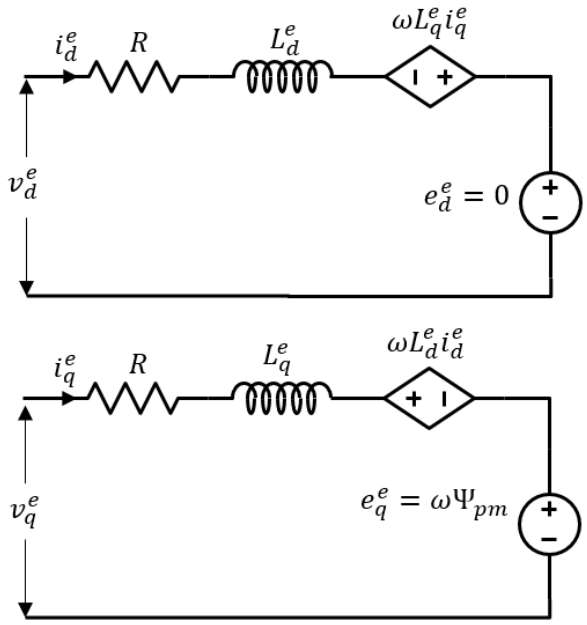

Figure 5.2. Schematic of the dq equivalent circuit of the proposed special machine in the synchronous reference frame.

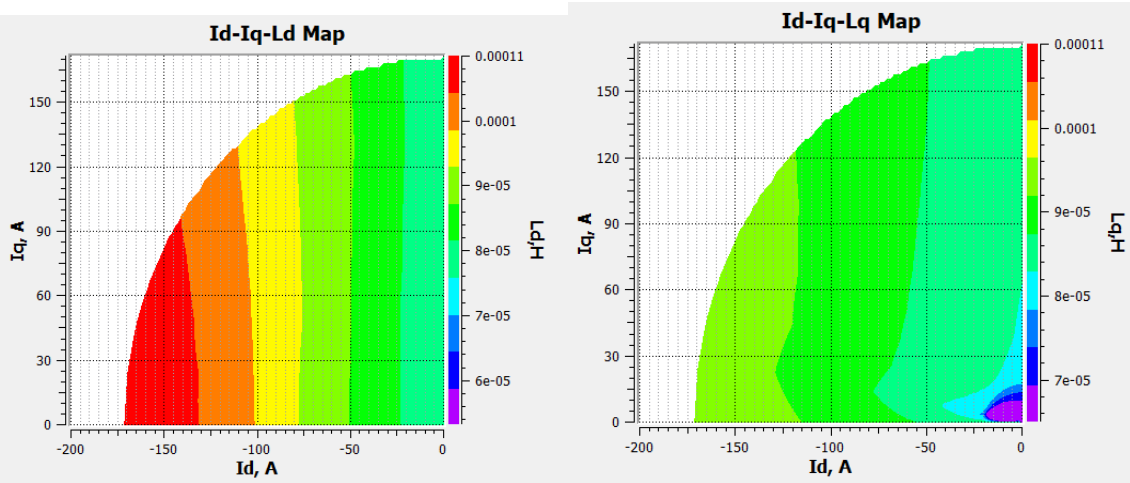

Figure 5.3. d-axis and q-axis currents versus inductance mapping of the special machine imported from high-fidelity plant model.

5.3. Control Methodology Employing High-Fidelity Plant Model

Field-oriented control methodologies of surface PM machine (SPM) apply to the special machine considering the non-salient behavior. Thus, speed regulation in constant torque regime till base speed is achieved by applying constant torque angle control by commanding zero d-axis current. Constant voltage and constant power (CVCP) control methodology has been applied in the field weakening regime to regulate the speeds above the base speed [58], [59]. The parameters from the high-fidelity plant model of the motor have been imported into the controller to consider the variation of inductances with respect to the currents in the synchronous reference frame. The overall control methodology is shown in Figure 5.4. consisting of a plant model, speed controller, field-oriented current controller, and high-fidelity characteristics of currents versus inductance block. The plant model realized from (5.5), (5.6), and (5.7) consists of cross-coupling between the d-axis and q-axis. Outputs of the current controllers have been adjusted to cancel out the effect of cross-coupling by embedding decoupling terms. It must be noted that the JMAG-RT tool applies power invariant form to transform the three-phase currents into the synchronous frame, but PSIM uses power variant form. Thus, a scaling factor of √(2/3) has been applied to the magnitudes of dq currents entered in the lookup tables.

5.3.1. Boundary Conditions

The machine has been designed to operate at a rated RMS current of 98.4A to deliver a torque of 42Nm at a base speed of 5000rpm and at a maximum RMS current of 124A at maximum speed. The inductances at the rated operating point are found to be $L_d^e \approx L_q^e$ =116μH. The flux linkage constant $\Psi_{pm} = 0.022$ has been determined from the back EMF test. Equation (5.5) has been modified to express the electrical speed as in (5.8). The

expression of speed in (5.8) has been adjusted to define voltage constraint is expressed in (5.9) which is an equation of circle because of non-saliency $L_d^e \approx L_q^e$ as shown in Figure 5.4. The current limiting circle is defined by the maximum current carrying capacity of the winding as expressed in (5.10). The saturation limits of the speed controller and current controllers have been chosen to operate within the current and voltage limits defined by the constraints in (5.8) and (5.10). The critical speed ω_c for the CVCP control methodology is determined by (5.11) [79].

$$\omega_e = p\omega_m = \frac{V_s = v_{max}}{\sqrt{(L_q i_{q\mathrm{m}}^e)^2 + (L_d i_{d\mathrm{m}}^e + \psi_{pm})^2}} \tag{5.8}$$

$$\frac{\left(\left(\frac{\psi_{pm}}{L_d}\right) + i_d^e\right)^2}{\frac{V_s^{\,2}}{(\omega_e L_d)^2}} + \frac{i_q^{e\,2}}{\frac{V_s^{\,2}}{(\omega_e L_q)^2}} = 1 \tag{5.9}$$

$$\hat{I}_s^{\,2} = i_d^{e\,2} + i_q^{e\,2} \le I_{max} \tag{5.10}$$

$$If\ \frac{\Psi_{pm}}{L_d} > I_{max};\ \omega_c = \frac{V_{max}}{p(\Psi_{pm} - L_d I_{max})} \tag{5.11}$$

$$i_{dref}^e = \frac{\omega_{base}}{\omega_e}\frac{\Psi_{pm}}{L_d} - \frac{\Psi_{pm}}{L_d} \tag{5.12}$$

$$v_s = \sqrt{v_d^{e\,2} + v_q^{e\,2}} \tag{5.13}$$

5.3.2. Constant Torque Angle or MTPA Control

The proposed machine has been operated in constant torque angle mode or MTPA mode for regulating speeds below the rated speed as reported in [57] based on (5.8). The speed controller generates a reference current $\hat{I}_s$. The current $i_{qref}^e = \hat{I}_s$ because $i_{dref}^e = 0$ in the constant torque regime. Thus, the torque is proportional to i_{qref}^e and speed is regulated in accordance with (5.8). The operating point of the machine follows the MTPA trajectory in this regime as shown in Figure 5.4.

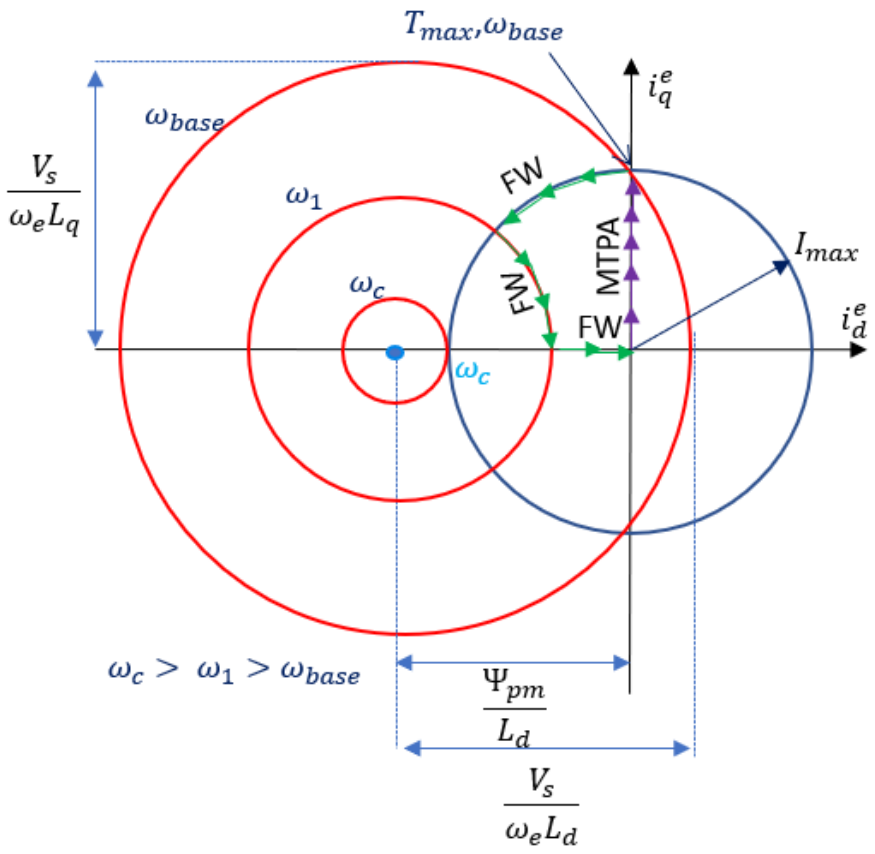

Figure 5.4. Current and voltage constraints of the proposed machine: MTPA trajectory for speeds below rated speed and field weakening trajectory for the speeds above rated speed [57].

5.3.3. Field Weakening Control

At base speed, the machine reaches the maximum voltage and current capability of the drive as defined in (5.8). The controller has leverage over the d-axis current only to regulate the speeds above the rated speed. Therefore, a negative d-axis current will be introduced against PM flux to weaken the overall flux linkages with the stator winding following the expression formulated by applying the CVCP control strategy [59]. The voltage output of the current controllers defined in (5.13) has been monitored to compare

with the maximum voltage capability of the traction inverter. The multiplexer chooses input 1 ($i^e_{dref} = 0$) or input 2 as defined in (5.12) based on the magnitude of the voltage. The maximum speeds ω_c for different voltages are calculated and shown in TABLE 5.1.

TABLE 5.1. CRITICAL SPEED OF THE MOTOR DRIVE SYSTEM [58], [79]

Parameters	**V_{max}**	**N_c**
$L^e_d \approx L^e_q$ =116μH, I_{rated} =98.4Arms, I_{max} =124Arms, and Ψ_{pm} =0.022V_{peak}/krpm	135Vac	9125 rpm
	270Vac	18250 rpm

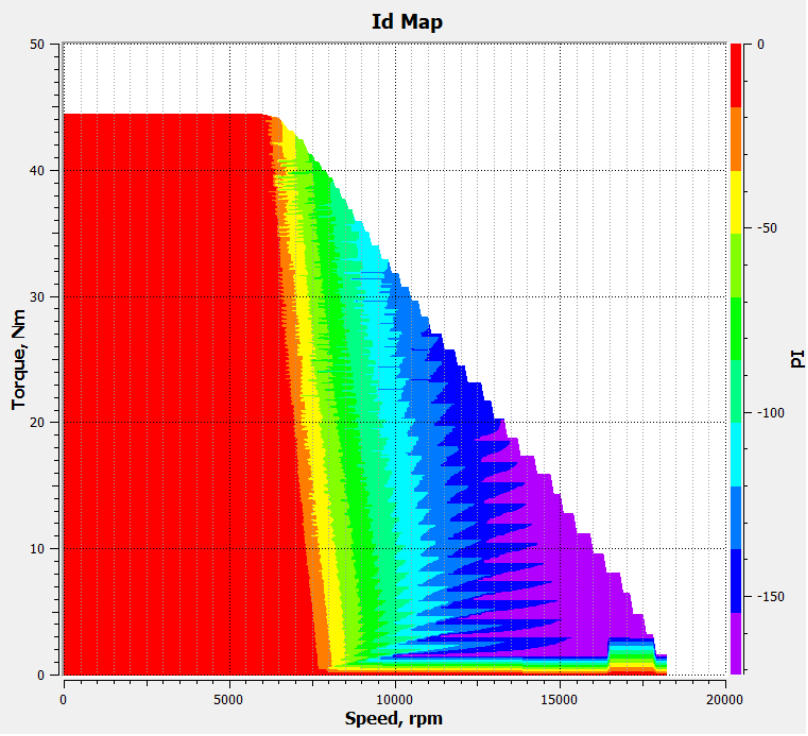

Figure 5.5. Speed versus torque plots showing the mapping of the power invariant d-axis currents in the constant torque and field weakening regime generated by JMAG-RT.

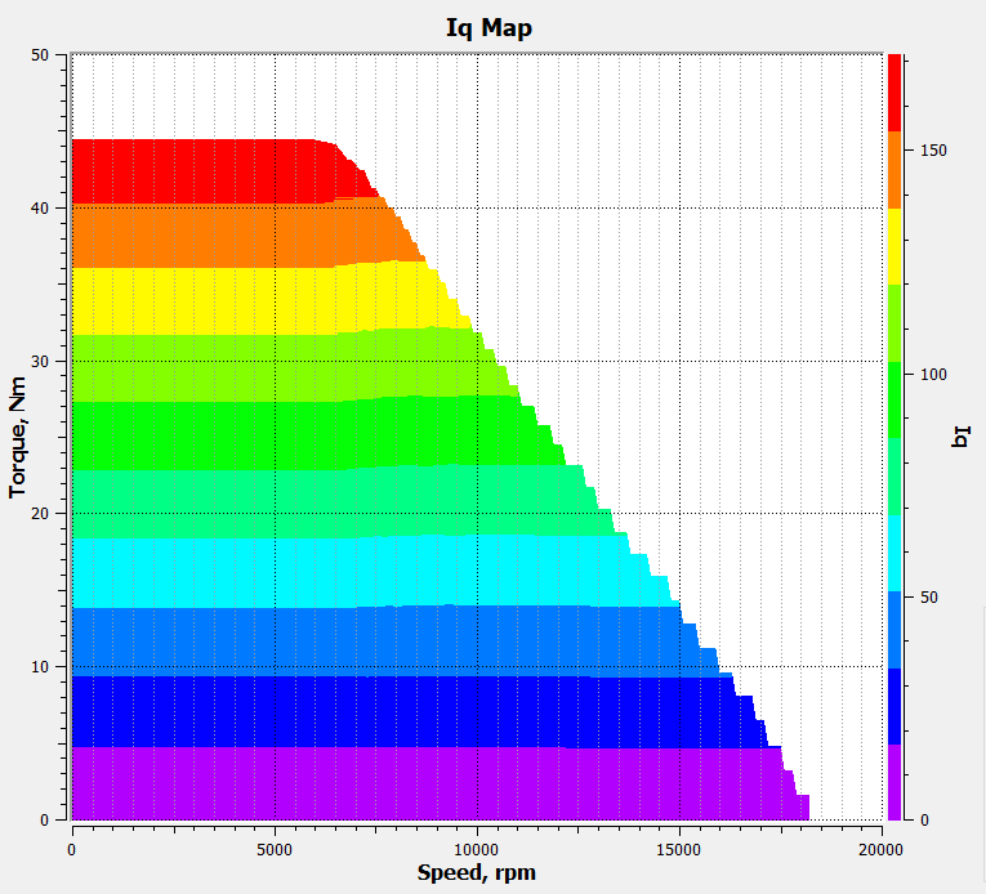

Figure 5.6. Speed versus torque plots showing the mapping of the power invariant q-axis currents in the constant torque and field weakening regime generated by JMAG-RT.

5.4. Stability Analysis

The overall control strategy shown in Figure 5.7. has been simplified to analyze the stability of the motor drive system, as shown in Figure 5.8. The effect of the cross-coupling has been canceled out by the decoupling block. Considering low values of inductances from the plant model, series path proportional integral (PI) controllers have been chosen to have more leverage over the placement of poles and zeros precisely [80].

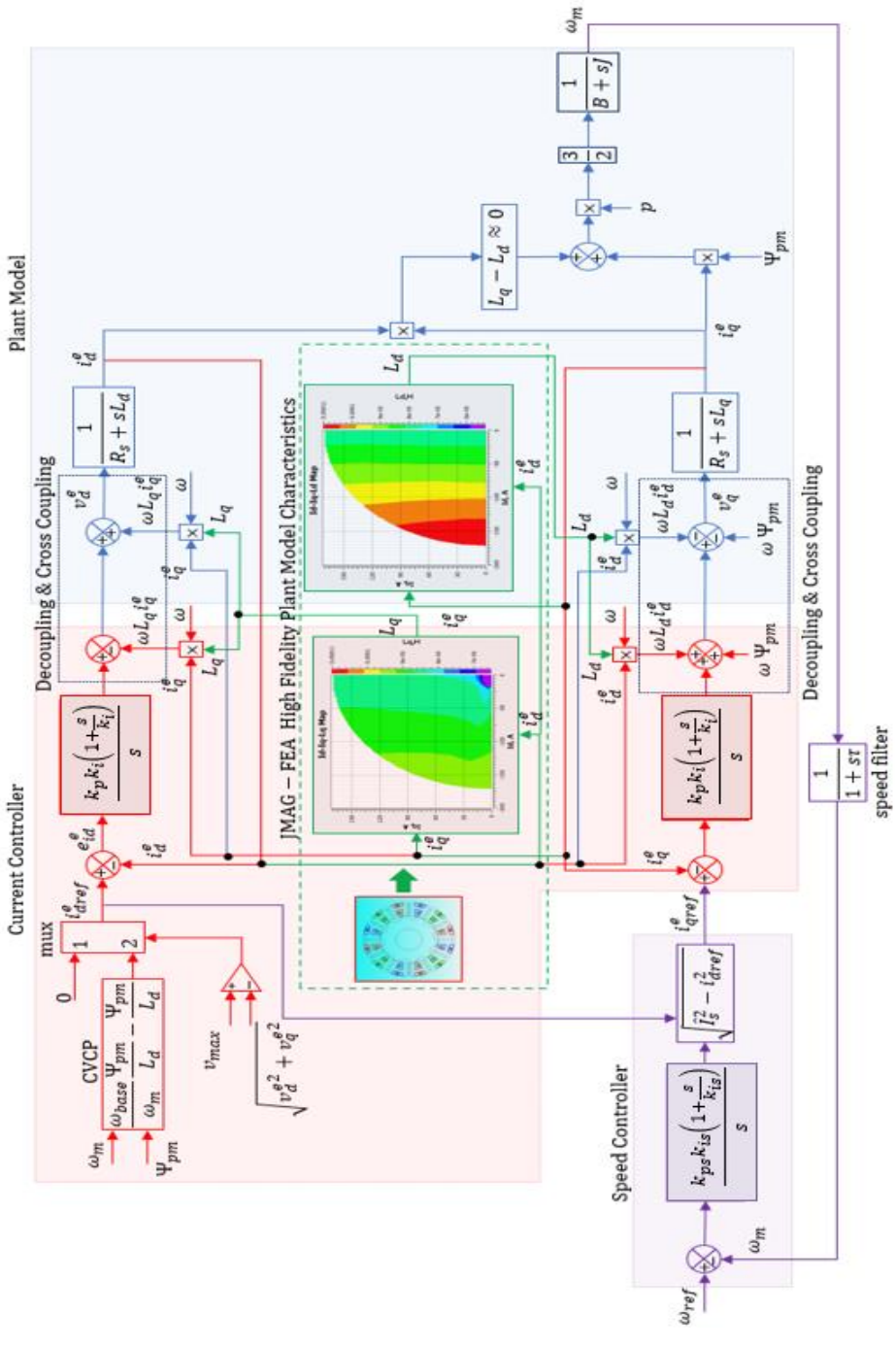

Figure 5.7. Schematic of overall field-oriented control block diagram of the special machine with characteristics imported from the high-fidelity plant model.

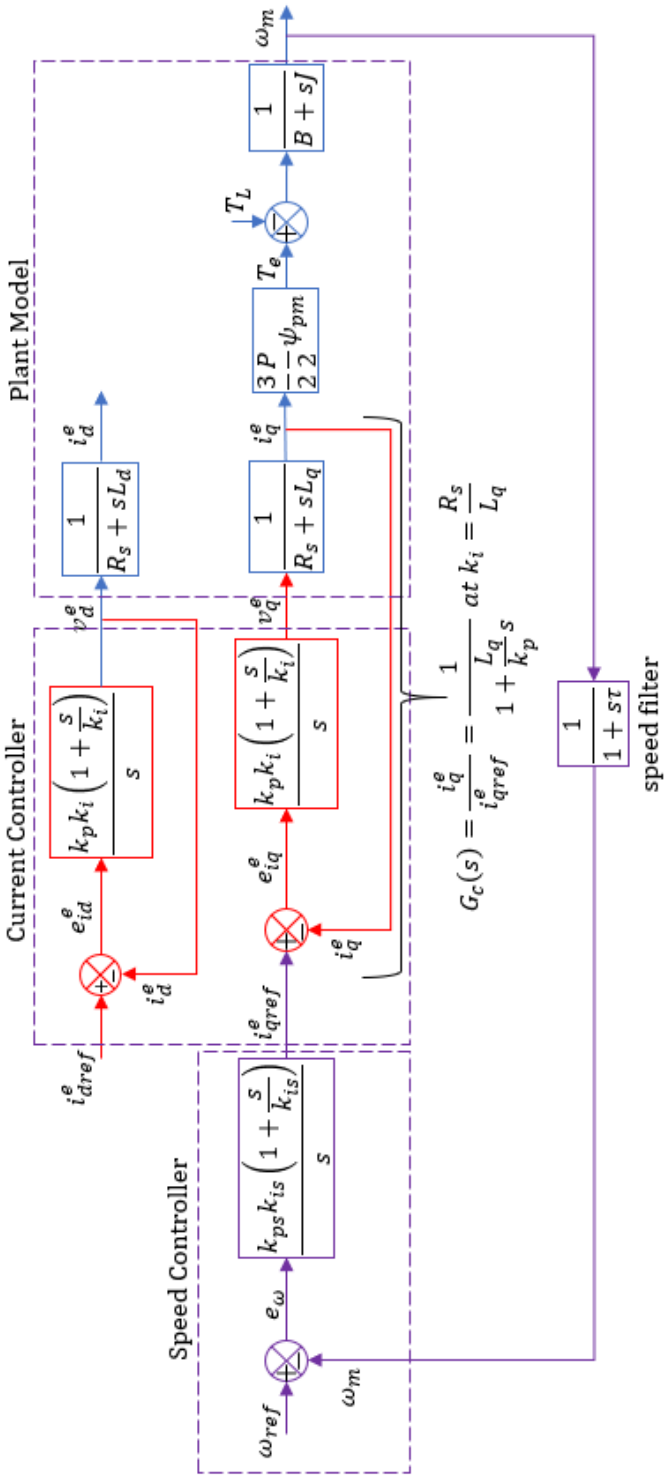

Figure 5.8. Schematic of the simplified control block diagram of the proposed motor drive system.

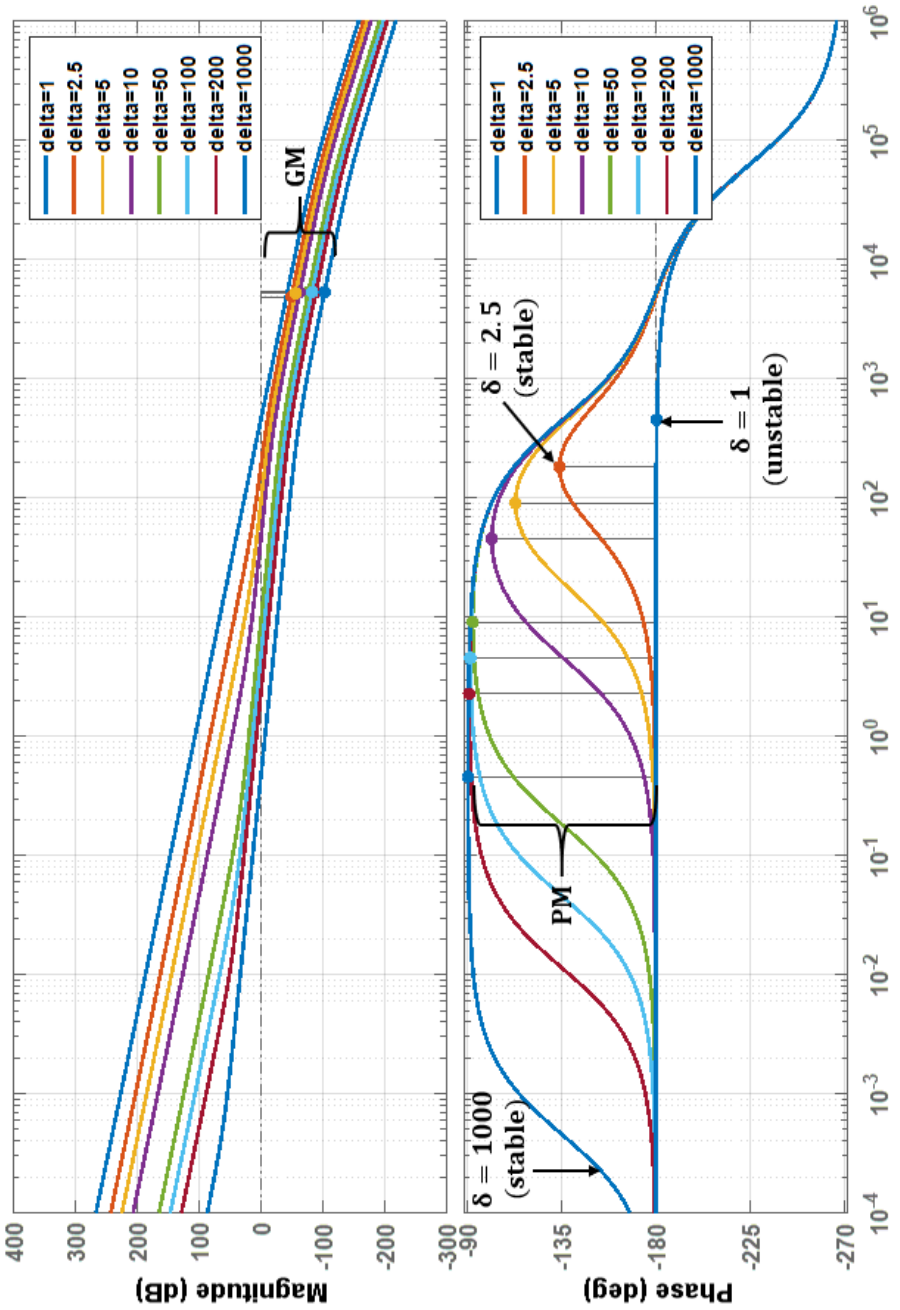

Figure 5.9. Bode plot of the composite transfer function for the proposed special motor drive system.

The integral constant of the current controller has been chosen as $k_i = \frac{R_s}{L_q}$ to cancel out the pole and zero to result in a closed-loop current transfer function $G_c(s)$ as shown in the Figure 5.8 [80]. Thus, the overall composite transfer function of the q-axis closed-loop system by neglecting the friction coefficient B and considering the speed filter as $H(S)$ is expressed as (5.15). The control parameters have been tuned according to the expressions reported TABLE 5.2. in which δ is called damping factor, and the constant k is expressed as (5.14). The time constant of the filter τ=2.2ms, an inertia of 0.00179kg-mm2 and 10 pole pairs have been chosen to determine the proportional and integral constants of speed and current controllers $k_{ps}, k_{is}, k_p, and\ k_i$ for several values of δ. The sampling time T_s has to be chosen for discrete time domain analysis. A Bode diagram has been plotted to identify the stability margins. The system is stable for all values of δ except $\delta \leq 1$. The stability margins and crossover frequencies as shown in Figure 5.9. have been reported in TABLE 5.3. Simulation results are reported in Chapter 7.

$$k = 1.5 \times no.of\ pole\ pairs \times inertia \tag{5.14}$$

$$G_c(s) = G(s)H(s) \approx \frac{kk_{ps}k_{is}\left(1 + \frac{S}{k_{is}}\right)}{s^2\left(1 + \frac{L_q}{k_p}s\right)(\tau S + 1)} \tag{5.15}$$

TABLE 5.2. EXPRESSIONS FOR PROPORTIONAL AND INTEGRAL CONSTANTS

Current Controller		**Speed Controller**	
$\frac{10L_q}{\delta\tau} < k_p < \frac{\pi L_q}{T_s}$	$k_i = \frac{R_s}{L_q \approx L_d}$	$k_{ps} = \frac{1}{\delta k \tau}$	$k_{is} = \frac{1}{\delta^2 \tau}$

TABLE 5.3. SYSTEM CHARACTERISTICS FOR VARIOUS VALUES OF DAMPING FACTOR

δ	**Phase Margin (degrees)**	**Gain Margin (dB)**	**Phase Crossover Frequency ω_{pc} (rad/s)**	**Gain Crossover Frequency ω_{gc} (rad/s)**	**Stability**
1000	89.9	103	5340	0.455	yes
200	89.4	88.9	5340	2.27	yes
100	88.8	62.8	5340	4.55	yes
50	87.7	76.9	5320	9.09	yes
10	78.5	62.8	5320	45.5	yes
5	67.3	56.5	5240	91	yes
2.5	46.2	49.3	4890	182	yes
1	-	-	-	-	no

CHAPTER 6: COMPLEX VECTOR CURRENT REGULATION STRATEGY

A complex vector current (CVC) regulation strategy for a high-power dense proposed special machine with 12 modular concentrated coils and 12 PMs in the stator and 10 pole protrusions in the rotor is presented in this chapter. The special machine has been designed to operate at a rated torque of 41Nm at a base speed of 5000RPM. A plant model of the special machine has been developed using FEA software. The phase flux linkage and inductance have substantial variations with the rotor position and therefore variations and possible errors are expected for the estimation of d-q inductances. Classical current regulation strategy in synchronous reference frame with or without decoupling is not capable of stable operation if uncertainty in the estimation of d-q inductances has been considered to determine proportional and integral constants of the controller. Thus, considering a wide range of uncertainty in the estimation of d-q inductances, the CVC regulation strategy has been employed for this special machine. A comparative analysis of classical and CVC regulation strategies has been presented in this digest for both maximum torque per ampere and field weakening control regimes to regulate the torque or speed over a wide range for electric vehicle traction applications. A detailed stability analysis reveals that the CVC regulation strategy is more robust compared to the classical proportional integral current regulation strategy in synchronous reference frame with decoupling. The performance of these two current regulation strategies has been validated by simulations in continuous domain and verified by employing controller hardware in the loop (CHIL).

6.1. Introduction

The three-phase topology of the special machine with 12 PMs and 12 concentrated modular toroidal coils (4 coils in series per phase) in the stator and 10 rotor pole protrusions as shown in Figure 5.4 has been considered in this chapter. The phase flux linkage and inductance have substantial variations with the rotor position and therefore variations and possible errors are expected for the estimation of d-q inductances. In this regard, the CVC regulation strategy has been analyzed to address robustness of the controller with errors in estimation of d-q inductances. In a classic proportional integral current control strategy in synchronous reference frame (SRF-PI) detailed in Chapter 5, proportional and integral constants ($k_p=\hat{r}\times\omega_{bw}$ & $k_i=\hat{L}\times\omega_{bw}$) and decoupling voltages ($\omega\hat{L}_dI_q$ & $\omega\hat{L}_qI_d$) are sensitive to the estimates of plant model [81].

Any error in the estimation of inductances of the plant model results in improper placements of complex zeros created by the SRF-PI current controller with decoupling. Thus, the complex zeros created by SRF-PI and complex poles of the plant model will not be canceled out. The effect of cross-coupling voltages will become obvious and may result in unstable operation or limit the speed or torque capability of the motor drive system within a small bandwidth. In this regard, to address the error in the estimation of inductances, without losing the speed or torque capabilities of the proposed machine, a complex vector current (CVC) regulation strategy has been employed A comparative analysis of SRF-PI and CVC current regulation strategies have been detailed in this chapter.

6.2. Synchronous Reference Frame Proportional Integral (SRF-PI) Current Control Strategy

The plant model of the proposed machine in synchronous reference frame is expressed as (6.1) either in scalar or complex vector form. A modified form of complex vector representation of the plant model, considering back EMF compensation is expressed in time domain and frequency domain as (6.2). A control schematic of SRF-PI current regulation strategy in complex form is shown in Figure 6.1. Thus, the transfer function of complex vector plant model is expressed as (6.3) has a pair of complex conjugate poles at $S_{p1,2} = -\frac{R}{L} \pm j\omega$.

$$\begin{bmatrix} v_d^e \\ v_q^e \end{bmatrix} = \begin{bmatrix} R & 0 \\ 0 & R \end{bmatrix} \begin{bmatrix} i_d^e \\ i_q^e \end{bmatrix} + \begin{bmatrix} L_d^e = L & 0 \\ 0 & L_q^e = L \end{bmatrix} \frac{d}{dt} \begin{bmatrix} i_d^e \\ i_q^e \end{bmatrix} + \begin{bmatrix} 0 & -\omega L_q^e \\ \omega L_d^e & 0 \end{bmatrix} \begin{bmatrix} i_d^e \\ i_q^e \end{bmatrix} + \begin{bmatrix} 0 \\ \omega \end{bmatrix} \Psi_{pm}$$

or

$$v_{qd}^e = R i_{qd}^e + L \frac{d}{dt}\left(i_{qd}^e\right) \pm j\omega L i_{qd}^e + \omega \Psi_{pm} \tag{6.1}$$

$$v_{qd}^e = R i_{qd}^e + L \frac{d}{dt}\left(i_{qd}^e\right) \pm j\omega L i_{qd}^e \tag{6.2}$$

or

$$V_{qd}^e(S) = (R + Ls \pm j\omega L) I_{qd}^e(S)$$

$$I_{qd}^e(S)/V_{qd}^e(S) = \frac{1}{R + Ls \pm j\omega L} \tag{6.3}$$

complex conjugate poles $S_{p1,2} = -\frac{R}{L} \pm j\omega$

The speed dependent decoupling voltages are embedded to move the complex conjugate poles to real poles and the respective transfer function is expressed in (6.4) with poles at $S_{p1,2} = -\frac{R}{L} \pm j\omega \mp \frac{j\omega \hat{L}}{L}$.

$$\frac{I_{qd}^{e}(S)}{V_{qd}^{e*}(S)} = \frac{1}{R + Ls \pm j\omega L \mp j\omega\hat{L}} \tag{6.4}$$

$$\text{poles } S_{p1,2} = -\frac{R}{L} \pm j\omega \mp \frac{j\omega\hat{L}}{L} = -\frac{R}{L} \text{ if } \hat{L} = L$$

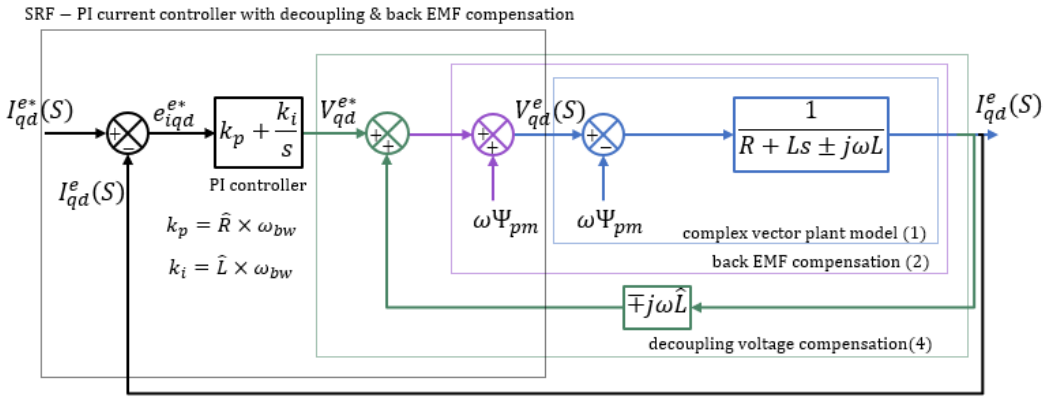

Figure 6.1. Control block diagram of SRF-PI current regulation strategy with decoupling and back EMF compensation in complex vector representation.

Thus, the complex conjugate poles will be transitioned into real poles if estimated inductance $\hat{L} = L$. The PI controller is tuned as $k_p = \hat{R} \times \omega_{bw}$ and $k_i = \hat{L} \times \omega_{bw}$ to have zeros at $S_{z1,2} = -R/\hat{L}$. Thus, real zeros created by PI controller cancels the real poles of plant only if $\hat{L} = L$. Any deviation in estimation of inductance will not cancel out the poles and presence of cross-coupling voltages is imminent. A control block diagram of SRF-PI current regulation strategy with decoupling and back EMF compensation has been shown in Fig. 4. The closed loop transfer function is expressed as (6.5).

$$\frac{I_{qd}^{e}(S)}{I_{qd}^{e*}(S)} = \frac{k_p s + k_i}{Ls^2 + \left(R \pm j\omega\left(L - \hat{L}\right) + k_p\right)s + k_i} \tag{6.5}$$

Thus, multiple loops in the classical SRF-PI current control strategy are dependent on $\hat{L}$ will have adverse effect on overall performance of the controller in case of errors in the

estimated values of inductances. For Bode plot analysis, the control transfer function (6.5) of classical SRF-PI is transformed into stationary reference frame by substituting s=s-jω [82] and expressed as (6.6).

$$\frac{I_{qd}^{s}(S)}{I_{qd}^{s*}(S)} = \frac{k_p s + k_i}{Ls^2 + \left(R \pm j\omega\left(L - \hat{L}\right) + k_p\right)s + k_i \mp \omega^2\hat{L} - j\omega\left(k_p + R\right)} \tag{6.6}$$

6.3. Complex Vector Current (CVC) Control Strategy

In CVC control strategy, controller has been simplified further by eliminating estimated inductance dependent decoupling voltage terms. A simplified complex vector representation of CVC control strategy has been shown in Figure 6.2.

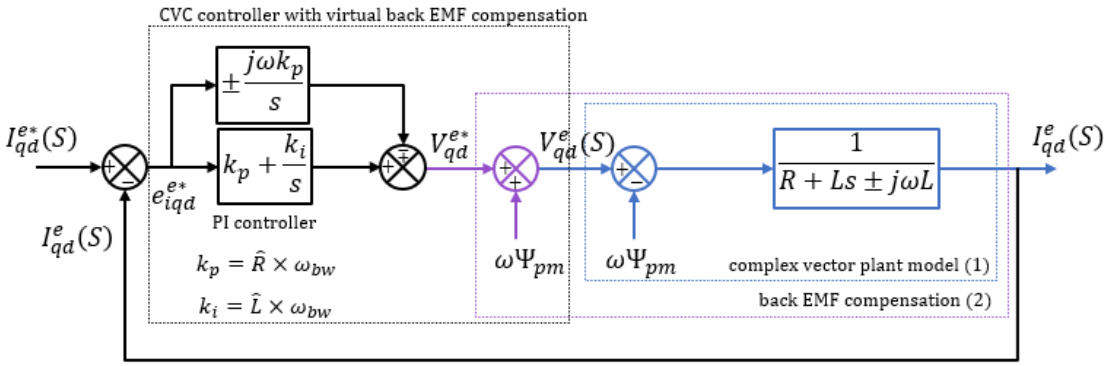

Figure 6.2. Control block diagram of CVC regulation strategy with back EMF compensation.

The control parameters in CVC are tuned to have complex conjugate zeros $S_{z1,2} = -\frac{k_i}{k_p} + j\omega = -\frac{\hat{R}}{\hat{L}} \pm j\omega$ to cancel out the complex conjugate poles of plant model $S_{p1,2} =$

$-\frac{R}{L} \pm j\omega$. Thus, overall closed loop transfer function of the CVC current control strategy is expressed as (6.7).

$$\frac{I_{qd}^{e}(S)}{I_{qd}^{e*}(S)} = \frac{k_p s + k_i + jk_p\omega}{Ls^2 + \left(R \pm j\omega L + k_p\right)s + k_i + jk_p\omega} \tag{6.7}$$

For Bode plot analysis, the control transfer functions (6.7) of CVC control strategy is transformed into stationary reference frame by substituting s=s-jω [82] and expressed as and (6.8).

$$\frac{I_{qd}^{s}(S)}{I_{qd}^{s*}(S)} = \frac{k_p s + k_i}{Ls^2 + \left(R \pm j\omega L + k_p\right)s + k_i - j\omega R} \tag{6.8}$$

6.4. Stability Analysis of SRF-PI and CVC Control Strategies

The proposed special machine with 10 pole protrusions, equivalent to 20 electrical poles, can operate at a rated and maximum fundamental frequency of 833.33Hz and 2833.33Hz corresponding to a rated and maximum speed of 5000RPM and 17000RPM. As the fundamental frequency reaches to 2833.33Hz, the controller bandwidth has been chosen as 833.33Hz and 3000Hz to account for the maximum fundamental frequencies corresponding to constant torque and field weakening regimes. Stationary reference frame equivalents of synchronous reference frame transfer functions (6.6) and (6.8) have been used to analyze the frequency response as reported in Figure 6.3 and Figure 6.4. Continuous domain simulation results and discrete domain C-HIL results are reported in Chapter 7.

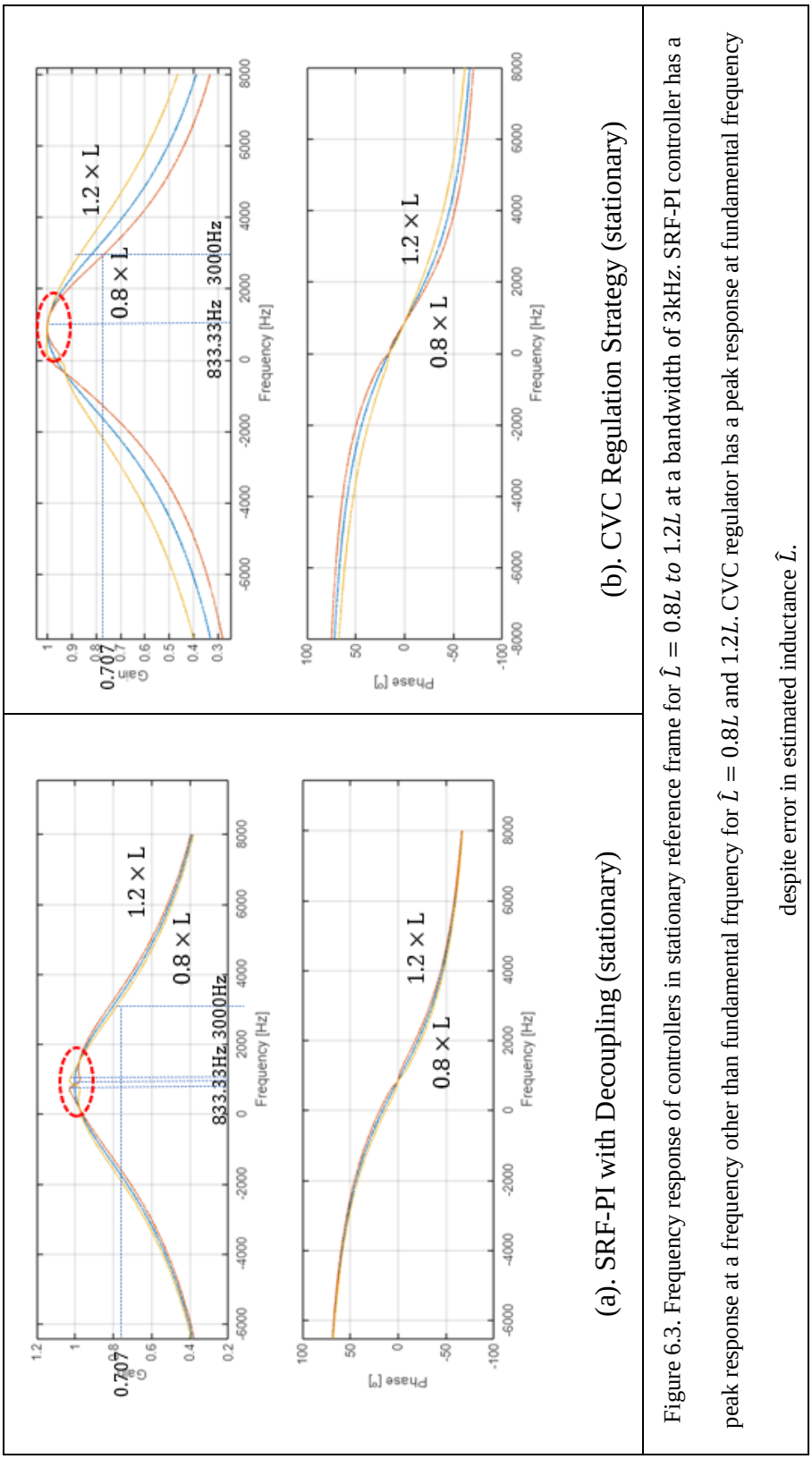

(a). SRF-PI with Decoupling (stationary)

(b). CVC Regulation Strategy (stationary)

Figure 6.3. Frequency response of controllers in stationary reference frame for $\hat{L} = 0.8L$ *to* $1.2L$ at a bandwidth of 3kHz. SRF-PI controller has a peak response at a frequency other than fundamental frquency for $\hat{L} = 0.8L$ and $1.2L$. CVC regulator has a peak response at fundamental frequency despite error in estimated inductance $\hat{L}$.

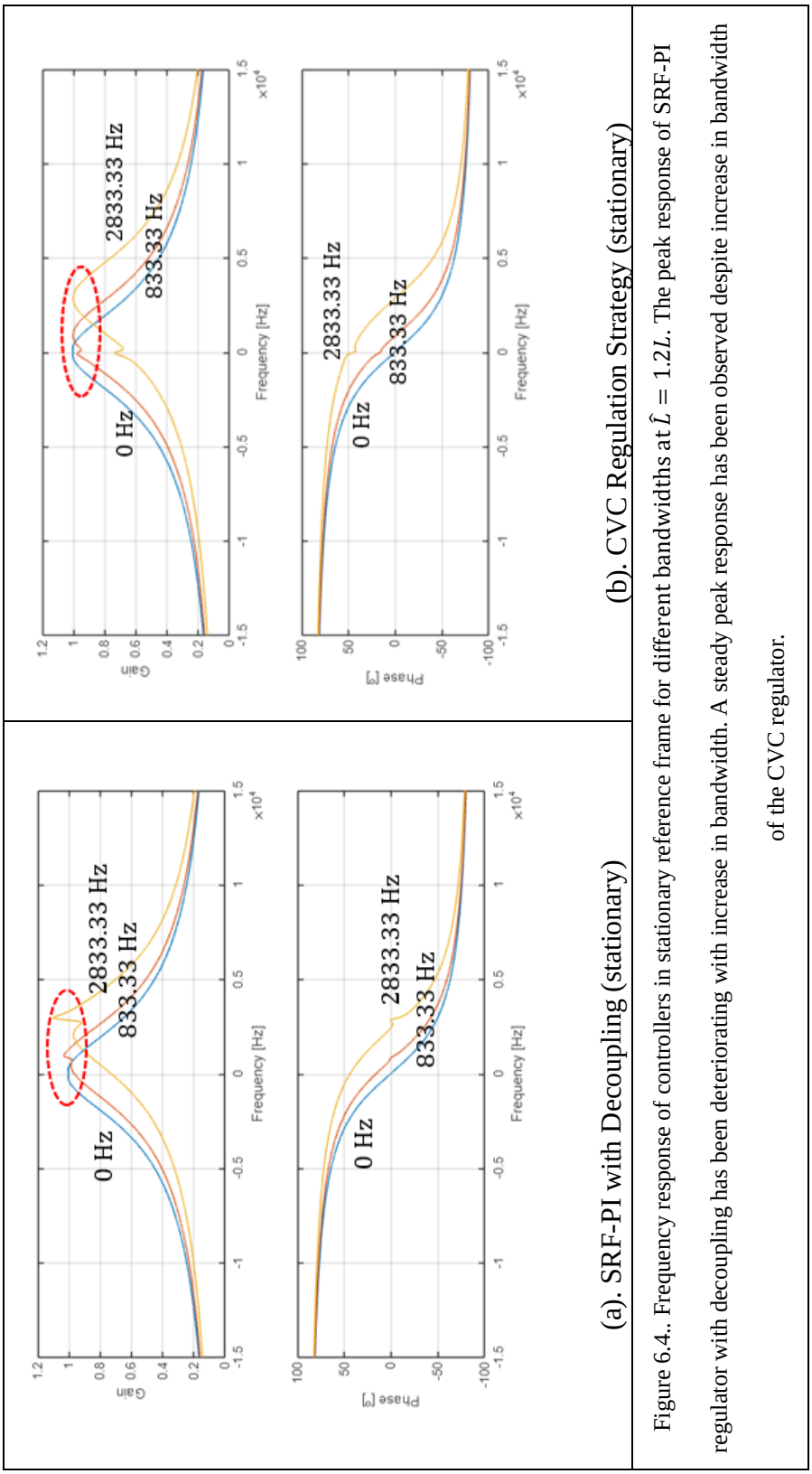

Figure 6.4.. Frequency response of controllers in stationary reference frame for different bandwidths at $\hat{L} = 1.2L$. The peak response of SRF-PI regulator with decoupling has been deteriorating with increase in bandwidth. A steady peak response has been observed despite increase in bandwidth of the CVC regulator.

CHAPTER 7: SIMULATION & C-HIL RESULTS

7.1. Introduction

This chapter is focused on presenting the continuous time-domain simulation results and validation of control algorithms employing C-HIL detailed in Chapter 6 and Chapter 7. Speed and torque control strategies employing model-based workflow are reported in Section 7.1. Continuous domain simulation results of comparative analysis of SRF-PI and CVC regulation strategies are reported in Section 7.2. Discrete time-domain simulation results employing C-HIL using TI DSP Delfino F28335 and Typhoon HIL 604 are reported in Section 7.3.

7.2. Simulation Results of Model Based Motor Drive System

Continuous domain simulations have been performed using PSIM considering the current versus inductance mapping and cross decoupling to account for the flux linkages for the specifications of the proposed motor drive system reported in TABLE 7.1. The speed controller and current controllers have been tuned precisely with anti-windup feature to limit the current and voltages within the safe limits of the motor drive system.

TABLE 7.1. SPECIFICATIONS OF THE SPECIAL MOTOR DRIVE SYSTEM.

$\mathbf{V_{dc}}$ $(\mathbf{V})$	$\mathbf{f_{sw}}$ $(\mathbf{kHz})$	$\mathbf{I_{rated}}$ $(\mathbf{A})$	$\mathbf{I_{max}}$ $(\mathbf{A})$	$\mathbf{T}$ $(\mathbf{Nm})$	$\mathbf{N_{rated}}$ $(\mathbf{rpm})$	$\mathbf{\Psi_{pm}}$ $\mathbf{V(peak)/krpm}$	$\mathbf{P}$	$\mathbf{J}$ $(\mathbf{kg-mm^2})$
500	20-40	98.4	124	42	5000	0.022	20	0.00179

The constant torque angle or MTPA and field weakening control algorithms have been implemented for a speed range of 17000rpm as shown in Figure 7.1. The control algorithms have been verified at switching frequencies 20-40kHz over a wide speed range in both

constant torque and constant power regimes. Successful validation of motor control at 42Nm output torque has been performed upto the rated speed of 5000rpm. The constant power regime has been identified in the field weakening region between 5000rpm and 17000rpm at reduced output torque levels. Presence of cogging torque has been reflected as a ripple in the torque and currents. An improvement in torque and current ripples has been observed at higher switching frequencies in both operating regions as shown in Figure 7.2. and Figure 7.3.

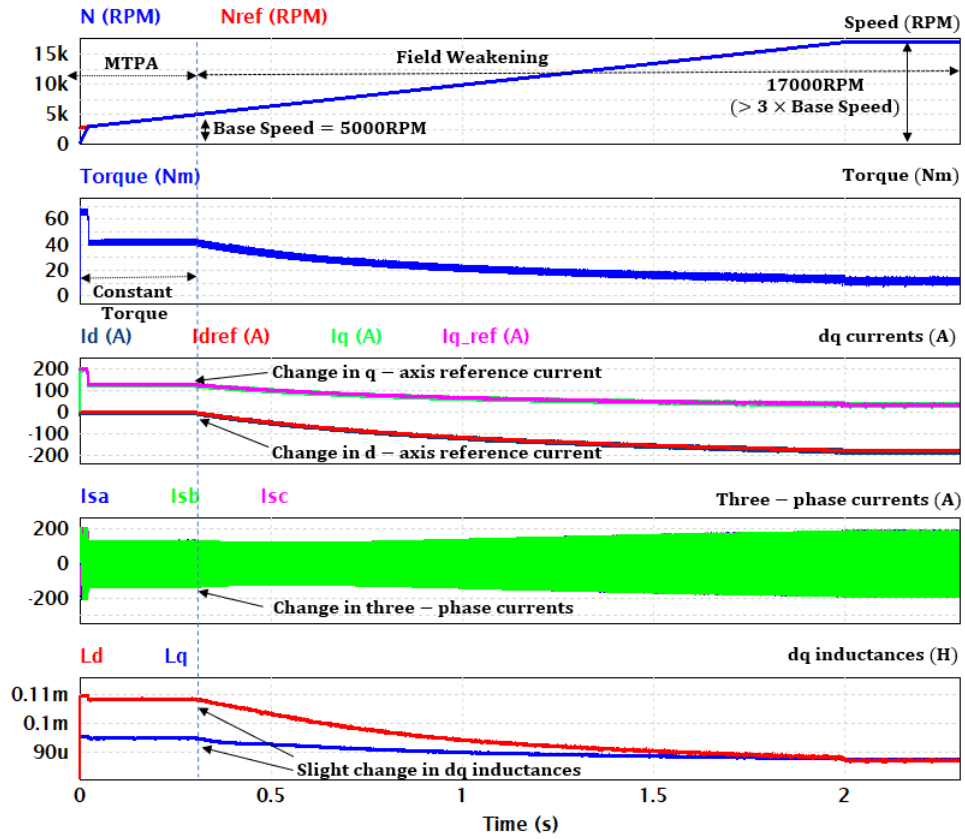

Figure 7.1. PSIM simulation results of the proposed special motor drive system transitioning from MTPA region to field weakening region for a change in speed from 2000rpm to a maximum speed of 17000rpm at a switching frequency of 40kHz.

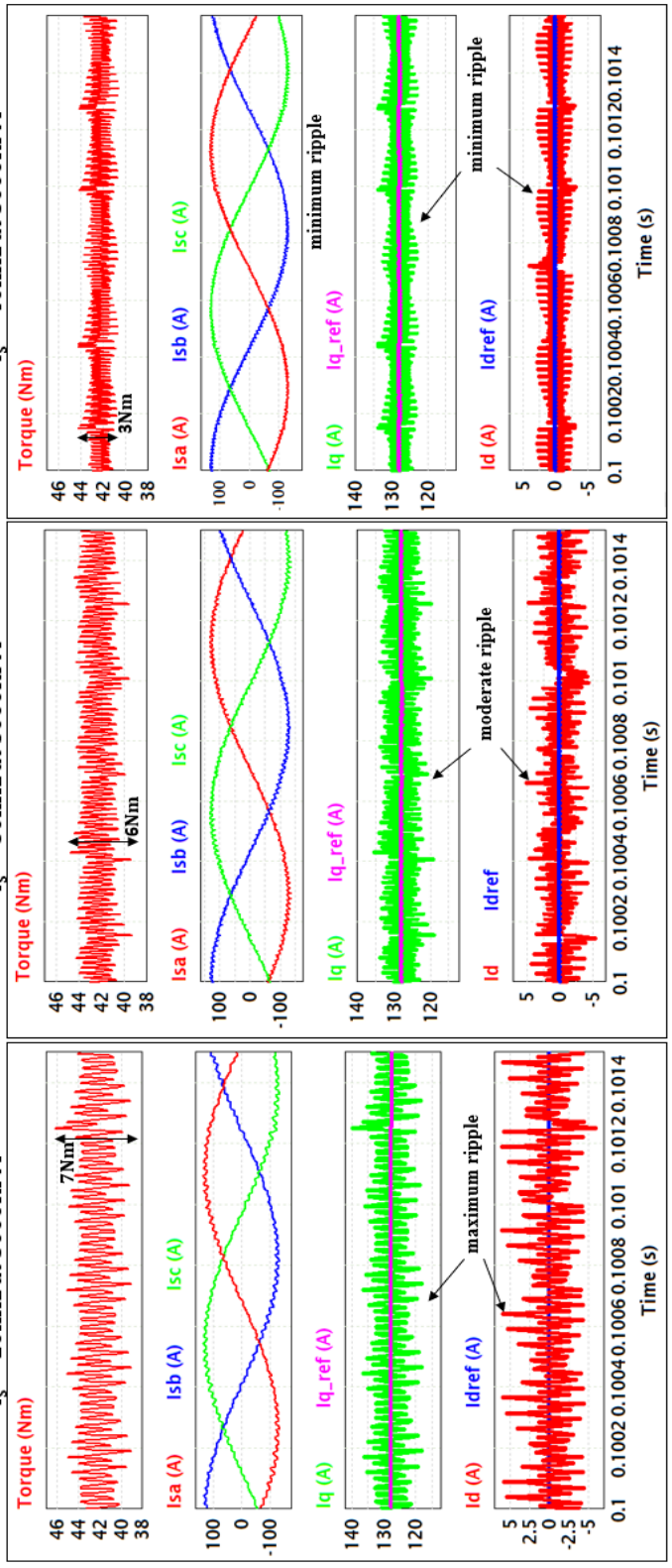

Figure 7.2. PSIM simulation results showing improvement in ripple content of torque, three-phase currents, and dq currents at various switching frequencies in the constant torque regime at 5000rpm.

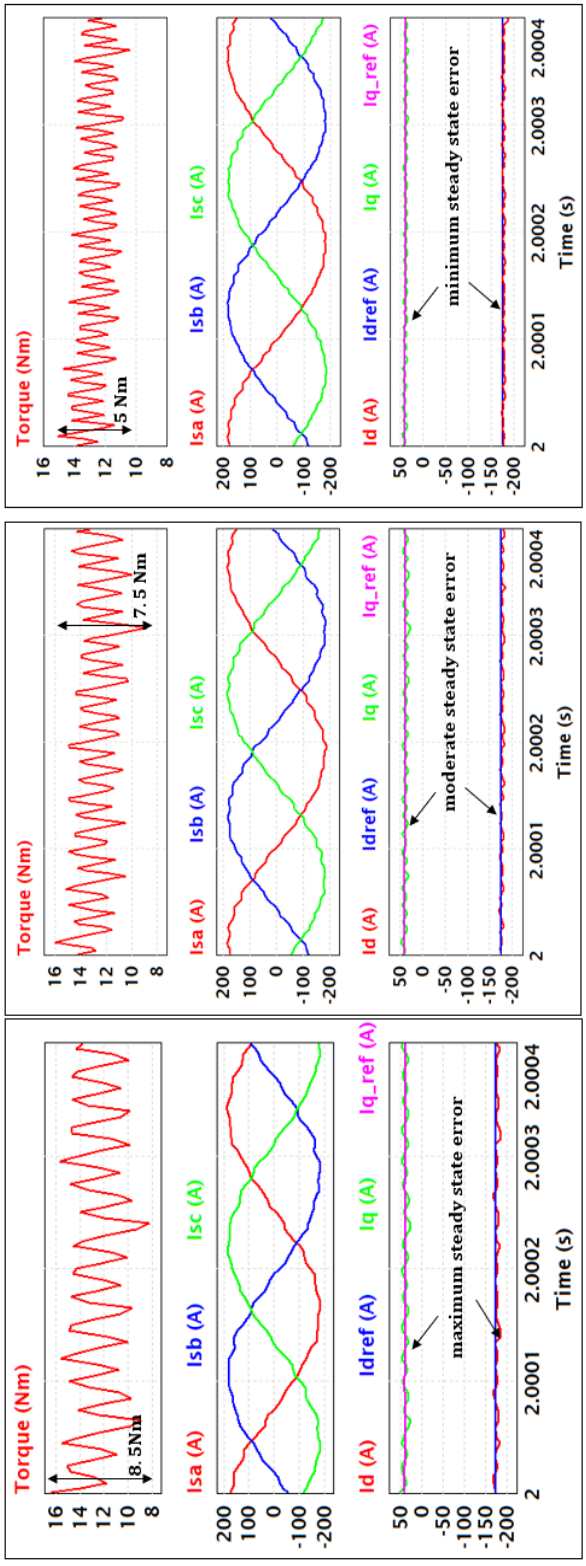

Figure 7.3. PSIM simulation results showing improvement in ripple content of torque, three-phase currents, and dq currents at various switching frequencies in the field weakening regime at a maximum speed.

7.3. Simulation Results of Comparative Analysis of SRF-PI and CVC Regulation Strategies

Continuous domain simulations have been done to validate the performance of SRF-PI current regulator with decoupling and CVC regulation strategy for both MTPA or constant torque and field weakening regimes. All the case studies have been reported for estimated inductances of $\hat{L} = 0.8L, L, \text{and } 1.2L$. A step change in q-axis current has been introduced while operating the machine at a rated speed of 5000RPM in MTPA region. In the MTPA regime, the q-axis currents have been tracked perfectly with more significant peak overshoots and more settling time employing SRF-PI current regulation strategy with decoupling voltages for an estimated inductance as shown in Figure 7.4. There is no presence of peak overshoots in CVC regulation strategy despite deviation in estimated inductance as reported in Figure 7.5. A step change in d-axis current has been introduced while operating the machine at a constant torque of 5Nm in the field weakening regime. In field weakening regime, employing SRF-PI current regulation strategy with decoupling, the d-axis currents have been tracked perfectly but the motor has been pushed to operate at either reduced or over speeds for deviations in estimated inductance as shown in Figure 7.6. In case of CVC regulation strategy, the speed response is almost identical despite the deviation in estimated inductance as shown in Figure 7.7.

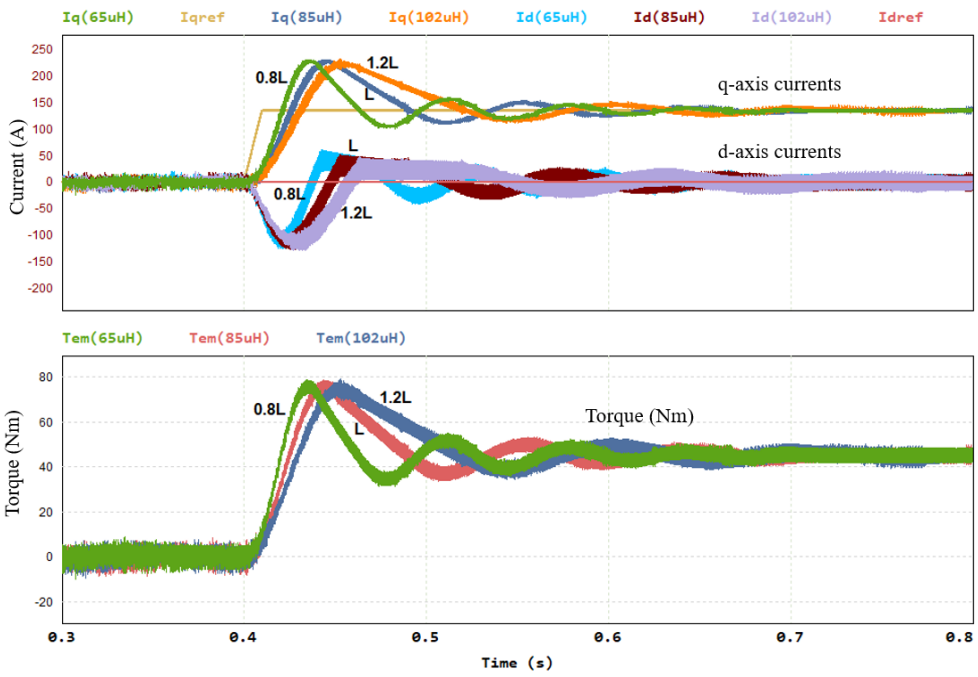

Figure 7.4. Simulation results of the proposed special motor drive, employing SRF-PI current regulation strategy with decoupling at a rated speed of 5000RPM, bandwidth of 3kHz, and switching frequency of 30kHz for a change in q-axis current from 0 to 135A in MTPA region. High peak overshoot is result of larger bandwidth.

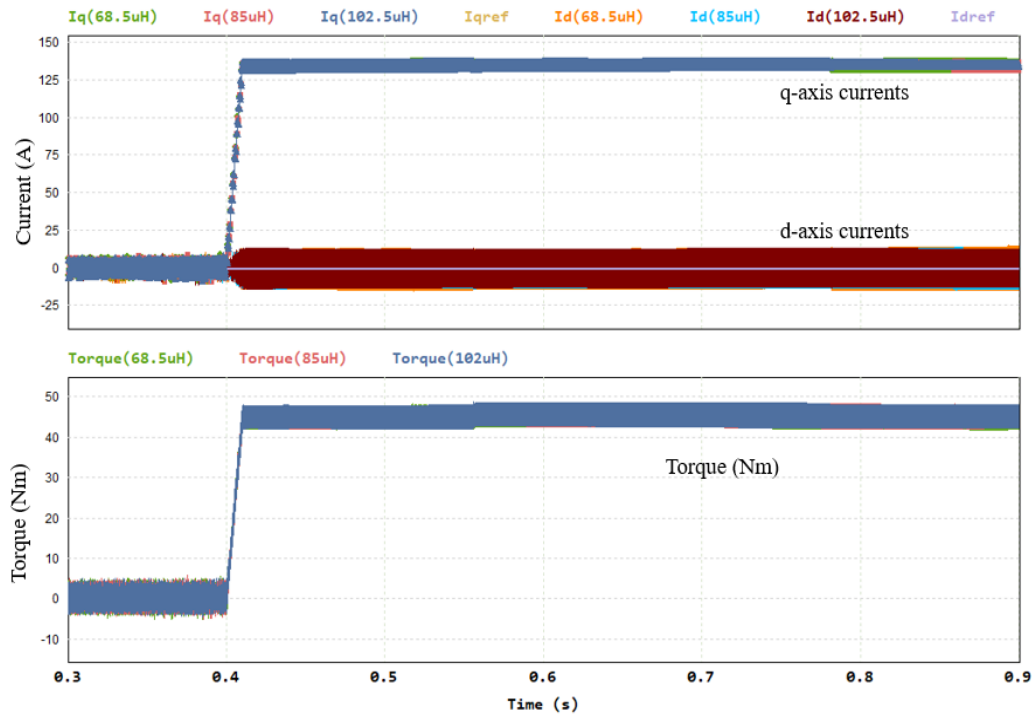

Figure 7.5. Simulation results of the proposed special motor drive system, employing CVC current regulation strategy at a rated speed of 5000RPM, bandwidth of 3kHz, and switching frequency of 30kHz for a change in q-axis current from 0 to 135A in MTPA region.

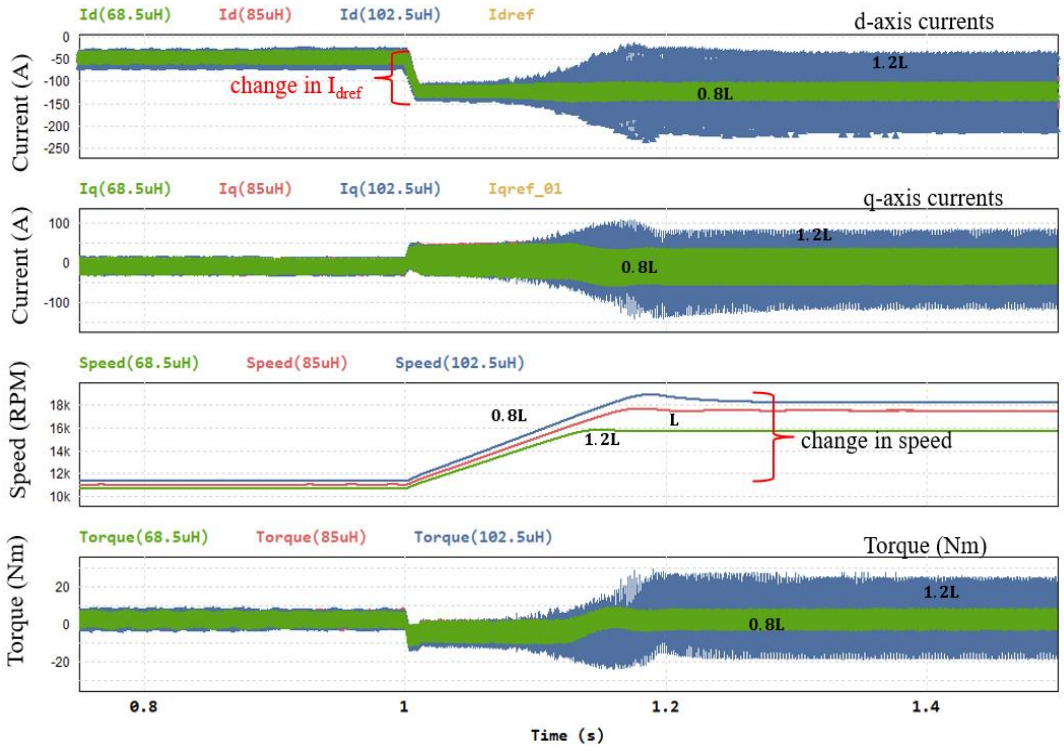

Figure 7.6. Simulation results of the proposed special motor drive, employing SRF-PI current regulation strategy with decoupling at a torque of 5Nm, bandwidth of 3kHz and switching frequency of 30kHz for a change in d-axis current from -100A to -125A in field weakening regime.

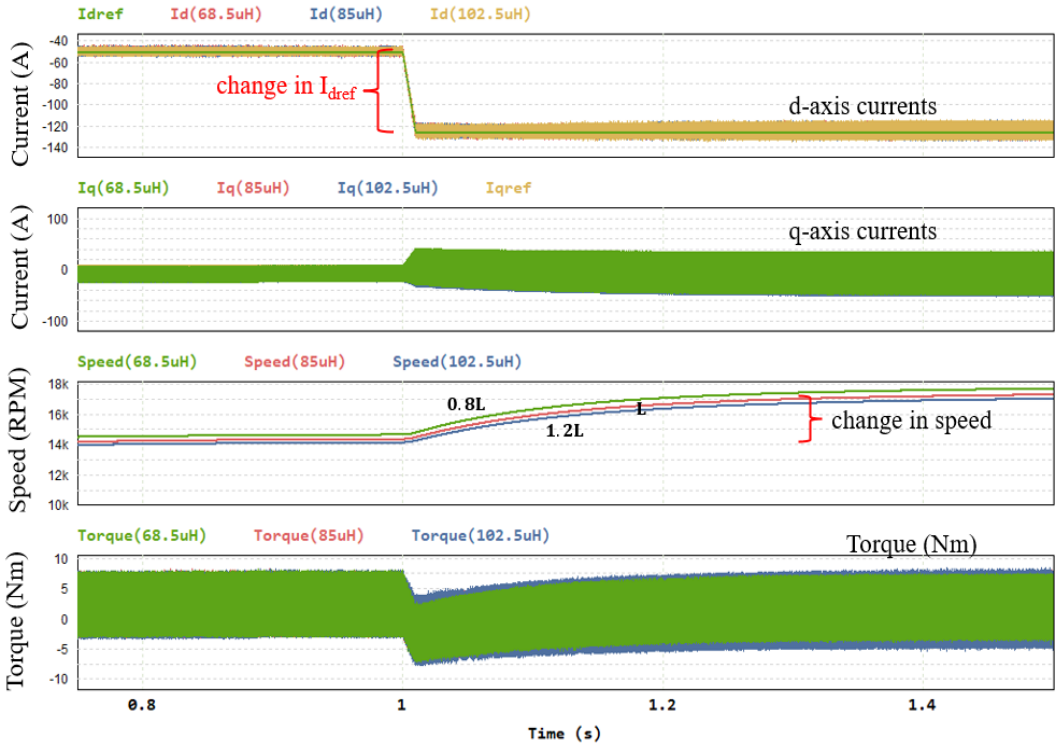

Figure 7.7. Simulation results of the proposed special motor drive, employing SRF-PI current regulation strategy with decoupling at a torque of 5Nm, bandwidth of 3kHz and switching frequency of 30kHz for a change in d-axis current from -100A to -125A in field weakening regime.

7.4. C-HIL Results of Comparative Analysis of SRF-PI and CVC Regulation Strategies

Controller hardware in the loop has been employed to verify SRF-PI current regulator with decoupling and CVC regulation strategy for the MTPA regime. Typhoon HIL 604 and TI DSP F28335 Delfino are used to implement power stage of the motor drive system and control algorithms at 500Vdc and a switching frequency of 40kHz. The controller is configured to implement torque control strategy by regulating the q-axis current through a serial communication interface. The current regulators are empirically tuned to have a bandwidth of 834 Hz corresponding to a rated speed of 5000rpm. Series path proportional integral controllers are employed to regulate the currents. Trapezoidal rule is applied to discretize the integrators at the specified sampling frequency.

In the SRF-PI current regulation strategy, peak overshoots and settling times are significantly high for both q-axis and d-axis currents, also reflected as high ripple content in the torque as reported in Figure 7.8. Thus, the presence of poor transient behavior in the SRF-PI current regulation strategy is due to decoupling voltages. In the CVC regulation strategy, peak overshoots and settling times are significantly low for both q-axis and d-axis currents, reflected as low ripple content in the torque, despite variation in the estimated inductances as reported in Figure 7.9. Thus, the transient behavior of the proposed doubly salient motor drive system is improved by the CVC regulation strategy.

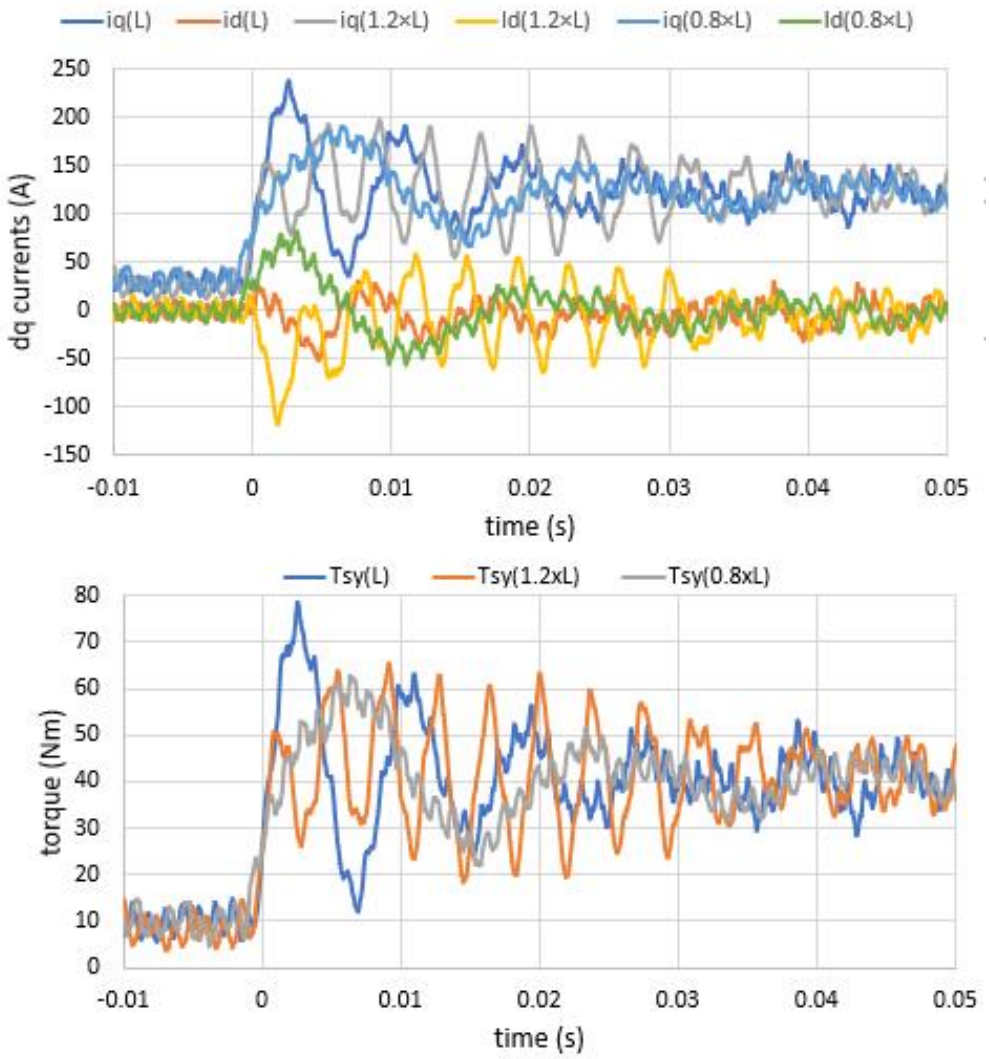

Figure 7.8. Experimental validation using CHIL for the proposed special motor drive, employing SRF-PI current regulation strategy with decoupling voltages at a rated speed of 5000rpm, bandwidth of 834Hz, and switching frequency of 40kHz for a change in q-axis current from 30A to 125A, reflected as a change in the torque from 10Nm to 40Nm in the MTPA regime.

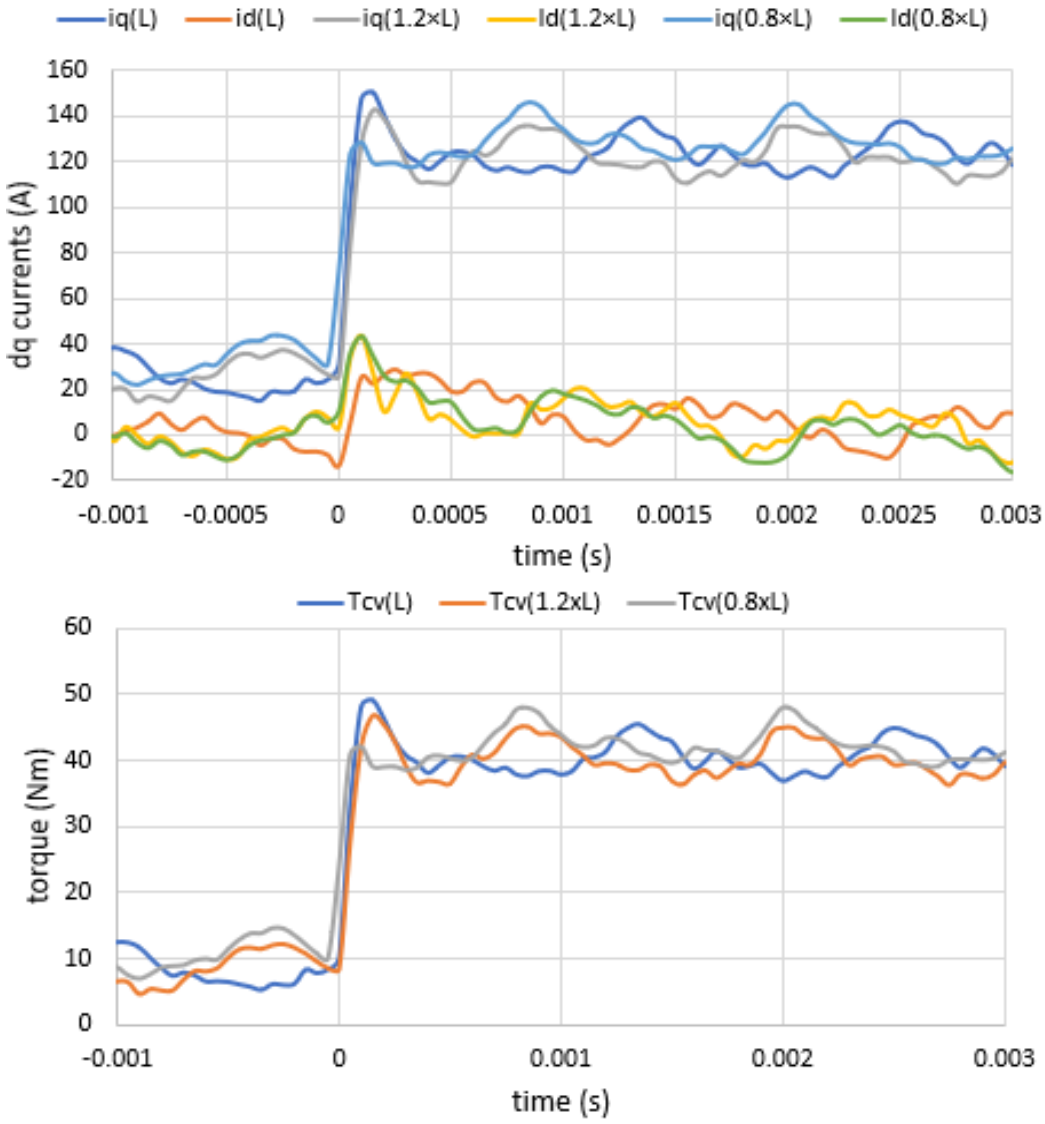

Figure 7.9. Experimental validation using CHIL for the proposed special motor drive, employing CVC regulation strategy at a rated speed of 5000rpm, bandwidth of 834Hz, and switching frequency of 40kHz for a change in q-axis current from 30A to 125A, reflected as a change in the torque from 10Nm to 40Nm in the MTPA regime.

CHAPTER 8: EXPERIMENTAL VALIDATION OF CONTROL ALGORITHMS

8.1. Introduction

This chapter focuses on presenting the details of the experimental setup and validation of torque control algorithms to assess the performance of the open frame laboratory prototype (OFLP) of the proposed high-power density motor. It covers the specifics of the motor dynamometer experimental setup, the design of experiments aimed at identifying the plant model of the OFLP, and the implementation of torque control algorithms.

8.2. Open frame laboratory prototype of the high power density motor

An open-frame laboratory prototype (OFLP) of the high-power density motor has been constructed to validate its performance using the dyno setup. A portion of the stator slot segment is illustrated in Figure 8.1, displaying the respective nomenclature of the design matrices. The design matrices for the OFLP are documented in TABLE 8.1. Figure 8.2 shows an image of the OFLP, featuring stator segments embedded with toroidal windings, permanent magnets (PMs), and a reluctance type. An inset picture of a modular stator segment embedded with a toroidal coil, with two terminals out, is presented in Figure 8.2. The terminals of each toroidal coil are connected accordingly, resulting in a topology of three-phase 12 slots or coils, with 4 coils per phase in a star configuration. The stator segments are separated by placing PMs of opposite polarity between them.

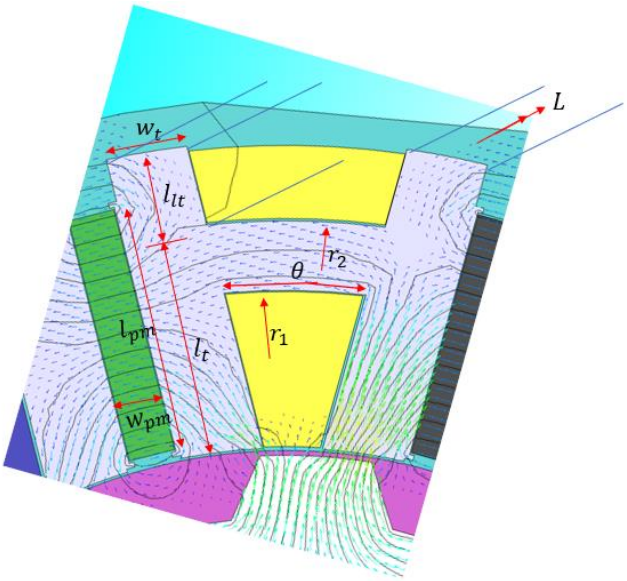

Figure. 8.1. 2D schematic of FEA illustrating dimensions of stator segment and PM.

TABLE 8.1: DESIGN MATRICES OF STATOR SEGMENT AND PM OF DSPM

Stack Length L	101.66mm
Tooth width w_t	8.38mm
Effective tooth length l_t	23.33mm
Leakage tooth length l_{lt}	8.24mm
Inner radius of core r_1	71.12mm
Outer radius of core r_2	78.26mm
Arc length θ	14.4mm
Width of PM w_{PM}	4.8mm
Radial Length of PM l_{PM}	25.86mm

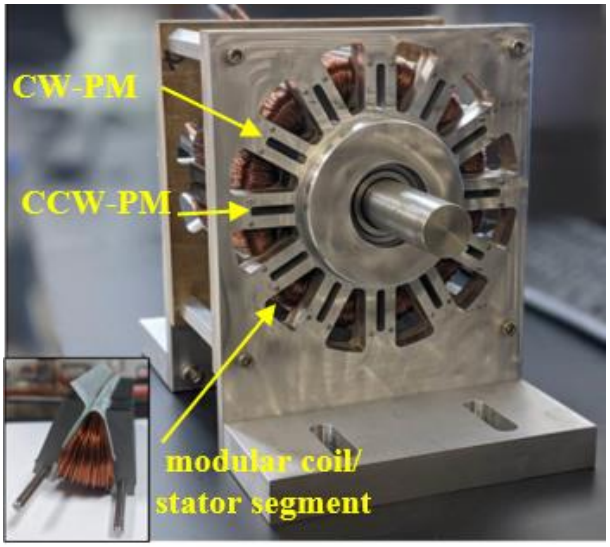

Figure 8.2. Open frame laboratory prototype of the three-phase special modular machine with 12 concentrated coils and 12 PMs in the stator and 12 protrusions in the rotor.

8.3. Experimental setup of the OFLP integrated with dynamometer test bench.

An experimental test bench setup has been established, featuring a dyno integrated with the OFLP. The schematic of the experimental test setup is illustrated in Figure 8.3. This configuration includes two electric machines, each equipped with its dedicated drive system. The first machine is a 3-phase induction machine with a rated operating point of 36Nm at 3525RPM, driven by a 3-phase AC/DC/AC YASKAWA drive. The induction machine drive setup operates at a specified speed condition, serves as a prime mover to spin the OFLP. The second motor drive system consists of an OFLP integrated with a SiC traction inverter, powered by a 300V DC power supply. The OFLP motor drive system is designed for torque control mode, while the induction machine drive system operates at the desired speed.

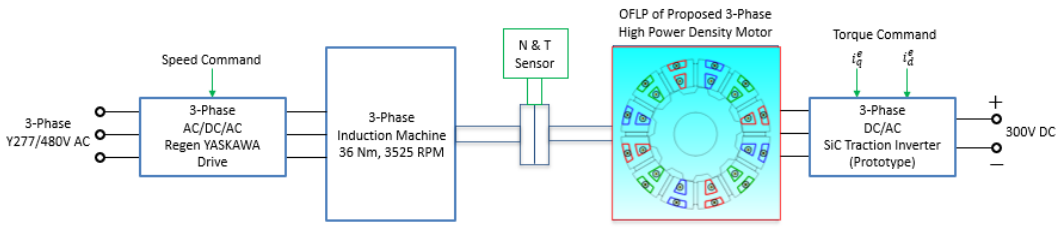

Figure. 8.3. Schematic of the experimental dyno test setup of the OFLP of the proposed special double salient machine operating as a generator at unity power factor.

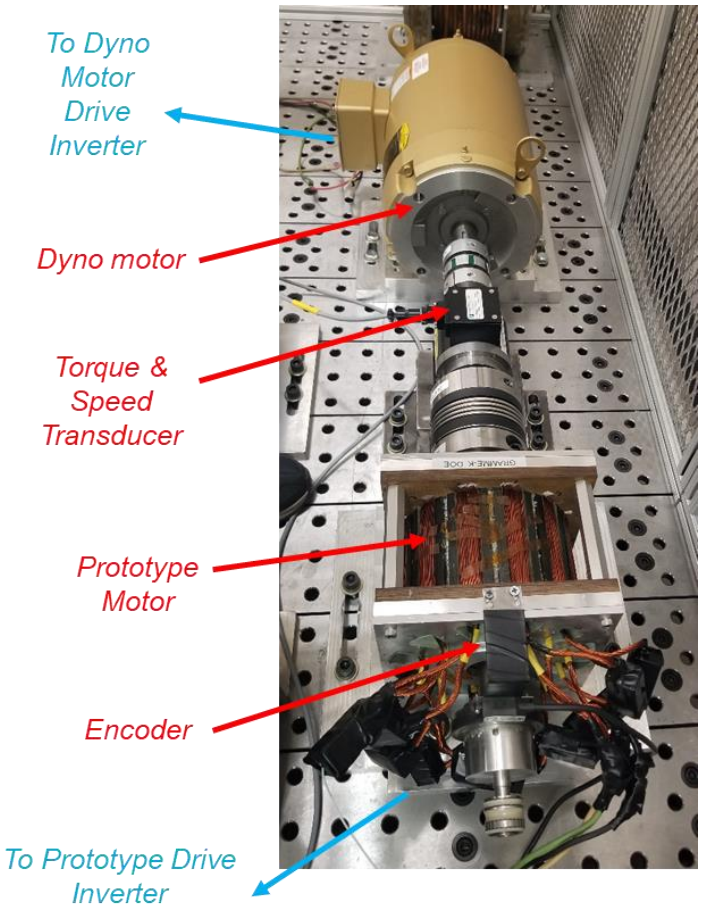

Figure. 8.4. Picture of the experimental setup of the OFLP integrated with dynamometer.

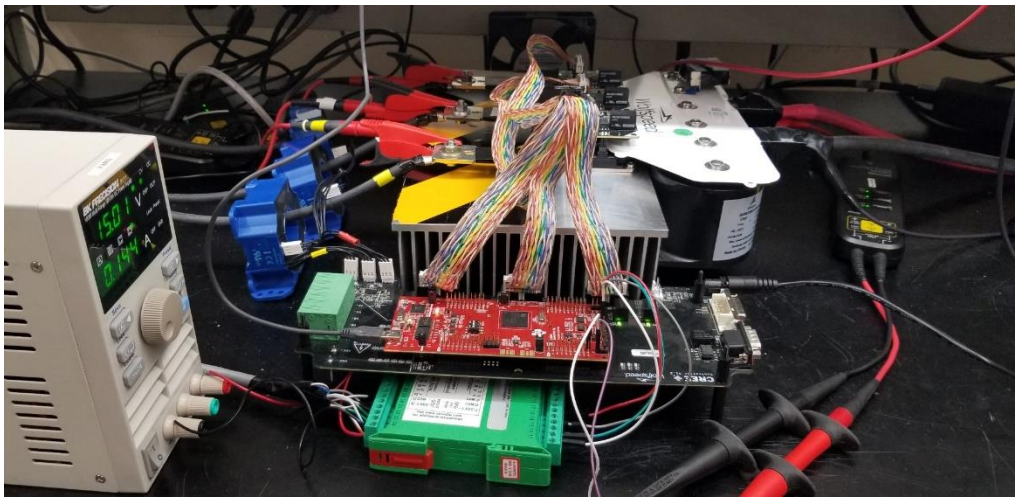

Figure. 8.5. Picture of SiC inverter and embedded systems hardware.

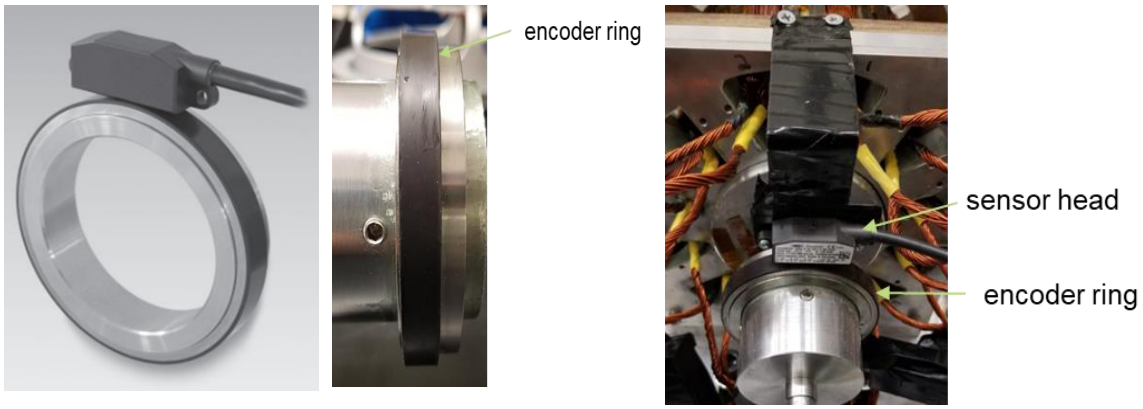

(a) (b) (c)

Figure. 8.6. Incremental bearingless encoder installation (a) Baumer ITD69H00, (b) Encoder ring installed on motor shaft, (c) Shaft mounted encoder ring with sensor head mounted to motor frame.

8.4. Design of Experiments

The following design of experiments have been conducted on the OFLP of the motor using the dynamometer setup,

1. Open circuit test to validate performance of back EMF and to determine flux linkage constant Ψ_{pm} (V/rpm):

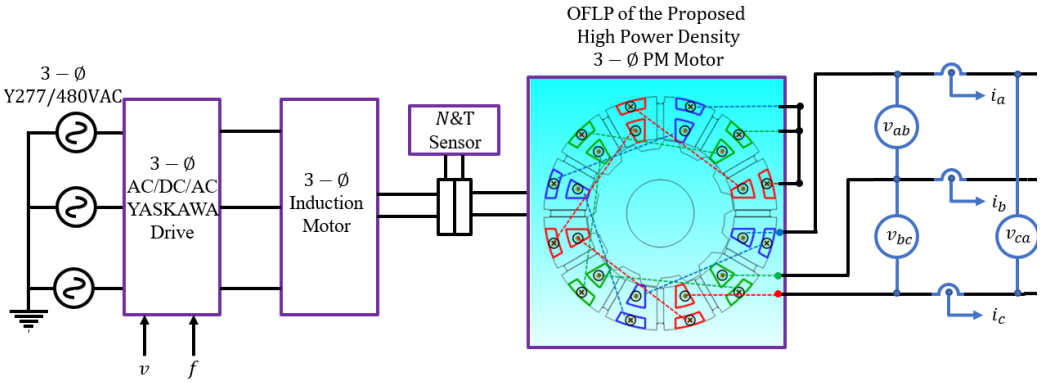

Figure. 8.7. Schematic of the experimental dyno test setup of the OFLP of the proposed special double salient machine operating as a generator under open circuit.

2. Static torque test to validate performance of torque:

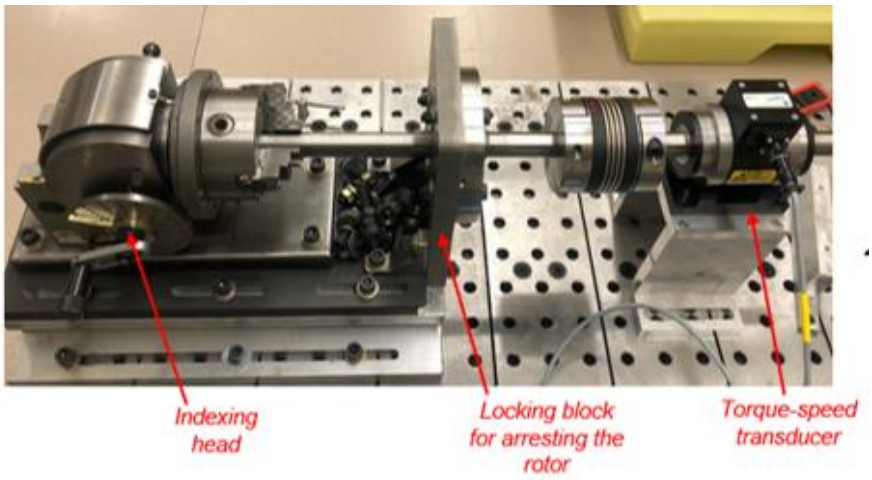

Figure. 8.8. Picture of static torque test setup to lock the rotor.

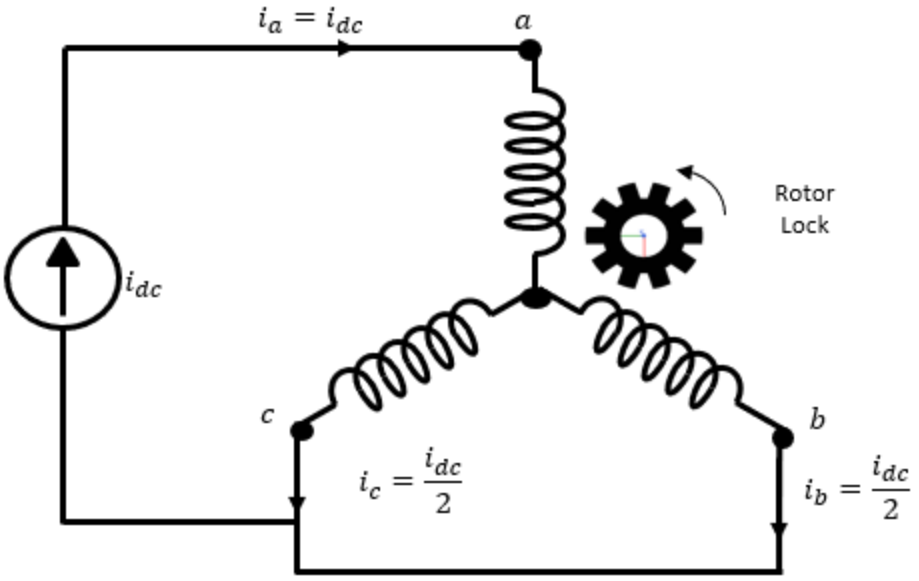

Figure. 8.9. Schematic of circuit for static torque test.

3. Unity power factor test with resistive load to identify plant model and to calibrate controls:

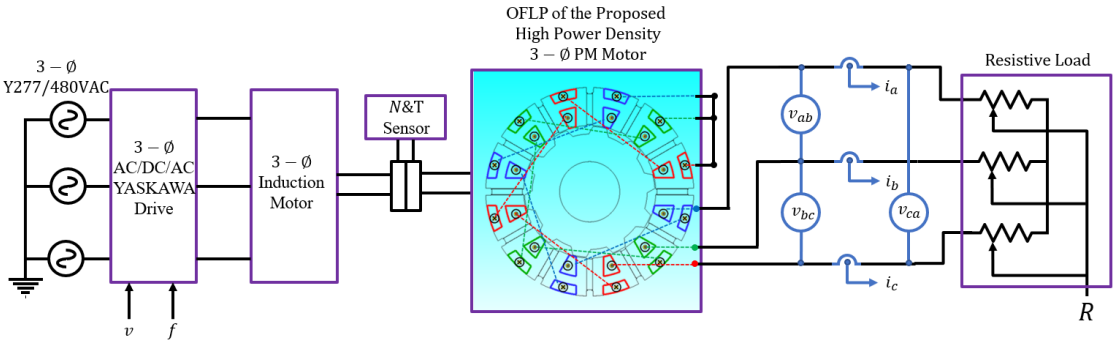

Figure. 8.10. Schematic of the experimental dyno test setup of the OFLP of the proposed special double salient machine operating as a generator at unity power factor.

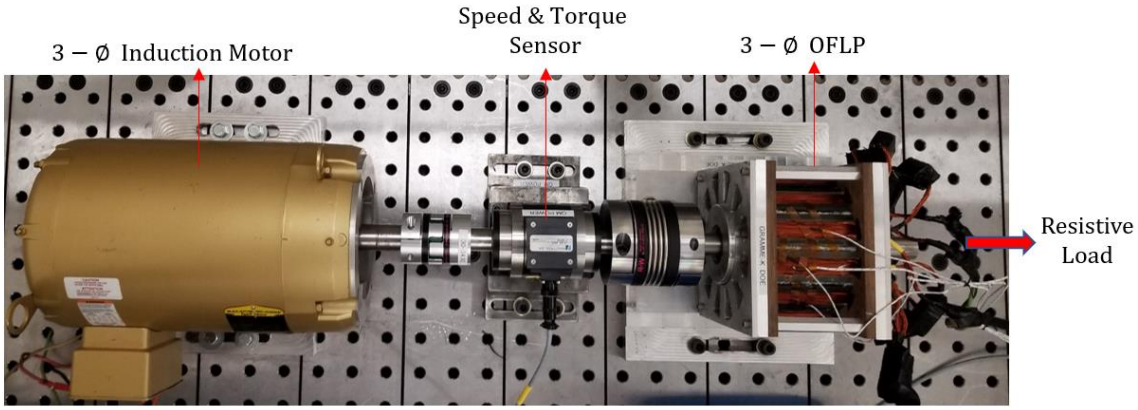

Figure. 8.11. Picture of the experimental dyno test setup of the OFLP of the proposed special double salient machine operating as a generator at unity power factor.

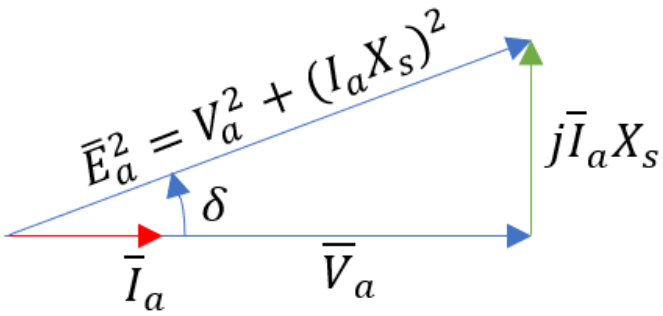

Figure. 8.12. Schematic of per phase vector diagram of the OFLP as a generator driving a resistive load at unity power factor.

4. Validation of control algorithms within dynamometer capabilities (3600RPM, 30Nm).

8.5. Experimental Results

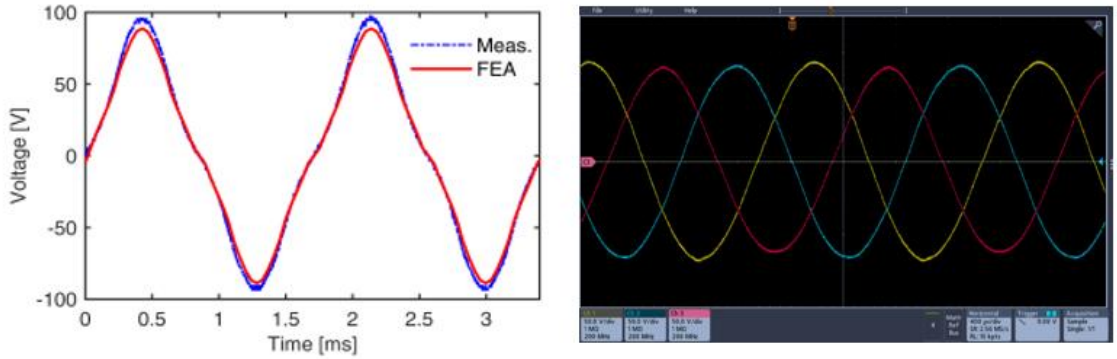

Figure. 8.13. Simulated and experimental open-circuit back EMF for phase-A open ended winding (left). Experimental open-circuit back EMF for line voltages between phases in star connection topology (right).

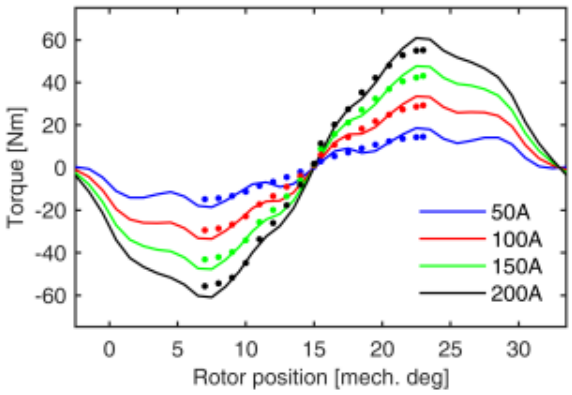

Figure. 8.14. Test and FEA simulation results for static torque versus rotor position.

TABLE 8.2. EXPERIMENTAL DATA FROM A UNITY POWER FACTOR GENERATOR TEST, EMPLOYED FOR INDUCTANCE IDENTIFICATION. THE AVERAGE INDUCTANCE VALUE SATISFACTORILY COMPARES WITH THE VALUE ESTIMATED BASED ON FEA SIMULATIONS.

Speed (RPM)	3500	3000	2400	2000
Frequency (Hz)	588	499	400	332
Load Current (A)	65	60	52	45
Terminal voltage per phase: V_a(V)	41.3	36.12	29.9	27.76
Induced voltage per phase: E_a (V)	52.3	43.6	34.8	30.1
Reactance per phase: $X_s = X_d = X_q$ (Ω)	0.439	0.364	0.291	0.243
Inductance per phase $L_s = L_d = L_q$ (μH)	116.25	116.10	116.20	116.5

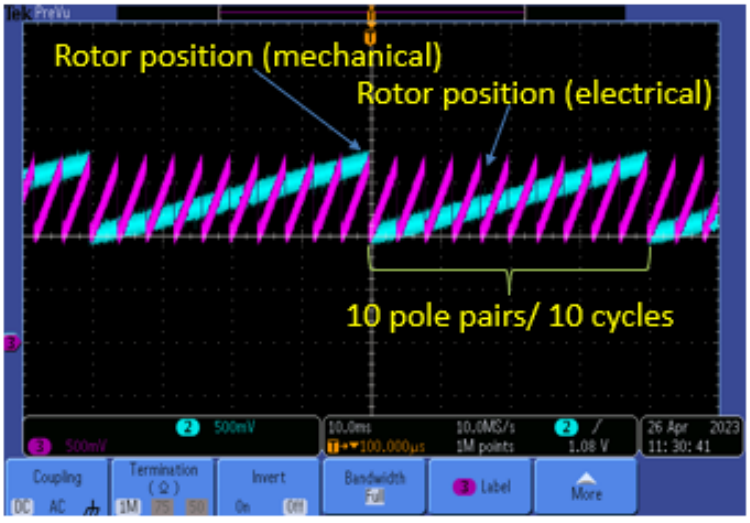

Figure. 8.15. Experimental waveform of mechanical and electrical equivalence of rotor position of the OFLP.

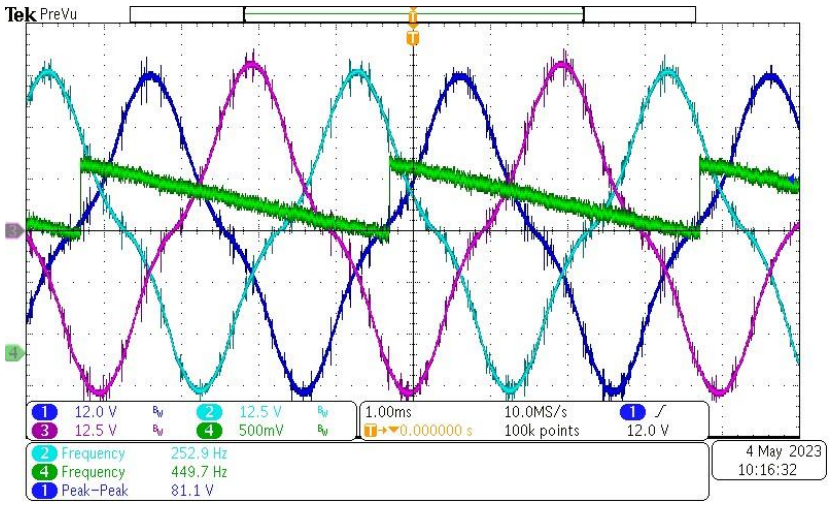

Figure. 8.16. Experimental waveforms of alignment of back EMF and rotor position to achieve maximum flux linkage operating point of the OFLP.

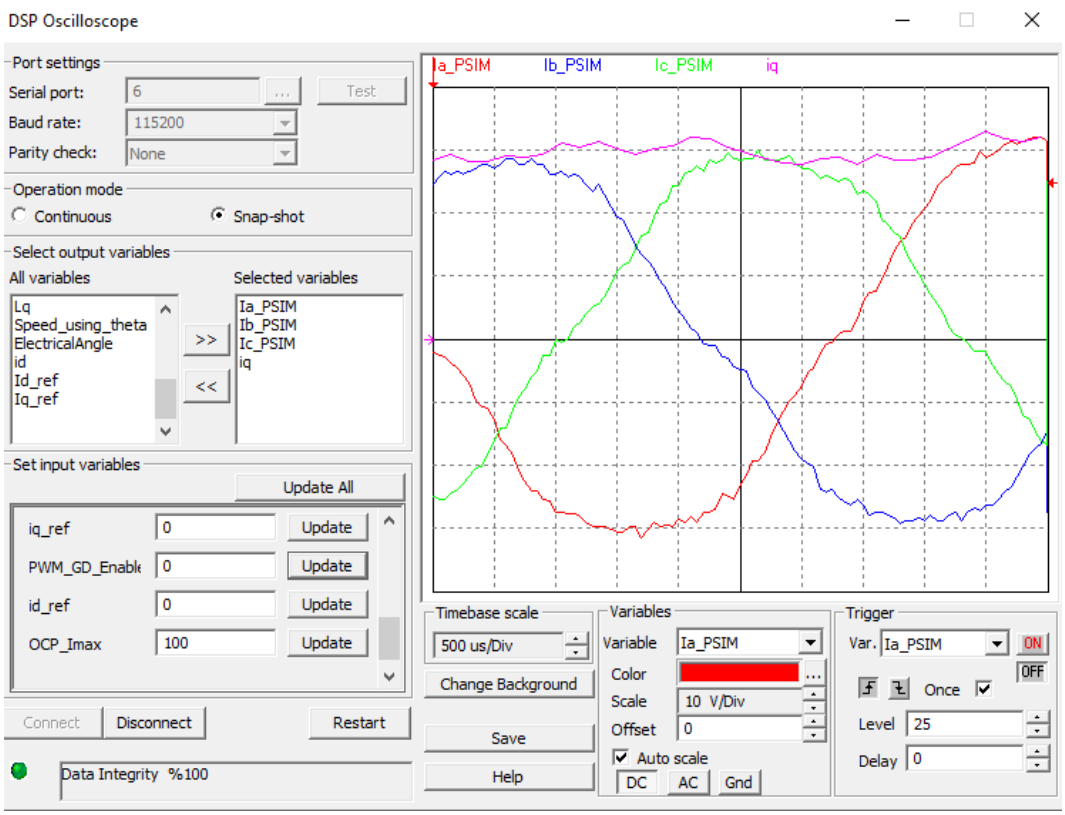

Figure. 8.17. Experimental waveforms of q-axis current and respective three-phase currents of the OFLP at 1500RPM, 7.5Nm.

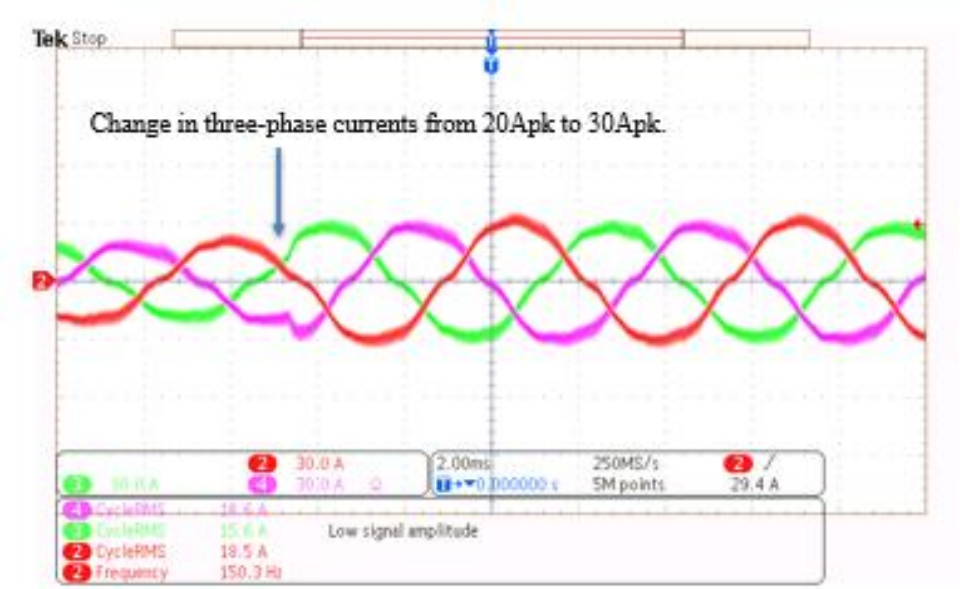

Figure. 8.18. Experimental waveforms of change in three-phase currents of the OFLP for the commanded q-axis current of 30A.

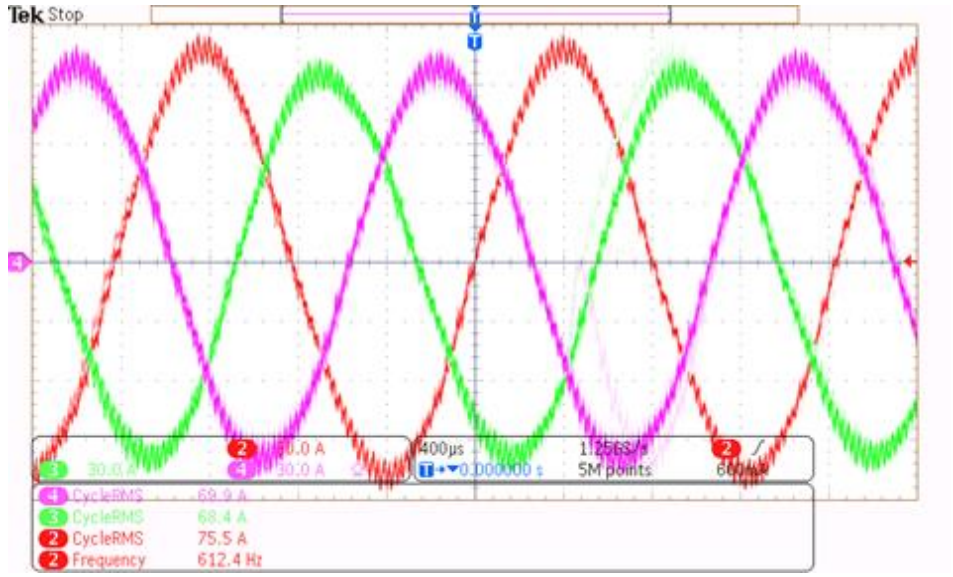

Figure. 8.19. Experimental waveforms of three-phase currents of the OFLP for the commanded q-axis current of 98.4A.

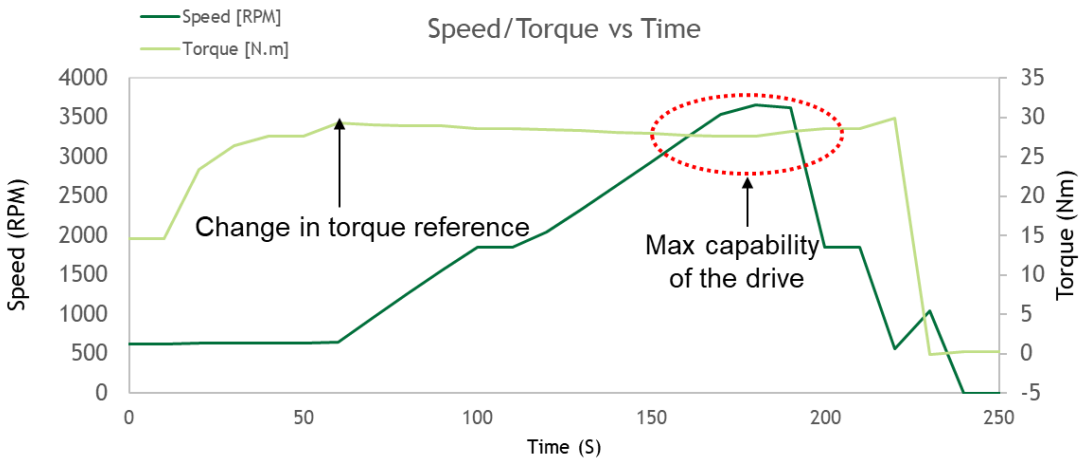

Figure. 8.20. Speed and torque profile readings from Magtrol as applied to the special DSPM prototype with respect to time.

CHAPTER 9: CONCLUSIONS

State of the art and trend in design matrices of traction motors and traction inverters employed in commercially available electric vehicles have been reviewed. The volumetric power density in kW/L and gravimetric power density in kW/kg of the traction motors and traction inverters have been profiled. Torque production mechanism of electric machines with saliency and non-saliency have been reviewed.

Several topologies of electric machines with mechanically doubly salient structures have been analyzed. Analysis of a special machine topology, which features a doubly salient structure and permanent magnets in the stator and provides very high power density performance has been presented in this dissertation. The machine analyzed is highly suited for electric vehicle traction applications and consists of 12 stator segments and toroidally wound concentrated coils, separated by 12 PMs in the stator, and a reluctance-type rotor with 10 protrusions equivalent to 20 electric poles.

Despite the mechanically doubly salient structure, the proposed machine has non-salient behavior. An emphasis has been made to investigate the non-salient behavior of the special machine. Lumped parameter magnetic equivalent circuits (LPMEC) were established for the doubly-salient special machine with PMs in the stator, yielding open circuit flux linkages, back EMF, self and mutual inductances, and dq inductances that were found to be in close agreement with results from finite element analysis.

The non-saliency behavior of machine with doubly salient structure was also identified by investigating the presence of spatial harmonics in self and mutual inductances. The negligible harmonics in the self and mutual inductances of the proposed DSPM result in

almost negligible equivalent saliency and synchronous reluctance torque. The LPMEC method used in this digest helped in understanding the key performance indices of the proposed DSPM by iteratively adapting the relative permeability of the core from the BH curve.

The experimental static torque test of the open frame laboratory prototype (OFLP), finite element method (FEM), and analytical LPMEC resulted in identical torque versus rotor position plots. A peak torque of 41 Nm at 90º electrical was reported, further confirming the non-salient behavior observed through the study of spatial harmonics.

A non-salient dq equivalent circuit was established and verified using experimental results of open circuit and static torque tests reported in prior work. A high-fidelity plant model of the machine was developed using JMAG-RT to develop a model-based motor drive system. The plant model was then imported into PSIM simulation software in the form of lookup tables. Considering the non-salient behavioral characteristics of the proposed motor, constant torque angle ($i_d^e = 0$) or MTPA control and constant voltage constant power (CVCP) control methodologies were implemented to regulate the speeds over a wide range to suit electric vehicle traction applications. The decoupling voltages were introduced at the output of the current controller to cancel out the effect of the cross-coupling in the plant model.

The speed and dq currents were observed to track the reference signals in both constant torque and field weakening regimes over a wide speed range (3x base speed) till 17000rpm. Improvements in torque and current profiles were achieved by operating the proposed motor drive system at higher switching frequencies. Thus, the proposed doubly salient

machine of very high-power density (50kW/L) was characterized as non-salient motor similar to surface permanent magnet motor and operated over a wide speed range.

A complex vector current (CVC) regulation strategy for an open frame lab prototype of special high-power dense three-phase doubly-salient machine with 12 coils, 12PMs, and 10 rotor protrusions was analyzed. An error in the estimation of inductance $\hat{L}$ was anticipated because the FEA software has considered the proposed non-conventional special machine as a non-salient synchronous machine, such as PMSM.

A complex vector representation of the plant model with complex conjugate poles at $S_{p1,2} = -\frac{R}{L} \pm j\omega$ was considered to implement the CVC regulation strategy with back EMF compensation and no decoupling feed forward voltages. A comparative analysis of the CVC regulation strategy with classical PI current regulation strategy in synchronous reference frame (SRF-PI) with decoupling voltages was discussed. The decoupling voltages translate the complex conjugate poles of plant into real poles i.e at $S_{p1,2} = -\frac{R}{L}$ and zeros of the controller were adjusted accordingly at $S_{z1,2} = -\frac{k_i}{k_p} = -\frac{R}{\hat{L}}$. In contrast, in the CVC regulation strategy, the zeros created by the controller were at $S_{z1,2} = -\frac{k_i}{k_p} + j\omega = -\frac{\hat{R}}{\hat{L}} \pm j\omega$ with no decoupling feedforward voltage loops, canceled the complex conjugate poles $S_{p1,2} = -\frac{R}{L} \pm j\omega$ effectively for $\hat{L} = L$.

From stability analysis, simulation results, and experimental validation employing controller hardware in the loop, the CVC regulator tracked change in reference currents precisely with faster settling time and less peak overshoot compared to SRF-PI with decoupling feedforward voltages despite errors in estimated values of inductances. An

improved transient behavior of the current and torque responses for the proposed special doubly salient machine was achieved with CVC regulation strategy.

Analytical outcomes and proposed control methodologies employing an open frame laboratory prototype (OFLP) of the proposed machine and SiC based traction inverter were validated by employing experimental tests. The currents of the proposed DSPM were observed to track the reference signals in the synchronous reference frame employing model-based approach.

CHAPTER 10: FUTURE WORKS

The doubly-salient machines will be explored further in four different aspects listed below,

1. Dual rotating reference frames: In the analysis of winding function theory, two distinct spatial harmonics contribute to the formation of a rotating magnetic field. By considering lower and higher-order spatial harmonics, two separate rotating reference frames emerge. A specialized dq-axis theory will be explored to address the dual rotating reference frame theory associated with doubly-salient machines.
2. Magnet free machines: Considering the global crisis in the procurement of rare earth magnets, magnet free topologies will be developed with doubly-salient structures.
3. Control of DC Field: Decentralized DC field current regulation strategies will be explored to effectively control the flux associated with specific coils.
4. Multiple stator DSPM: As the proposed DSPMs exhibit lower torque performance compared to SPM and FSPM, a new topology involving multiple stator modules stacked along the axial length of the rotor will be investigated to enhance torque performance. The topology of DSPMs with multiple stators will be studied.

REFERENCES

[1] “Electrical and Electronics Technical Team Road Map,” *U.S. Drive Partnership,* Oct. 2017.

[2] A. Krings and C. Monissen, "Review and Trends in Electric Traction Motors for Battery Electric and Hybrid Vehicles," *2020 International Conference on Electrical Machines (ICEM),* pp. 1807-1813, Aug 2020.

[3] S. J. Rind, Y. Ren, Y. Hu, J. Wang, and L. Jiang, "Configurations and control of traction motors for electric vehicles: A review," *Chinese Journal of Electrical Engineering*, vol. 3, no. 3, pp. 1-17, December 2017.

[4] E. A. Grunditz and T. Thiringer, "Performance Analysis of Current BEVs Based on a Comprehensive Review of Specifications," *IEEE Transactions on Transportation Electrification, vol. 2, no. 3, pp. 270-289,* Sept. 2016.

[5] K.T. Chau, Wenlong Li, “Overview of electric machines for electric and hybrid vehicles,” *International Journal of Vehicle Design, vol. 74, no.1, pp. 46-71,* Sep 2013.

[6] “Comparing 10 Leading EV Motors: Webcast,” *Virtual Conference on Charged EV Engineering*, July 2020.

[7] J. Liu, M. Anwar, P. Chiang, S. Hawkins, Y. Jeong, F. Momen, S. Poulos, and S. Song, “Design of the Chevrolet Bolt EV Propulsion System,” *SAE International Journal of Alternative Power Trains,* Vol. 5, pp. 79-86, May 2016.

[8] Tim Burress, “Electrical Performance, Reliability Analysis, and Characterization,” *DoE VTO Annual Merit Review*, June 2017.

[9] J. Reimers, L. Dorn-Gomba, C. Mak, A. Emadi, "Automotive Traction Inverters: Current Status and Future Trends", *IEEE Transaction on Vehicular Technology,* Vol.68, No.4, pp. 3337-3350, April 2019.

[10] Tim Burress, "Benchmarking of Competitive Technologies," *DoE VTO Annual Merit Review,* Washington, D.C, May 2011.

[11] J.R. Hendershot & T.J.E. Miller, "Design of Brushless Permanent-Magnet Machines," *Motor Design Books LLC,* 2010.

[12] D.W. Novotny, and T.A. Lipo, "Vector Control and Dynamics of AC Drives," *Oxford University Press*, 1996.

[13] T.A. Lipo, "Introduction to A.C Machine Design," *IEEE Press, John Wiley & Sons Inc,* New Jersey, 2017.

[14] Gianmario Pellegrino, Alfredo Vagati, and Paolo Guglielmi, "Performance Comparison Between Surface-Mounted and Interior PM Motor Drives for Electric Vehicle Application," *IEEE Transactions on Industrial Electronics,* Vol.59, No. 2, pp. 803-811, Feb. 2012

[15] Gianmario Pellegrino, Francesco Cupertino, and Chris Gerada, "Automatic design of synchronous reluctance motors focusing on barrier shape optimization," *IEEE Transactions on Industry Applications,* Vol. 51, No.2, pp. 1465-1474, August 2014.

[16] T. Burress, "Evaluation of the 2007 Toyota Camry Hybrid Synergy Drive System," *Oak Ridge National Laboratory*, 2008.

[17] T. Burress, "Evaluation of the 2010 Toyota Prius Hybrid Synergy Drive System," *Oak Ridge National Laboratory*, 2011.

[18] Ayman M. El-Refaie, Thomas M. Jahns, and Donald W. Novotny, “Analysis of Surface Permanent Magnet Machines with Fractional-Slot Concentrated Windings,” *IEEE Transactions on Energy Conversions*, Vol.21, No.1, March 2016.

[19] Khwaja Rahman, Peter J. Savagian, Nitinkumar Patel, and Robert Dawsey, “Retrospective of Electric Machines for EV and HEV Traction Applications at General Motors,” *IEEE Energy Conversion Congress and Exposition (ECCE)*, Sep. 2019.

[20] https://www.additive-drives.de/en/project/racing-engine/

[21] Yoshinori Sato, Shigeaki Ishikawa, Takahito Okubo, Makoto Abe, and, Katsunori Tamai, Development of High Response Motor and Inverter System for the Nissan LEAF Electric Vehicle, *SAE World Congress & Exposition*, Jan. 2011.

[22] Https://web.archive.org/web/20090123001021/http://www.greencar.com/features/gm-ev1/

[23] K. T. Chau, "Overview of Electric Vehicle Machines - From Tesla to Tesla, and Beyond," *2016 International Conference of Asian Union of Magnetics Societies (ICAUMS)*, pp. 1-6, Oct 2016.

[24] K. Rahman, S. Jurkovic, P. J. Savagian, N. Patel and R. Dawsey, "Retrospective of electric machines for EV and HEV traction applications at general motors," *2016 IEEE Energy Conversion Congress and Exposition (ECCE)*, pp. 1-8, Feb 2017.

[25] S. Jurkovic, K. Rahman, B. Bae, N. Patel, and P. Savagian, "Next-generation chevy volt electric machines; design, optimization, and control for performance and rare-

earth mitigation," *2015 IEEE Energy Conversion Congress and Exposition (ECCE)*, Montreal, QC, Canada, pp. 5219-5226, 2015.

[26] K. Rajashekara, "Present Status and Future Trends in Electric Vehicle Propulsion Technologies," *IEEE Journal of Emerging and Selected Topics in Power Electronics*, vol. 1, no. 1, pp. 3-10, March 2013.

[27] R. Vartanian, H. A. Toliyat, B. Akin and R. Poley, "Power factor improvement of synchronous reluctance motors (SynRM) using permanent magnets for drive size reduction," *2012 Twenty-Seventh Annual IEEE Applied Power Electronics Conference and Exposition (APEC)*, pp. 628-633, 2012.

[28] I. Boldea, L. Tutelea, and C. I. Pitic, "PM-assisted reluctance synchronous motor/generator (PM-RSM) for mild hybrid vehicles: electromagnetic design," *IEEE Transactions on Industry Applications*, vol. 40, no. 2, pp. 492-498, March-April 2004.

[29] L. Knebl, C. Ondrusek and J. Kurfürst, "Ferrite Assisted Synchronous Reluctance Motor Design, Manufacturing and Material Influence on Motor Characteristics," *2018 18th International Conference on Mechatronics - Mechatronika (ME), Brno, Czech Republic*, pp. 1-6, 2018.

[30] P. Guglielmi, G. Giraudo, G. M. Pellegrino and A. Vagati, "P.M. assisted synchronous reluctance drive for minimal hybrid application," *39th IAS Annual Meeting., Seattle, WA, USA*, 2004, pp. 306, 2004.

[31] P. B. Reddy, A. M. El-Refaie, K. Huh, J. K. Tangudu and T. M. Jahns, "Comparison of Interior and Surface PM Machines Equipped With Fractional-Slot

Concentrated Windings for Hybrid Traction Applications," *IEEE Transactions on Energy Conversion,* vol. 27, no. 3, pp. 593-602, Sept. 2012.

[32] A. J. Bourgault, P. Roy, E. Ghosh and N. C. Kar, "A Survey of Different Cooling Methods for Traction Motor Application," 2019 *IEEE Canadian Conference of Electrical and Computer Engineering (CCECE),* Oct 2019.

[33] B. Groschup, M. Nell and K. Hameyer, "Operational Enhancement of Electric Drives by Advanced Cooling Technologies," *2019 IEEE Workshop on Electrical Machines Design, Control and Diagnosis (WEMDCD),* pp. 65-70, Oct 2019.

[34] G. Venturini, G. Volpe, M. Villani and M. Popescu, "Investigation of Cooling Solutions for Hairpin Winding in Traction Application," *2020 International Conference on Electrical Machines (ICEM),* pp. 1573-1578, Dec 2020.

[35] J. Juergens, A. Fricassè, L. Marengo, J. Gragger, M. De Gennaro and B. Ponick, "Innovative design of an air-cooled ferrite permanent magnet assisted synchronous reluctance machine for automotive traction application," *2016 XXII International Conference on Electrical Machines (ICEM),* pp. 803-810, Nov 2016.

[36] F. Calegari, G. Federico, E. Bassi, and F. Benzi, "Parameter identification of an high-efficiency PMA synchronous reluctance motor for design and control," *2017 IEEE International Symposium on Sensorless Control for Electrical Drives (SLED),* pp. 31-36, Oct 2017.

[37] G. Berardi, S. Nategh, N. Bianchi and Y. Thioliere, "A Comparison Between Random and Hairpin Winding in E-mobility Applications," *IECON 2020 The 46th Annual Conference of the IEEE Industrial Electronics Society,* pp. 815-820, Nov 2020.

[38] Alexander Kuehl, Andreas Riedel, Alexander Vogel, Sebastian Hartl, Tobias Glaessesl, Michael Masuch, Jeorg Franke, " Robot-based Production of Electric Motors with Hairpin Winding Technology," *Proceedings of the World Congress on Engineering and Computer Science,* Oct 2019.

[39] A. Arzillo et al., "Challenges and Future opportunities of Hairpin Technologies," *2020 IEEE 29th International Symposium on Industrial Electronics (ISIE),* pp. 277-282, July 2020.

[40] Y. Gai et al., "Cooling of Automotive Traction Motors: Schemes, Examples, and Computation Methods," *IEEE Transactions on Industrial Electronics,* vol. 66, no. 3, pp. 1681-1692, March 2019.

[41] L. Chen and B. Ge, "High Power Traction Inverter Design and Comparison for Electric Vehicles," 2018 IEEE Transportation Electrification Conference and Expo (ITEC), pp. 583-588, August 2018.

[42] C. Chen, M. Su, Z. Xu and X. Lu, "SiC-based automotive traction drives, opportunities and challenges," 2017 IEEE 5th Workshop on Wide Bandgap Power Devices and Applications (WiPDA), pp. 25-30, 2017.

[43] M. Anwar, M. K. Alam, S. E. Gleason and J. Setting, "Traction Power Inverter Design for EV and HEV Applications at General Motors: A Review," *2019 IEEE Energy Conversion Congress and Exposition (ECCE)*, pp. 6346-6351, Nov 2019.

[44] Desai. P, Anwar. M, Gleason. S, and Hawkins. S, "Power Electronics for GM 2-Mode Hybrid Electric Vehicles," SAE Technical Paper 2010-01-1253, April 2010.

[45] Gafford. J, Mazzola, M, Molen. M, Parker, C. et al, "A 1200-V 600-A Silicon-Carbide Half-Bridge Power Module for Drop-In Replacement of an IGBT IPM,"

SAE Technical Paper 2010-01-1251, April 2010.

[46] Loncarski, Jelena; Leijon, Mats; Srndovic, Milan; Rossi, Claudio; Grandi, Gabriele. 2015. "Comparison of Output Current Ripple in Single and Dual Three-Phase Inverters for Electric Vehicle Motor Drives" *Energies 8*, no. 5: 3832-3848, 2015.

[47] M. Niakinezhad, I. U. Nutkani and N. Fernando, "A New Modular Asymmetrical Half-Bridge Switched Reluctance Motor Integrated Drive for Electric Vehicle Application," *2018 IEEE 27th International Symposium on Industrial Electronics (ISIE)*, pp. 1003-1010, August 2018.

[48] A. S. Lutonin, A. Y. Shklyarskiy and Y. E. Shklyarskiy, "Control Strategy of Dual Fed Open-End Winding PMSM Drive for Traction Applications," 2020 IEEE Conference of Russian Young Researchers in Electrical and Electronic Engineering (EIConRus), pp. 746-749, March 2020.

[49] A. Matsumoto, M. Hasegawa and S. Doki, "A flux-weakening control method on Maximum Torque Control frame for IPMSM position sensorless control," IECON 2012 - 38th Annual Conference on IEEE Industrial Electronics Society, pp. 1612-1617, Dec 2012.

[50] F. Tinazzi, S. Bolognani, S. Calligaro, P. Kumar, R. Petrella and M. Zigliotto, "Classification and review of MTPA algorithms for synchronous reluctance and interior permanent magnet motor drives," 2019 21st European Conference on Power Electronics and Applications (EPE '19 ECCE Europe), pp. P.1-P.10, Nov 2019.

[51] S. Dwivedi, S. M. Tripathi and S. K. Sinha, "Review on Control Strategies of Permanent Magnet-Assisted Synchronous Reluctance Motor Drive," 2020 International Conference on Power Electronics & IoT Applications in Renewable Energy and its Control (PARC), pp. 124-128, May 2020.

[52] Manual of Motor Control Design Suite by PSIM, April 2020.

[53] Z. Chen, D. Boroyevich and R. Burgos, "Experimental parametric study of the parasitic inductance influence on MOSFET switching characteristics," *The 2010 International Power Electronics Conference - ECCE ASIA -, Sapporo*, pp. 164-169, June 2010.

[54] M. Feurtado et al., "High-Performance 300 kW 3-Phase SiC Inverter Based on Next Generation Modular SiC Power Modules," *PCIM Europe; International Exhibition and Conference for Power Electronics, Intelligent Motion, Renewable Energy and Energy Management*, Nuremberg, Germany, pp. 1-8, July 2019.

[55] Application Note of SiC XM3 Modules, Wolfspeed, 2019.

[56] Application Note of Dual Power Core SiC Inverter, Wolfspeed, 2020.

[57] Li, Muyang, "Flux-Weakening Control for Permanent-Magnet Synchronous Motors Based on Z-Source Inverters", *Master's Theses,Marquette University,* 2014.

[58] S. Morimoto, M. Sanada and Y. Takeda, "Wide-speed operation of interior permanent magnet synchronous motors with high-performance current regulator," *IEEE Transactions on Industry Applications*, vol. 30, no. 4, pp. 920-926, July-Aug. 1994.

[59] Jong-Hwan Song, Jang-Mok Kim and S. -K. Sul, "A new robust SPMSM control to parameter variations in flux weakening region," Proceedings of the 1996 IEEE IECON. 22nd International Conference on Industrial Electronics, Control, and Instrumentation, vol.21, pp. 1193-1198, 1996.

[60] A. Vagati, G. Pellegrino and P. Guglielmi, "Comparison between SPM and IPM motor drives for EV application," *The XIX International Conference on Electrical Machines - ICEM 2010,* Rome, Italy, pp. 1-6, 2010.

[61] C. Pollock and M. Wallace, "The flux switching motor, a DC motor without magnets or brushes," *Conference Record of the 1999 IEEE Industry Applications Conference. Thirty-Forth IAS Annual Meeting* (Cat. No.99CH36370), Phoenix, AZ, USA, pp. 1980-1987 vol.3, 1999.

[62] Hao Ge, “Fractional Slot Concentrated Winding Interior Permanent Magnet Machines with Reluctance Torque: Inductance-Based Methodology for Comprehensive Analysis, Design, and Control,” Ph.D. Dissertation, McMaster University, 2016.

[63] Yuefeng Liao, Feng Liang and T. A. Lipo, "A novel permanent magnet motor with doubly salient structure," *IEEE Transactions on Industry Applications,* vol. 31, no. 5, pp. 1069-1078, Sept.-Oct. 1995.

[64] J.Flynn, Norman B. Talsoe, Jamie J. Childress, “Parallel Path Magnetic Technology for High Efficiency Power Generators and Motor Drives,”*AIP Conference Proceedings,* Feb 2006.

[65] Nimal Savio Lobo, “Doubly Salient Permanent Magnet Flux-Reversal-Free-Stator

Switched Reluctance Machines," *Ph.D. Dissertation, Virginia Polytechnic Institute and State University,* Jan 21, 2011.

[66] J. D. McFarland, T. M. Jahns and A. M. EL-Refaie, "Analysis of the torque production mechanism for flux-switching permanent magnet machines," *2014 IEEE Energy Conversion Congress and Exposition (ECCE),* pp. 310-317, Pittsburgh, PA, USA, 2014.

[66] Lipo, T.A, "Analysis of Synchronous Machines (2nd ed.)," *CRC Press,* 2012.

[67] Z. Q. Zhu, Y. Pang, D. Howe, S. Iwasaki, R. Deodhar and A. Pride, "Analysis of electromagnetic performance of flux-switching permanent-magnet Machines by nonlinear adaptive lumped parameter magnetic circuit model," *IEEE Transactions on Magnetics,* vol. 41, no. 11, pp. 4277-4287, Nov. 2005.

[68] F.W. Carter, "The magnetic field of the dynamo-electric machine", *The Jounal of the I.E.E.,* vol. 64, pp.1115-1138, 1926.

[69] Zhu, Z. Q. and David Howe. "Instantaneous magnetic field distribution in permanent magnet brushless DC motors. IV. Magnetic field on load." *IEEE Transactions on Magnetics* 29 (1993): 152-158.

[70] J. Laksar and L. Veg, "Reduced Schwarz-Christoffel Conformal Mapping in Surface-Mounted PMSM," *2018 18th International Conference on Mechatronics - Mechatronika (ME),* Brno, Czech Republic, pp. 1-8, 2018.

[71] S. D. Sudhoff, B. T. Kuhn, K. A. Corzine and B. T. Branecky, "Magnetic Equivalent Circuit Modeling of Induction Motors," *IEEE Transactions on Energy Conversion,* vol. 22, no. 2, pp. 259-270, June 2007.

[72] K. N. Srinivas and R. Arumugam, "Dynamic characterization of switched reluctance motor by computer-aided design and electromagnetic transient simulation," *IEEE Transactions on Magnetics*, vol. 39, no. 3, pp. 1806-1812, May 2003.

[73] E. C. Lovelace, T. M. Jahns and J. H. Lang, "A saturating lumped-parameter model for an interior PM synchronous machine," *IEEE Transactions on Industry Applications*, vol. 38, no. 3, pp. 645-650, May-June 2002.

[74] Z. Q. Zhu, J. T. Chen, Y. Pang, D. Howe, S. Iwasaki and R. Deodhar, "Modeling of end-effect in flux-switching permanent magnet machines," 2007 *International Conference on Electrical Machines and Systems (ICEMS),* Seoul, Korea (South), pp. 943-948, 2007.

[75] R. Dutta, M. F. Rahman and L. Chong, "Winding Inductances of an Interior Permanent Magnet (IPM) Machine with Fractional Slot Concentrated Winding," *IEEE Transactions on Magnetics*, vol. 48, no. 12, pp. 4842-4849, Dec. 2012.

[76] Peng Han, Murat G. Kesign, Dan M. Ionel, Rohan Gosalia, N. Shah, Charles J. Flynn, C. S. Goli, S. Essakiappan, and M. Manjrekar, "Design Optimization of a Very High Power Density Motor with a Reluctance Rotor and a Modular Stator Having PMs and Toroidal Windings," *2021 IEEE Energy Conversion Congress and Exposition (ECCE),* pp. 4424-4430, 2021.

[77] Application Note of JMAG Designer 20.2, Power Sys, JSOL, 2020.

[78] C.W. Brice et all, “Reference frames for simulation of electric motors and drives,” *International conference on electrical machines,* Espoo, August 2000.

[79] Jingxin Shi and Yu-Sheng Lu, "Field-weakening operation of cylindrical permanent-magnet motors," *Proceeding of the 1996 IEEE International Conference on Control Applications held together with IEEE International Symposium on Intelligent Control*, pp. 864-869, 1996.

[80] Dave Wilson, "Teaching Your PI Controller to Behave," *Texas Instruments Design Support Forum*, 2013.

[81] F. Briz, M. W. Degner and R. D. Lorenz, "Analysis and design of current regulators using complex vectors," *IEEE Transactions on Industry Applications*, vol. 36, no. 3, pp. 817-825, May-June 2000.

[82] D. N. Zmood, D. G. Holmes and G. H. Bode, "Frequency-domain analysis of three-phase linear current regulators", *IEEE Transactions on Industry Applications*, vol. 37, no. 2, pp. 601-610, March-April 2001.

PUBLICATIONS

Journal:

[1] C. S. Goli, Murat G. Kesign, Dan M. Ionel, Peng Han, S. Essakiappan, J. Gafford and M. Manjrekar, "Analysis and Design of an Electric Machine Employing a Special Stator With Phase Winding Modules and PMs and a Reluctance Rotor," *IEEE Access*, vol. 12, pp. 9621-9631, 2024.

Conference Papers:

[2] C. S. Goli, M. Manjrekar, S. Essakiappan, P. Sahu and N. Shah, "Landscaping and Review of Traction Motors for Electric Vehicle Applications," *2021 IEEE Transportation Electrification Conference & Expo (ITEC),* Chicago, IL, USA, pp. 162-168, 2021.

[3] C. S. Goli, S. Essakiappan, P. Sahu, M. Manjrekar and N. Shah, "Review of Recent Trends in Design of Traction Inverters for Electric Vehicle Applications," *2021 IEEE 12th International Symposium on Power Electronics for Distributed Generation Systems (PEDG),* Chicago, IL, USA, pp. 1-6, 2021.

[4] P. Han et al., "Design Optimization of a Very High Power Density Motor with a Reluctance Rotor and a Modular Stator Having PMs and Toroidal Windings," *2021 IEEE Energy Conversion Congress and Exposition (ECCE),* Vancouver, BC, Canada, pp. 4424-4430, 2021.

[5] C. S. Goli, S. Essakiappan, J. Gafford, D. M. Ionel, M. Manjrekar and N. Shah, "Modeling and Speed Control for a Doubly-Salient Special Machine Employing a High-Fidelity Plant Model," 2022 IEEE Vehicle Power and Propulsion Conference (VPPC), Merced, CA, USA, pp. 1-8, 2022.

[6] C. S. Goli, S. Essakiappan, D. M. Ionel, J. Gafford and M. Manjrekar, "Complex Vector Current Regulation Strategy for a High-Speed Doubly Salient Machine with Stator PMs," *2023 IEEE Transportation Electrification Conference & Expo (ITEC),* Detroit, MI, USA, 2023.

[7] C. S. Goli, Maryam Saleh, S. Essakiappan, D. M. Ionel, J. Gafford and M. Manjrekar, “Comparative Analysis of Doubly Salient Special Machine and Flux Switching Machine with PMs in Stator,” *2023 IEEE International Electric Machines & Drives Conference,* Sanfransisco, USA, 2023.

[8] C. S. Goli, S. Essakiappan, D. M. Ionel, J. Gafford and M. Manjrekar, “Analysis of a Mechanically Doubly Salient Electric Machine using FE and Lumped Parameter Magnetic Equivalent Circuit Models,” *2023 IEEE Energy Conversion Congress and Exposition (ECCE),* Nashville, USA, 2023.

Publications on Other Topics:

[11] C. S. Goli, M. Manjrekar and P. Sahu, "Comparative Analysis, Modeling, and Experimental Validation of Current Regulation Strategies for a Grid- Tied Inverter with LCL Filter," *2022 IEEE Industry Applications Society Annual Meeting (IAS),* Detroit, MI, USA, pp. 1-8, 2022. (Received First Paper Prize Award)

[12] C. S. Goli, M. Manjrekar, P. Sahu, A. Chanda and S. Essakiappan, "Implementation of Stationary and Synchronous Frame Current Regulators for Grid Tied Inverter using Typhoon Hardware in Loop System," *2021 IEEE 12th International Symposium on Power Electronics for Distributed Generation Systems (PEDG),* Chicago, IL, USA, pp. 1-8, 2021.